MOTION CONTROL OF ELECTROMECHANICAL ACTUATORS AT SUB-MICRON PRECISION

HOI WAI CHOW

Ph.D

The Hong Kong Polytechnic University

2012

THE HONG KONG POLYTECHNIC UNIVERSITY

Department of Electrical Engineering

MOTION CONTROL OF ELECTROMECHANICAL ACTUATORS AT SUB-MICRON PRECISION

Hoi Wai CHOW

A thesis submitted in partial fulfillment of the requirements for the Degree of Doctor of Philosophy

August 2011

CERTIFICATE OF ORIGINALITY

I hereby declare that this thesis is my own work and that, to the best of my knowledge and belief, it reproduces no material previously published or written, nor material that has been accepted for the award of any other degree or diploma, except where due acknowledgement has been made in the text.

______________________________(Signed)

Hoi Wai CHOW (Name of student)

Abstract

High precision linear motion has attracted much attention in the manufacturing industry. To fulfill the requirements of demanding industrial applications, high precision motion system should be accurate, fast responding, and inexpensive. Various types of linear motion systems have been developed, but few of them can fulfill all of the above requirements. A linear motion system usually suffers from external environmental influences, such as friction, erratic external forces, and load variations.

This project aims to investigate and propose several motion-control methodologies, so that a fast and high precision linear motion down to submicron level can be achieved. Under this goal, a high precision position encoder based on laser interferometric method has been developed. A resolution increasing circuit has been developed and a fusion algorithm has been utilized so that the speed and accuracy of the motion sensing can be improved. In addition, a prototype of high precision linear motion system based on a permanent magnet linear motor, with an adaptive intelligent control algorithm has been developed. Both the simulation results and the experimental results validate the usefulness of the proposed methods.

This project develops a high precision low cost linear motion sensor based on the optical interferometer with a 3×3 fiber coupler. The simulation results and the experimental measurements from a prototype linear motion sensor have demonstrated that a successful linear motion sensing system with low cost, long measurement range, and high accuracy can be achieved by using the novel optical

interferometric method.

Optical linear incremental encoder is widely employed in high precision linear motion control because of its high accuracy characteristic. However, the maximum measurement speed of this incremental encoder is usually limited by the clock frequency boundary in the decoder circuitry. To make the incremental encoder more useful in high speed motion control applications, the speed limitation of linear incremental encoder have been overcome by developing a novel enhancement circuit. This circuit is responsible for increasing the resolution of sensor outputs, so that the measurement speed can be improved. The velocity information from the optical linear incremental encoder and the velocity output of the resolution increasing circuit are combined by the data fusion algorithm, so that an accurate position sensing system with higher measurement speed range can be developed. The feasibility of the idea is verified by experiments.

Developing a high precision linear motion system with a direct-drive linear motor is a difficult task because this motion system usually suffers from many non-linear characteristics, such as friction, ripple-force, variation of parameter. A high precision motion control algorithm with a modified disturbance compensator and the internal model reference control is proposed and implemented. Satisfactory experimental results have been obtained. The proposed controller is capable of achieving high speed and high accuracy (with position error less than 0.1μm). Compared with the performance of the conventional disturbance compensator, the response speed to the position command and the external disturbance is much faster when modified disturbance compensator is adopted.

Publications Arising from this Thesis

3 journal papers and 2 conference papers have been produced, as a result of this project research. Both conference papers were warmly received by audiences, and they generated interesting discussions. The details of the papers are listed below:

[1] Chow, H.W., and Cheung, N., 'Low cost displacement sensor at sub-micron precision based on 3×3 optical coupler for vibrating surface', *The* 5^{th} *IEEE International Conference on Mechatronics*, Málaga, Spain, pp.1–6, April 2009

[2] Chow, H.W., Cheung, N.C., and Jin, W., 'A Low-Cost Submicrolinear Incremental Encoder Based on 3×3 Fiber-Optic Directional Coupler'. *IEEE Transactions on Instrumentation and Measurement*, Volume 59, Issue 6, pp.1624-1633, 2010

[3] Chow H.W., and Cheung N., 'High Speed Processing of Encoder Information by using a Dual-Resolution Approach', The 5^{th} IEEE Conference on Industrial Electronics and Applications, Taichung, Taiwan, pp.644-649, June 2010

[4] Chow H.W., and Cheung N., 'An Analog Detection Device in a Sub-micron Linear Encoder based on a Fiber Optic Interferometer with a 3×3 Coupler', *IET Science, Measurement & Technology*, Vol. 4, no. 5, pp.237-245, 2010

[5] Chow, H.W., Cheung, N.C., and Jin, W., 'Disturbance and Response Time Improvement of Sub-Micron Precision Linear Motion System by using Modified Disturbance Compensator and Internal Model Reference Control'. IEEE Transactions on Industrial Electronics, Ready to publish, 2012

Acknowledgments

First of all, I would like to express my sincere appreciation and gratitude to my chief supervisor, Dr. Norbert C. Cheung for his continuous support. He has always been supportive and encouraging throughout my research study. His academic guidance is extremely useful and beneficial. Without him, it would be impossible for me to fulfill my goal of pursuing for a PhD degree.

I would also like to thank Prof. Wei Jin, my co-supervisor, for his guidance regarding to the interferometer configuration. Prof. Jin's spirit and attitude had encouraged me to take up the research work and the PhD study.

I must thank Dr. Shi-Wei Zhao for this valuable suggestions and comments. I must also thank all my valuable friends and colleagues, who have helped me out in the times of need. Their assistances are highly appreciated.

I would like to gratefully acknowledge to the Hong Kong Polytechnic University for the support of this project through research account: RP47.

Lastly, I would like to deeply thank my parents, Mr. Wing-Yiu Chow and Mrs. Fung-Cheung Chow, and my brother, Mr. Hoi-Keung Chow, for their full support and back-up during my study.

Table of contents

List of figures

List of tables

List of acronyms

AFC	Adaptive feed-forward compensation
DSP	Digital Signal Processor
d-axis	direct axis
e.m.f.	Electro-motive force
ECL	External-cavity laser
IC	Integrated Circuit
IMRC	Internal Model Reference Control
ILC	Iterative Learning Control Algorithm
LED	Light Emitting Diode
LPF	Low Pass Filter
MEMS	Micro Electro-Mechanical System
MRAC	Model Reference Adaptive Control
PMLM	Permanent Magnet Linear Motor
PCB	Print Circuit Board
PID	Proportional-Integral-Derivative
PWM	Pulse Width Modulation
q-axis	quadrature axis
r.m.s	Root mean square
SMC	Sliding Mode Control
VCM	Voice Coil Motor

List of symbols

$\Delta_a(s)$	Additive plant perturbation
$\Delta_d(s)$	Stable factor perturbations
ΔK_f	Deviation of force constant
ΔL	Traveled distance of the movable target
$\Delta_m(s)$	Multiplicative plant perturbation
ΔM	Deviation of mass
$\Delta_n(s)$	Stable factor perturbations
Δt	Propagation time delay of the resolution increasing circuit
Δx	Traveled displacement of the movable target
δ	Phase difference between the stator axis and rotor axis of PMLM
φ	The initial phase difference for L is zero
ϕ	The phase shift induced by the movable target
λ	The wavelength of the laser in vacuum
λ_{qs}	The stator flux linkages along q-axis
λ_{ds}	The stator flux linkages along d-axis
θ	The initial phase of the waveform
μ_k	Mean value of the measurements at instant time interval k
σ_k^2	Variance of the measurements at instant time interval k
σ_1^2	Variance of the sensor 1
σ_2^2	Variance of the sensor 2
ω	Angular frequency
ω_{mr}	The mechanical angular speed of the rotor
ω_r	Applied electrical frequency

A_1, A_2	Coefficients of the force ripple in "sinθ+cosθ" format
a_1, a_2	Coefficients of the V_{afc} in "sinθ+cosθ" format
A_1', A_2'	Coefficients of the V_{ripple} in "sinθ+cosθ" format
A^2	The input power of proposed laser interferometer
a_j	Complex amplitudes of three waves in interferometer with 3×3 fiber coupler
A_{ripple}	Amplitude of the force ripple
C	Feedback parameter of self-mixing interferometer
$C_p(s)$	The simplified controller of position loop
$C_v(s)$	The simplified controller of velocity loop
d	The actual disturbance
$\hat{d}$	The estimated disturbance in disturbance observer
D	Viscosity constant
$D(s)$	The disturbance transfer function between the $F_{perturb}(s)$ and the $Y_{perturb}(s)$
$D_m(s)$	The denominator of the model of the plant
e	The position error
E_x	Component of light wave along x-axis
E_y	Component of light wave along y-axis
$F(s)$	The transfer function of low pass filter
F'_{cmp}	Estimated disturbance
F'_{cmp2}	The estimated disturbance by modified disturbance compensator
f_1	A non-linear function contains all disturbance acting on PMLM
F_{cmp}	The external disturbance force and the effect of parameter variation
F_{dis}	The external disturbance force adding to the PMLM
F_e	External applied force to the movable mechanism

F_{em}	Electromagnet force
$F_{friction}$	The function of classical friction model
F_{fri_model}	The model of kinetic friction which is function of velocity
F_{load}	Load force
$F_{perturb}(s)$	The external disturbances appear in IMRC
F_{ripple}	Ripple force
F_s	Maximum value of the static friction
$f_{sampling}$	The sampling frequency of the DSP
F_{thrust}	Thrust force from the motor
g	The adaptive gain
g_f	The cutoff frequency of the LPF in disturbance compensator
$G_{PWM}(s)$	The transfer function of the PWM driver
g_v	The cutoff frequency of the $M_v(s)$
g_x	The cutoff frequency of the $M_p(s)$
i	$\sqrt{-1}$
I'_{cmp}	The compensation current calculated from F'_{cmp}
I'_{cmp2}	The compensation current calculated from F'_{cmp2}
i_a, i_b, i_c	The injected currents to motor
I_a	Armature current
I_{amp}	The amplitude of the sinusoidal $I_{resultant}$
I_{avg}	D.C. offset of this sinusoidal $I_{resultant}$
I_{cmd}	Current command of the current loop
i_d, i_q, i_0	The injected currents to motor in d-q frame
i_{dr}	The rotor current along d-axis
i_{ds}	The stator currents along d-axis
I_f	Photo-current from photodiode

i_{fr}	The excitation current due to the permanent magnet field
I_{finial}	The final measured intensity from the two-beam laser interferometer
$I_{initial}$	The initial measured intensity from the two-beam laser interferometer
i_{qr}	The rotor current along q-axis
i_{qs}	The stator currents along q-axis
$I_{resultant}$	The resultant light intensity
I_s	The amplitude of the PMLM input current
K	Coupling coefficient of 3×3 fiber coupler
$K(s)$	The transfer function for converting the estimated disturbance to the compensation current
K_e	Back e.m.f constant
K_f	Force constant
K_{fn}	Nominal force constant
K_i	The variable gain used in novel disturbance compensation algorithm
K_{kj}	The coupling coefficient between the k-th and j-th waveguide
k_p, k_i, k_d	The gain of PID controller
K_t	The torque constant
L	The distance between the movable target and fiber end of interferometer
L_a	The armature inductance
$L_{coupler}$	The coupler length
L_d	The inductance for d-axis
L_m	The mutual inductance between stator winding and rotor magnets
L_q	The inductance for q-axis

L_s The self-inductance of the stator when the $\delta = 180^0$

M Mass of the translator

$M(s)$ The predefined stable model of the IMRC

M_n Nominal mass

$M_p(s)$ The stable reference model used in the position loop controller

$M_v(s)$ The stable reference model used in the velocity loop controller

$N_m(s)$ The numerator of the model of the plant

O_1 The first output of proposed interferometer with 3×3 fiber coupler

O_1' Offset eliminated signal of O_1

O_{1mean} Offset of signal O_1

O_2 The second output of proposed interferometer with 3×3 fiber coupler

O_2' Offset eliminated signal of O_2

O_{2mean} Offset of signal O_2

p The number of poles

$P(s)$ the actual system function

Phase A The first digital signal from incremental encoder

Phase B The second digital signal from incremental encoder

P_{in} The input power of the PMLM

$P_m(s)$ The model of the plant

$P_{mp}(s)$ The model of the process of in the position loop of IMRC

$P_{mv}(s)$ The model of the process of in the velocity loop of IMRC

P_{out} The output power of the PMLM

$P_p(s)$ The actual process in position loop

$P_v(s)$ The actual process in velocity loop

$Q(s)$ The transfer function inside the IMRC controller

$Q_p(s)$ The transfer function of used in the position controller

$Q_v(s)$	The transfer function of used in the velocity controller
R	The resistance
$R(s)$	The command input of IMRC
R_a	Armature resistance
R_d	d-axis winding resistance of stator
R_e	The responsivity of photodiode
R_q	q-axis winding resistance of stator
S_1	Analog signal of $O_1'+O_2'$
S_1'	Digitalized signal of S_1
S_2	Analog signal of $O_1'-O_2'$
S_2'	Digitalized signal of S_2
S_3	Analog signal of $2O_1'+O_2'$
S_3'	Digitalized signal of S_3
S_4	Analog signal of $O_1'+2O_2'$
S_4'	Digitalized signal of S_4
T_{em}	Electromagnet torque
$U_{carrier}$	Peak to peak amplitude of the carrier of PWM driver
u_{cmd}	The amplitude of voltage command inputted to the PWM driver
u_{ff}	The feed-forward control signal
u_{h1}	The amplitude of the fundamental harmonic of input voltage of PMLM
u_{PID}	The control signal from PID controller
U_s	DC input of the PWM driver
v_1	Velocity measurement from sensor 1
$v_{1\mu}$	Mean value of the sensor 1
v_2	Velocity measurement from sensor 2

$v_{2\mu}$	Mean value of the sensor 2
V_a, V_b, V_c	The input voltages of PMLM
V_{afc}	Control signal calculated from adaptive feed-forward compensation
V_{apply}	Applied voltage
$v_{circuit}$	The measured velocity from the resolution increasing circuit
V_d, V_q, V_0	The applied voltages to motor in d-q frame
V_{ds}	The stator voltages along d-axis
$v_{encoder}$	The measured velocity from the optical linear incremental encoder
v_{fused}	Calculated velocity based on the data fusion algorithm
V_{ripple}	Virtual voltage input of force ripple
V_{qs}	The stator voltages along q-axis
W_1	The weighting factor for the optical linear incremental encoder
W_2	The weighting factor for the resolution increasing circuit
x	The position of the target
$X(s)$	Position of the motor (in s domain)
x_{cmd}	The required position command
$Y(s)$	The actual output of the process in the IMRC
$Y_{perturb}(s)$	The disturbance to system output
z	The position of coupler

Chapter 1
Introduction

1.1 Background and motivation of this thesis

For the past few decades, high precision linear motion control system has been in high demand from the manufacturing industry. Due to miniaturization, the precision requirements from products manufacturing are getting more and more demanding. Solder placement system, PCB separator, and 3D laser engraving are just some examples of high precision motion requirements [1]. Some companies also employ the high precision motion stages in other applications such as Micro Electro-Mechanical System (MEMS) assembling, automatic wafer handling and inspection, and photonic device alignment testing [2]. However, achieving submicron precision motion control is not an easy task and engineers will encounter great difficulties. A general positioning apparatus usually includes structural limitations such as backlash, velocity dead-zone, and static friction. The effects of these limitations are more obvious when general positioning apparatus is employed for submicron precision motion control.

Direct drive permanent magnet linear motor (PMLM) has been widely adopted in linear motion actuation because it has the advantages of less mechanical translators, small friction, no backlash, and high acceleration capability. These superior properties also enable engineers to construct very high precision linear motion systems down to sub-micron level. However, fabricating the high precision linear motion stage with PMLM will encounter many difficulties such as static and dynamic friction between moving contacts, ripple force between the moving coils and permanent magnets, performance degradation due to the variation of model parameters, load change, and external force disturbance.

Many engineers have devoted a large amount of efforts to overcome these difficulties. Huang and Sung [3] handled the parameter uncertainties by implementing flux estimation to determine the flux and phase angle, and by developing sliding-mode control with direct-thrust-control for the linear motion control. Cupertino et.al. [4] described a control system for a tubular synchronous linear motor based on sliding-mode control and a proportional-integral-based equivalent disturbance observer, which aims to address the effects of static friction and payload difference. Chen [5] proposed a new method for PMLM with a hysteretic relay feedback so as to identify the linear and nonlinear parameters, including force ripple and friction.

Obviously, constructing a high speed and high precision linear motion system is a complex and expensive job. This goal is an unavoidable trend in the manufacturing industry and the demand is likely to increase more in future years. The above reasons motivate the author to develop a set of tools which can assist the achievement of a simple, easy-to-implement, and low-cost high precision motion system.

1.2 Organization of this thesis

This thesis is organized as follows:

Chapter 1 describes the progress and background of high precision motion control during the past few decades. Motivations and objectives of this thesis are also established. The organization of the thesis is introduced and the contributions of this thesis are also discussed.

Chapter 2 describes some typical high precision motion sensors. In this thesis, a high precision motion sensor, the optical linear incremental encoder, is utilized for providing the reference position. This chapter introduces the operation of this type of linear incremental encoder. Another type of high precision motion sensor, the laser interferometric displacement sensor, is also described. Three common examples of interferometers are presented. The pros and cons of each sensor are highlighted.

Chapter 3 describes a novel high precision position sensor for motion control. A laser interferometric displacement sensor with 3×3 coupler and resolution enhancement is constructed and studied. The detailed configuration, mathematical equations, and operating principle of this novel displacement sensor are also described. A resolution enhancing circuit is constructed to modify the outputs of interferometer to provide interface of conventional encoder. The proposed methods have been investigated by building the prototype and conducting measurement experiments. Finally, the experimental results are also shown and analyzed.

In chapter 4, the limitations of the optical linear incremental encoder are identified through reviewing of the operation of decoder. In order to overcome this limitation, the data fusion algorithm is used. The basic concepts and the algorithms are also studied and presented.

Chapter 5 presents a novel resolution increasing circuit to improve the maximum measurement speed of the incremental encoder. The operation of the resolution increasing circuit is described. The prototype of the circuit is developed and its performances are illustrated in this chapter. Meanwhile, the limitations of the resolution increasing circuit are also observed from the experimental results. The data fusion algorithm is used to further improve the output of resolution increasing circuit. The performances of the improved methods are investigated and the results are described also shown in this chapter.

The basic concepts and theories of control algorithms and drives are investigated in chapter 6. Linear actuators can be divided into direct drive and indirect drive motion system. The pros and cons of these two systems are investigated and described. There are many the problems (including force ripple phenomenon, friction, model uncertainties, and load variations) which have to be encountered during the development of high precision linear motion system. Those mentioned problems are described and investigated in this chapter. The PMLM is the target actuator studied in this thesis. The scalar model and vector model of the PMLM are reviewed and the typical control algorithms for PMLM to achieve high precision motion system are also presented.

In chapter 7, a novel modified disturbance observer and compensator are developed and an internal model reference control (IMRC) algorithm is formulated for the high precision linear motion control. Equations of the conventional and modified compensation algorithm are derived and explained. After the implementation of disturbance compensation, non-linearity characteristics of PMLM such as friction, ripple force, variation of model parameters, load change, and external force disturbance are also compensated. The IMRC control algorithm is adopted to control the compensated PMLM to be a high precision controlled motion system. The prototype for illustrating the proposed approach is constructed and the experimental results validate the usefulness of the disturbance compensator and the IMRC algorithm. In addition, the experimental results of modified disturbance compensators and the original compensator are compared. This comparison also illustrated that the modified disturbance compensator can further improve the ability of the disturbance compensator.

The last chapter highlights the main contributions and achievements of the thesis. Some remaining issues and interesting conclusions within the context of the thesis are also suggested for further research.

1.3 Summary of contribution

This research project has made the following contributions:

Contribution 1: A novel laser interferometric displacement sensing system with 3×3 fiber coupler is proposed. The operating principles, theories and performances of interferometer with 3×3 fiber coupler are reviewed and the idea of this interferometer is employed to achieve a high precision linear motion sensor. The outputs interface conversion for generic industrial decoder is also presented. The position sensor can achieve a displacement measurement resolution of 95.5nm.

Contribution 2: The novel resolution increasing circuit and the data fusion algorithm are employed to enhance the measurement speed of the optical linear incremental encoder. The outputs of optical linear incremental encoder are modified by another delicate circuit, so that the new outputs from the circuit can provide double resolution and double maximum measurement speed compared with original optical linear incremental encoder. These two sets of signals are merged to achieve a velocity measuring system with wider measurement speed range and high precision measurement. The prototype of the delicate circuit is constructed and the feasibility of the proposed method is corroborated.

Contribution 3: A control strategy for PMLM to achieve high precision controlled motion is proposed. The non-linearity such as friction, external forces, and perturbation of motor parameters are compensated by a novel modified disturbance compensator. This disturbance-free linear motion system is controlled by IMRC, so that the PMLM can track in a predefined manner. By combining the benefits of compensation method and IMRC, the compensated and controlled PMLM realizes a high precision linear motion with a steady state error deviation less than 0.1μm.

Chapter 2
Background studies on high precision linear motion sensor

High precision motion sensor is one of the essential components in controlled linear motion system. Typical examples of linear motion sensors are the optical linear incremental encoder and the laser interferometric displacement sensor.

2.1 The optical linear incremental encoder

Optical linear incremental encoder is a non-contact and frictionless measuring system [6]. It can assist the achievement of speedy and accurate linear motion system. This type of motion sensor will be utilized in this thesis. Therefore, the operation of it is explained in this section. One example of commercial products manufactured by Renishaw is shown in Fig.2-1.

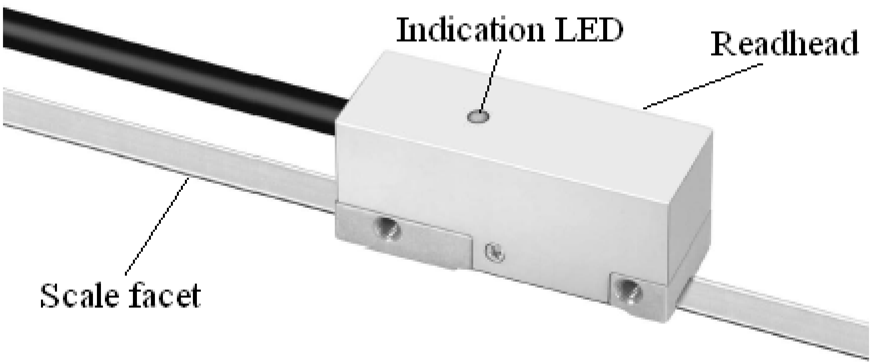

Fig.2-1 Appearance of an optical linear incremental encoder [7]

This displacement sensor is based on the reflective measuring mechanism, as illustrated in Fig.2-2. Generally, the readhead is installed on the translator and the scale facet is installed on the flat surface of the stator. The LED emits light onto the scale facet which reflects the light back to the detectors in the readhead. The reflected light will form a bright and dark pattern at the level of the readhead. If the readhead is located at a different position, the pattern will vary with the location of the readhead. Based on the received light from the readhead, photo-detectors and encoding electronics circuit will generate the different output values which are in quadrature incremental pulse format. Note that the gold plated the scale is lacquer coated so that scale facet can be protected, installed, and maintained easily.

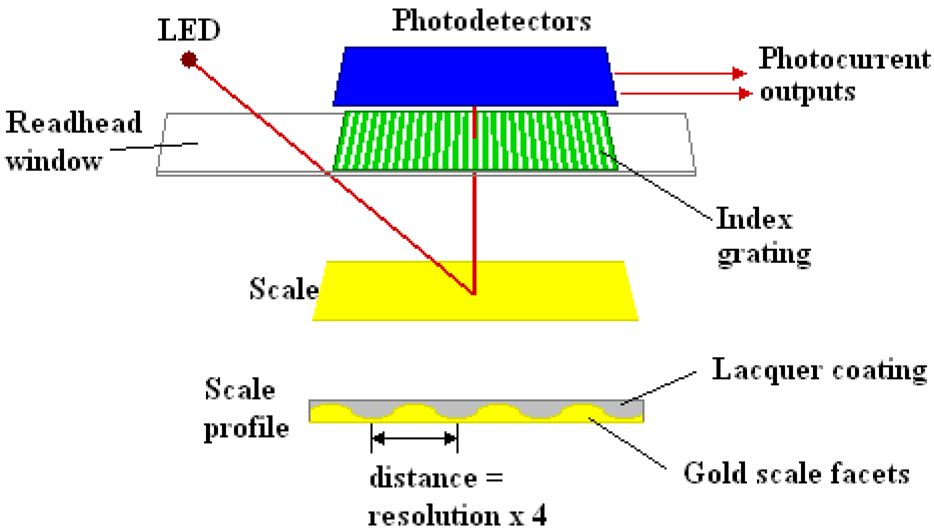

Fig.2-2 Operation of the optical linear incremental encoder

2.2 Encoding and decoding of incremental pulses

Fig.2-3 explains the operation of the quadrature signals. Phase A and Phase B signals vary with the measured position. The signals assignment can be generated by optical and magnetic means. Note that Phase A and Phase B are the function of position, as shown in Fig.2-3(a). When the measured object is moved with the profile shown in Fig.2-3(b), quadrature signals from encoder is generated, as shown in

Fig.2-3(c). It is obvious that the frequencies of the both phases are related to the velocity of the movable target.

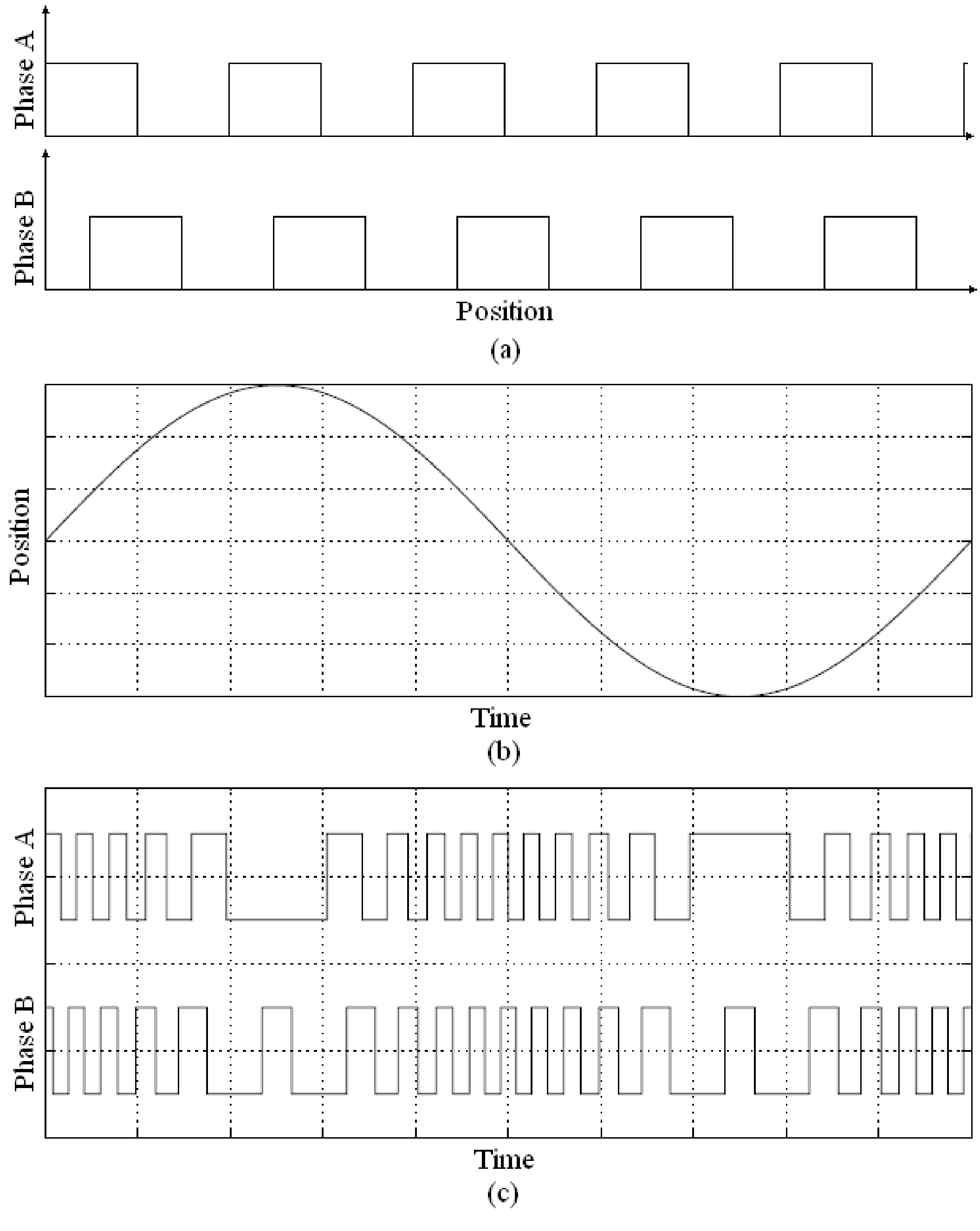

Fig.2-3 Generation of quadrature signals; (a) relationship between the Phase A, Phase B and the position; (b) position time graph; (c) the corresponding Phase A and Phase B for (b)

The encoded signals Phase A and Phase B contain information of traveled distance and direction [6]. The combination of signals can be classified as four different stages:

(1) “A high B low”

(2) “A high B high”

(3) “A low B high”

(4) “A low B low”

The stage of signals is monitored by a high speed decoder circuitry. When the stage is changed from one state to another, the position count is added or subtracted, depending on the sequence of the monitored stage. Fig.2-4 illustrates the sequence of the stages. If the stage changes in solid arrows sequence, the position count will be incremented. The count will be decremented if sequence follows hollow arrow. Note that high speed data sampling in the incremental decoder circuitry is necessary and the sampling frequency should be at least four times higher than the frequency of Phase A and Phase B. Since the frequencies of both phases are proportional to the velocity of the movable target, and the sampling frequency of the decoder is usually limited, the maximum measurement speed is therefore confined to this limitation.

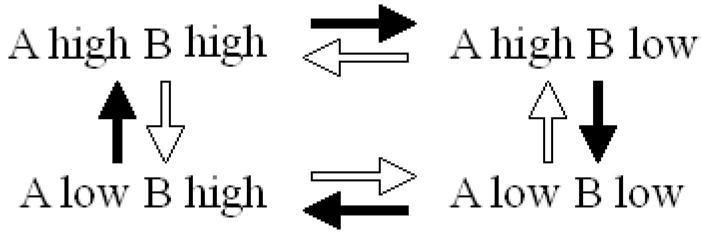

Fig.2-4 Stage sequence of quadrature signals.

2.3 The laser interferometric distance sensor

Compared with the optical linear incremental encoder, the fiber-optical interferometer is more popular for high precision short stroke applications, such as position sensor of CD-ROM read-head, and some engineers prefer utilizing laser interferometer to measure the position of the actuator in a high precision motion system. The resolution of a laser interferometer displacement sensor is related to the wavelength of the laser source, which is down to sub-micron level. Therefore, this sensor is suitable for implementing into a high precision linear motion controlled system. In addition, the fiber optical sensor is suitable for harsh working environment and the entire sensor cost is usually lower.

Laser interferometer is a kind of phase-modulated sensor. Generally, phase modulation sensors utilize a coherence light source which is split into two light beams. One of the light beams undergoes phase modulation from the environment perturbation, which is related to the value of the measuring parameter. Another light does not have any modulation. The two light beams are combined and superimposed to generate a resultant output light beam. The intensity of output of the interferometer will be varied with the measuring parameter. This phase modulation mechanism can be employed to measure the displacement of an object at a high resolution.

A simple configuration of interferometer is shown in Fig.2-5 [8]. A laser diode generates a coherence laser light beam, which is propagated along the fiber through an optical isolator. The optical isolator blocks the reflected light so that operation of the laser diode is not disturbed. This light beam is then split by a light splitter (e.g. a 2×2 fiber coupler). One light beam propagates along the reference arm and then reflected by a fixed reflecting mechanism. Another light leaves the fiber and travels along the air and it is reflected by the movable target. These two reflected light beams superimpose inside the light splitter. The resultant light beam is projected on the photodiode which is responsible for detecting the light intensity of the received light. The photodiode will then convert the light intensity into an electrical signal.

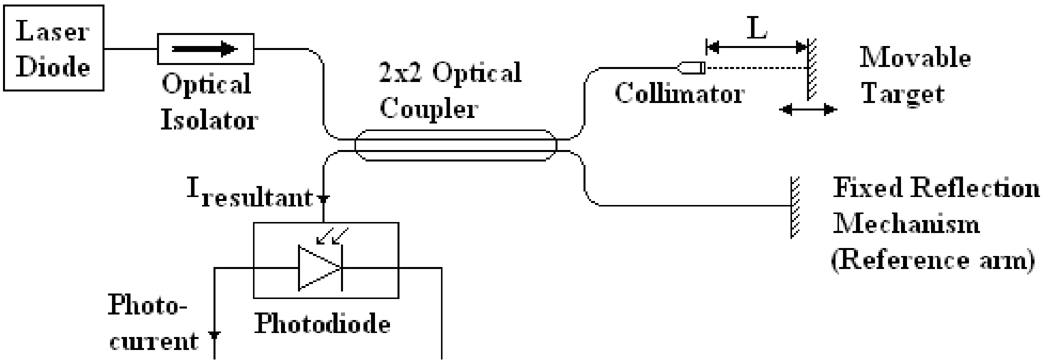

Fig.2-5 Configuration of a two-beam interferometric displacement sensor

The resultant light intensity $I_{resultant}$ can be formulated as shown in (2.1)

$$I_{resul\tan t} = I_{avg} + I_{amp}\cos(\frac{4\pi L}{\lambda} + \varphi) \tag{2.1}$$

where I_{avg} is DC offset of this sinusoidal $I_{resultant}$

I_{amp} is the amplitude of the sinusoidal $I_{resultant}$

φ is initial phase difference when L is zero

λ is wavelength of the laser in vacuum

The traveled distance ΔL can be measured by the following equations if the movement is less than $\lambda/4$:

$$\Delta L = \frac{\lambda}{4\pi}[\cos^{-1}(\frac{I_{final} - I_{avg}}{I_{amp}}) - \cos^{-1}(\frac{I_{initial} - I_{avg}}{I_{amp}})] \qquad (2.2)$$

(2.2) can measure the traveled distance within the displacement length of $\lambda/4$ only, because of the periodic nature of a cosine function. If the traveled distance is longer than $\lambda/4$, the method shown in Fig.2-6(a) and Fig. 2-6(b) can be used. The initial intensity $I_{initial}$ is measured and recorded. The intensity of resultant light beam is checked continuously and its number of turning point is also examined. When the movable target is stopped the final intensity I_{finial} is also recorded. These three data can be collected and converted to position information (L_1, L_2, and L_3). They can be added together so that the traveled distance can be calculated. Note that the accuracy and the resolution of the sensor depend on the wavelength of laser.

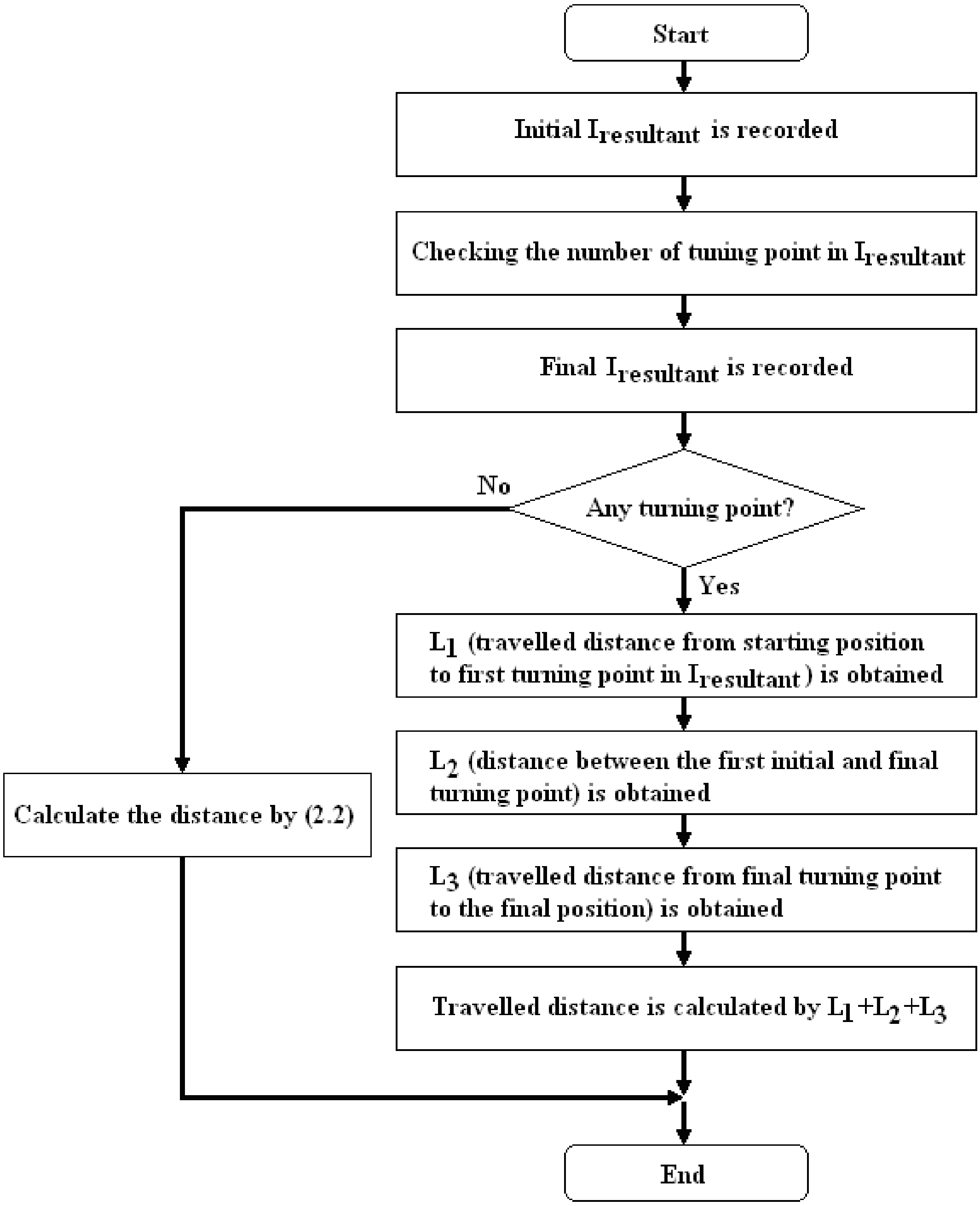

Fig.2-6(a) Measurement algorithm of general interferometric displacement sensor

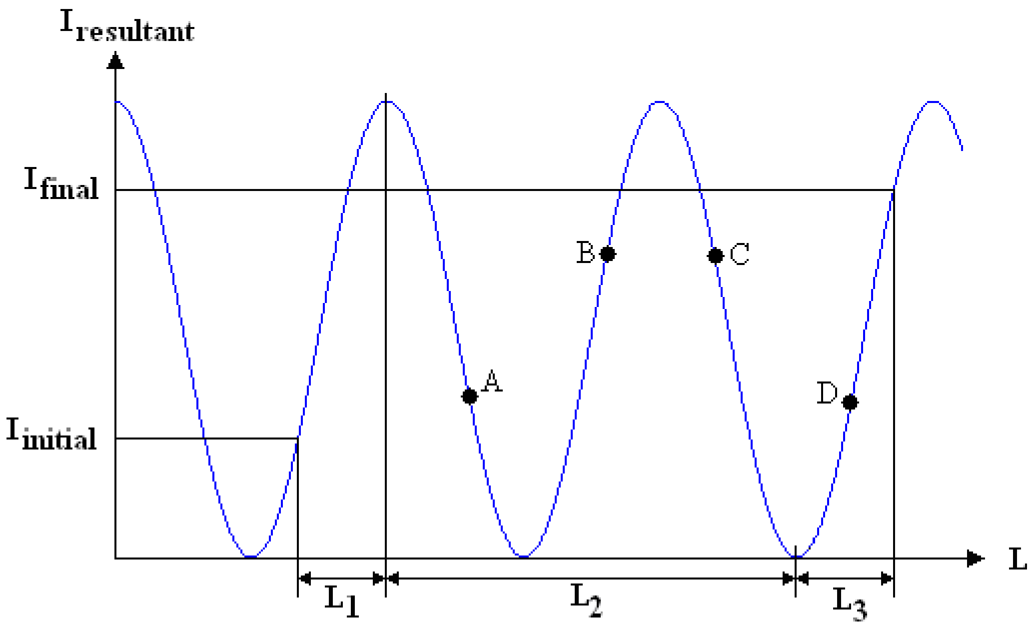

Fig.2-6(b) Resultant intensity and variable assignment for method explanation

This approach has an undeniable disadvantage when it is directly applied to linear motion control. When the movable target is moving in the negative direction, the photodiode receives the light intensity varying from point B to point A, as shown in Fig.2-6(b). On the other hand, if the target moves in the positive direction, the measured intensity will vary from point C to point D. Although the moving directions in these two cases are different, the intensity varying patterns are same for both cases and there is no evidence to illustrate the moving direction of the target. To conclude, the output of this approach can not determine the moving direction of the target.

2.4 The laser interferometric displacement sensor

Many engineers proposed different modifications on the basic form of interferometer so that the traveling direction of movable target can be obtained. Those modifications can be summarized as follows:

2.4.1 Self-mixing interferometer

[9] and [10] show a kind of interferometer which utilizes the laser cavity to act as the region for superimposing the reflected light beams. Fig.2-7(a) shows the configuration of a self-mixing interferometer. The resultant light beam is detected by the embedded photodiode located near the back facet of the laser. The photocurrent from the photodiode is converted to electrical voltage by the trans-impedance amplifier and it is then further processed by different signal processing stages. The relationship between actual position and output of trans-impedance amplifier is shown in Fig.2-7(b). A saw-tooth like waveform can be obtained. The slope of the waveform is related to the direction of the movable target. This saw-tooth like waveform can be differentiated and converted to displacement information by an up-down counter. Note that the level of feedback parameter C is controlled by a variable attenuator and C has to be moderate ($1<C<4.6$) so that a saw-tooth waveform can be generated.

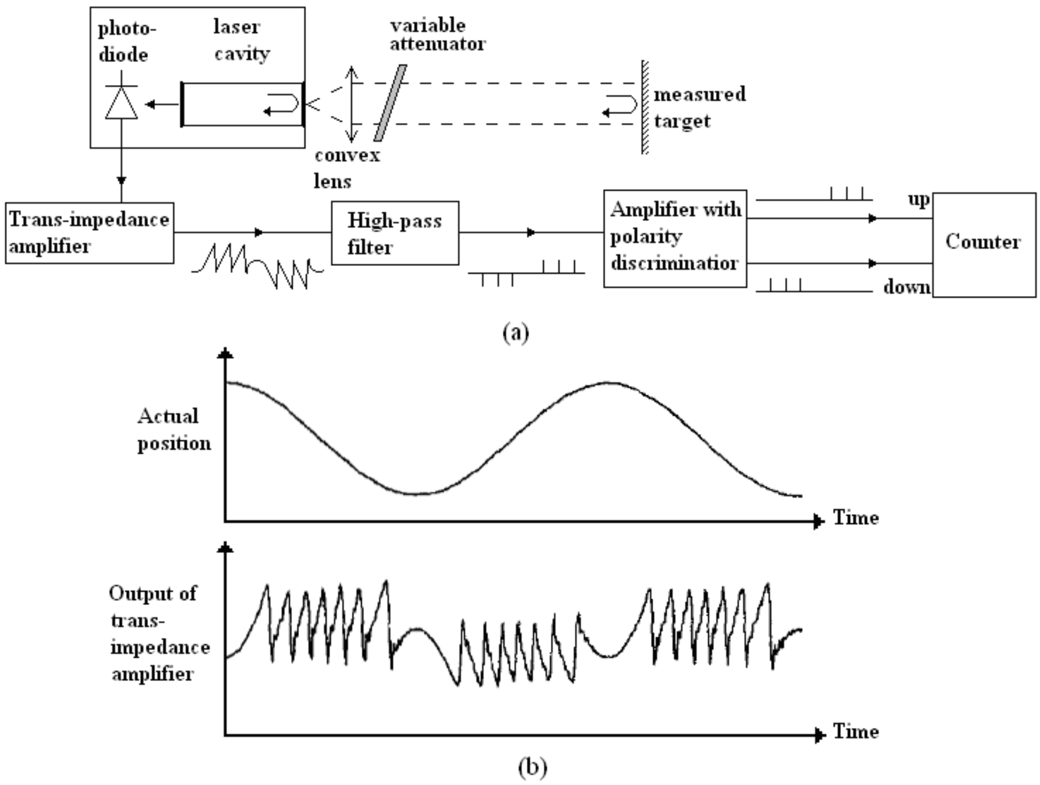

Fig.2-7(a) Configuration of a self-mixing interferometer; (b) Relationship between actual position and output of trans-impedance amplifier

This type of interferometer requires additional control of the attenuator to adjust the parameter *C*. In addition, this feedback mechanism will result in laser frequency fluctuation. Controlling the fluctuation in laser frequency plays a very important role in the performance of these sensors [11]. These control procedures are difficult, time-consuming, and definitely increases the cost of the sensor.

2.4.2 Interferometer with polarization

Light wave contains two orthogonal components (E_x and E_y). Some engineers utilized these two components to develop a displacement sensor. An optical device called wave-plate or retardation plate, which governs the speed of light wave components along the fast-axis and slow-axis, introduces a phase difference between the two components. This device is utilized in an interferometric displacement measurement system. Fig.2-8(a)-(c) show the three types of polarization interferometer [12-14].

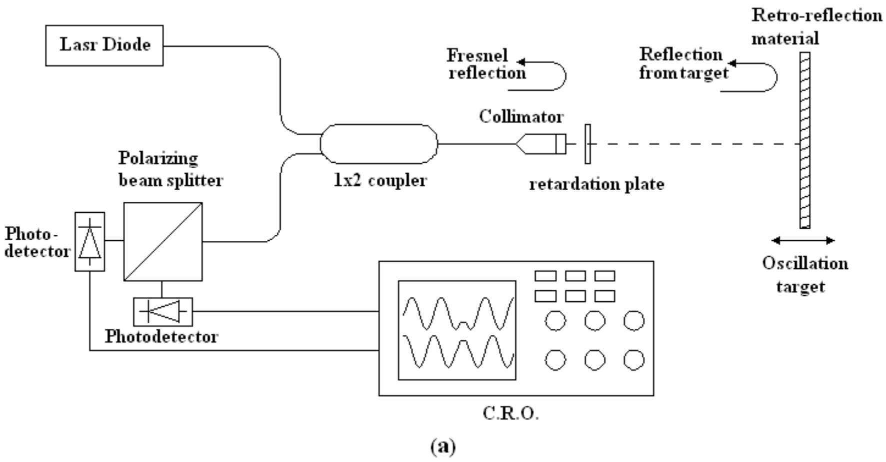

Fig. 2-8(a) Polarization interferometer used in [12]

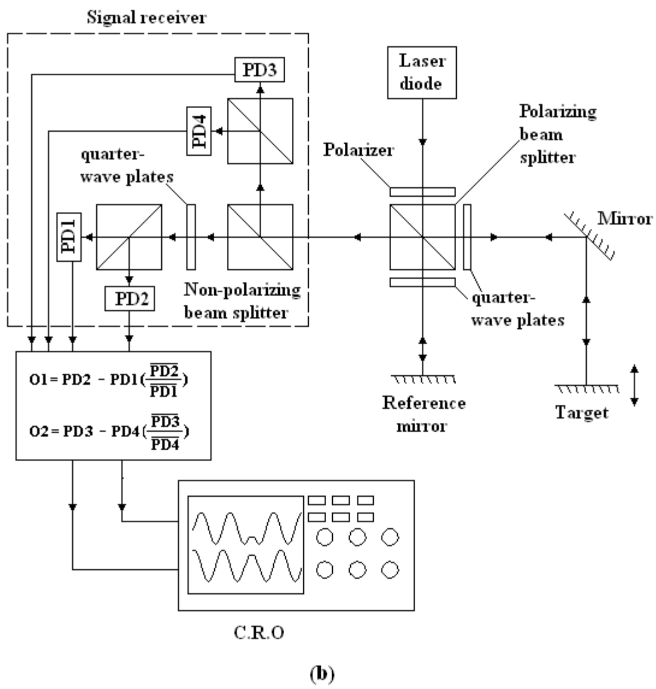

Fig. 2-8 (b) Polarization interferometer used in [13]

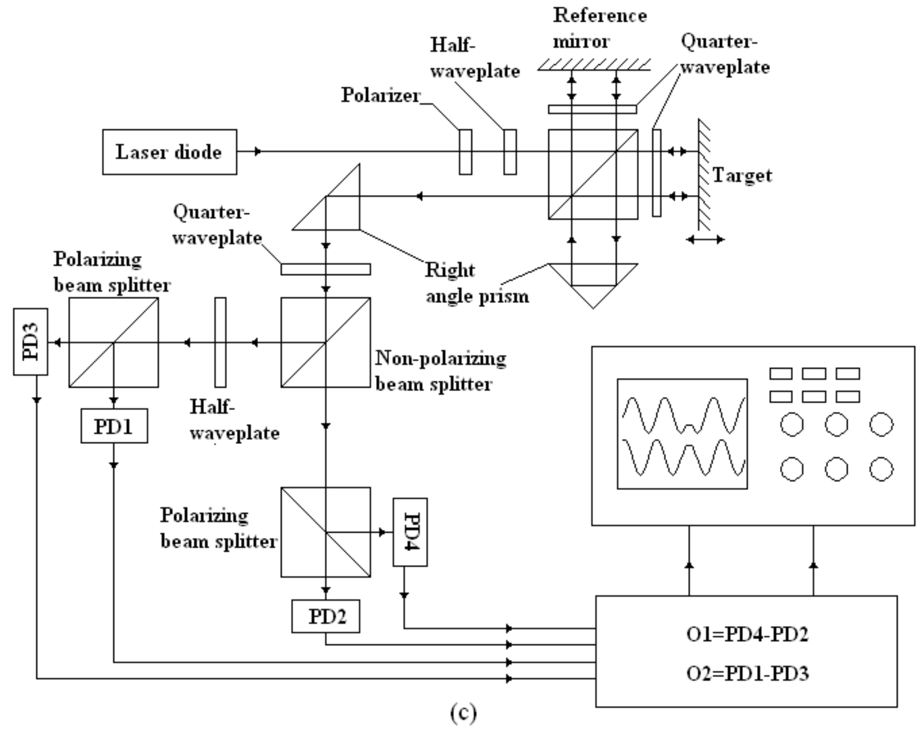

Fig. 2-8 (c) Polarization interferometer used in [14]

The light beams which are reflected from the reference position and the moving target are joined inside the interferometer. The resultant light beam contains its own E_x and E_y and their converted intensities are the functions of the position of the moving target. The components of light beams can be decomposed by an optical device called polarizing beam splitter. With suitable signal processing among the decomposed signals, the polarization interferometer can develop two quadrature sinusoidal signals. The leading or lagging relationship of these two components is related to the traveling direction of the target. This can be employed for extracting the displacement information.

Although this type of interferometer can generate the quadrature analogue signals, which can be directly applied to a generic incremental decoder, the light beams alignment and size of sensor are the main challenges of constructing this high precision motion control. As illustrated in Fig. 2-8, the light beams need to be projected perpendicular to the surface of the polarizing beam splitter cube. The number of alignment will increase the difficulty of sensor construction. Also, compared with other interferometers, the space occupied by the polarization interferometer is much more because of big polarizing beam splitter cubes.

2.4.3 LED driven interferometer with a 3×3 coupler

2×2 fiber coupler usually provides single output fiber to deliver the superimposed signal and the sinusoidal output from this output fiber does not contain the direction information. Another optical device which is 3×3 fiber coupler can overcome the problem of single output fiber. This device involves two output fibers to deliver two sinusoidal signals varying with the displacement of the movable target. The phase difference between these two signals is 120^o. Therefore, the direction of moving target can be obtained based on these phase relationship. Some engineers applied this device and LED sources to develop a displacement sensing systems [15, 16] and these systems are successfully achieving the high precision positioning measurement system.

This novel interferometer with 3×3 coupler seems to be the most suitable for feedback sensor of high precision linear motion control. However, some new and high speed position decoding methods are required in order to convert two signals with 120^o phase difference into position. The complicate decoding method will raise the cost and difficulty of the sensor. In addition, the coherence length of LED source is short, so the displacement sensors presented in [15] and [16] can only perform measurements over short distances.

2.5 Summary

In this chapter, the operation principles of high precision displacement sensors are discussed. The sensors investigated include the optical linear incremental encoder and the laser interferometric displacement sensor.

Optical linear incremental encoder is commonly employed in high precision linear motion system. It is because the resolution of the sensor can go down to submicron level. The operation of an incremental encoder has already been mentioned (including the output signals encoding and stage sequence). The decoding method and its limitation are also explained.

After substantial improvements, some types of laser interferometric displacement sensors have the potential to become displacement sensors utilized in high precision motion control. This is because the resolution of the sensor, which depends on the wavelength of the laser source, can comfortably go down to sub-micron level. Different configurations of laser interferometric displacement sensors have been reviewed.

This literature review shows that an accurate, low cost, and with better resolution linear displacement sensor for the manufacturing industry is not easy to achieve. One of the feasible and potential suggestions for high precision displacement measuring is laser interferometric displacement sensor with a 3×3 coupler. The high precision and resolution of the interferometer depends on the wavelength of the laser source and the resolution can go down to submicron level.

This motivates the author to develop a low cost and high precision sensor based on laser interferometer. The sensor in the following chapter has a novel configuration. It is simple in construction, and it can be installed and aligned very easily.

Chapter 3
A novel laser interferometric displacement sensor for sub-micron precision control

A “3×3 fiber coupler” is utilized to construct a displacement sensor with simple structure. The outputs of the displacement sensor are modified so that their interfaces can compatible with conventional motion controllers (with incremental signal outputs). Furthermore, a high coherence laser light source is employed in order to extend the range of measurement.

3.1 Configuration of displacement sensor

Fig.3-1 shows the structure of the interferometric displacement sensor made with a 3×3 fiber coupler.

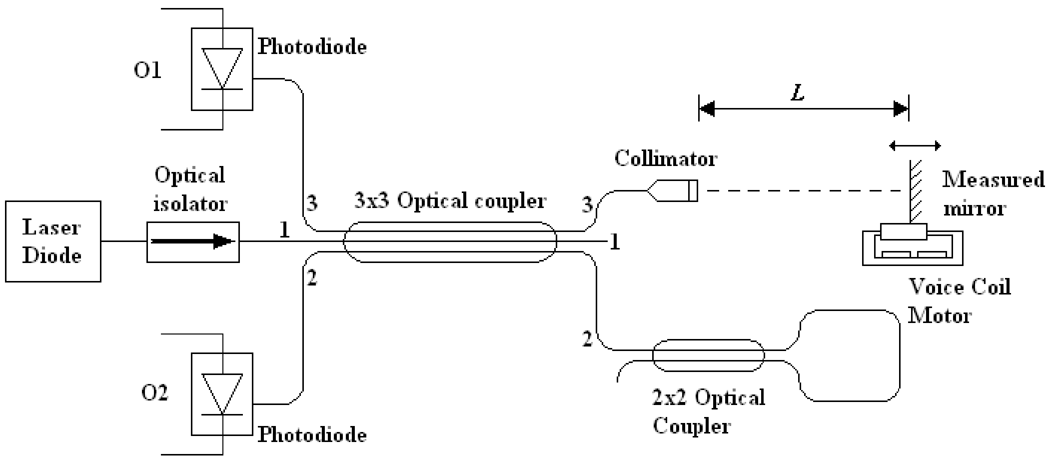

Fig.3-1 Configuration of interferometric displacement sensor with a 3×3 fiber coupler

A laser diode is employed to generate single wavelength laser light which is injected into the 3×3 fiber coupler through an optical isolator. The laser light is coupled to three output channels with the same ratio (the coupling coefficients between each waveguide are the same). The fiber end of output port in channel 1 is coated with an anti-reflection layer. This is aimed to reduce the effect of the Fresnel reflection (fiber-end reflection), so that the signal from channel 1 will not be reflected back into the coupler. Note that the laser light in channel 1 output is not used in this configuration.

The light beam in output channel 2 leaves the fiber end through a collimator and projects onto the moving target (mirror installed on the voice coil motor). The collimator is responsible for collimating the light beam from the fiber, so that the parallel light beam can be produced and the light alignment will be easier. This light beam travels for distance L (from collimator to movable target) and is then reflected back to the fiber with the same distance L (from the movable target to the collimator). Another light beam in channel 3 is reflected by the fixed reflecting mechanism called the fiber loop reflector [17]. Note that this reflected light beam acts as a reference light beam. Both reflected beams from output channel 2 and 3 are superimposed inside the optical coupler. The resultant light beam is coupled back to input channels for displacement measurement.

Note that the function of the optical isolator is blocking the light beams entering the laser diode. The reflected light beam in input channel 1 is blocked so it can be neglected. The coupled light beams in inputs channel 2 and 3 are utilized for position measurement. Based on these two optical signals (O_1 and O_2) which will vary with position of the moving target, the displacement (ΔL) of the target can be obtained from these two signals. The intensities of these two signals are detected by two photodiodes which are responsible to convert the optical signals into electrical signals.

3.2 Equations of interferometric displacement sensor

The basic operation of the interferometer with 3×3 fiber coupler has been explained in [18] and [19]. Fig.3-2 shows an unfolded form of interferometer and this illustrates the principle of the interferometer. The 3×3 fiber coupler is governed by a set of linear differential equations as shown below:

$$\begin{cases} \dfrac{da_1}{dz} + iK_{12}a_2 + iK_{13}a_3 = 0 \\ \dfrac{da_2}{dz} + iK_{23}a_3 + iK_{21}a_1 = 0 \\ \dfrac{da_3}{dz} + iK_{31}a_1 + iK_{32}a_2 = 0 \end{cases} \tag{3.1}$$

where a_j is complex amplitude of three waves in 3×3 coupler, where j=1,2, and 3

K_{kj} is the coupling coefficient between the k-th and j-th waveguide. For 33:33:33 fiber coupler, $K_{kj} = K_{jk} = K$

i is $\sqrt{-1}$

z is the position of coupler

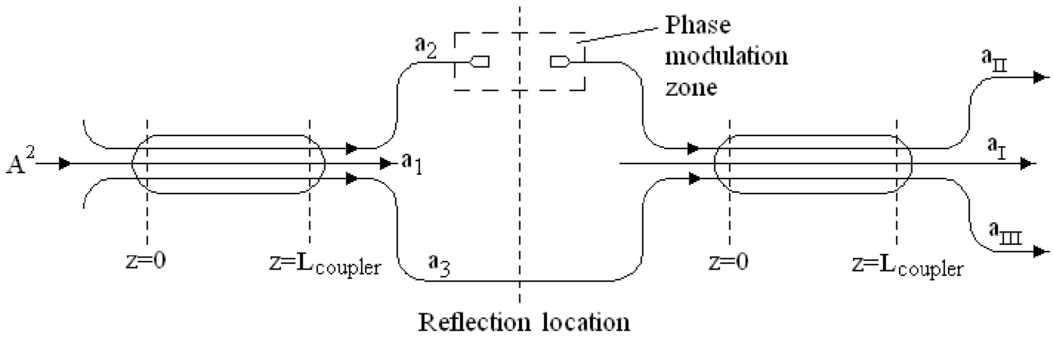

Fig.3-2 Unfolded form of interferometer with 3×3 coupler

When the laser light with input power A^2 is injected into the coupler, the initial condition of the linear differential equations for the first coupler is:

$$a_1(0) = A,\ \ a_2(0) = 0,\ \ a_3(0) = 0$$

The three complex amplitudes of the first coupler can be solved as shown in (3.2). The corresponding output intensities of the coupler ($z = L_{coupler}$) are shown in (3.3)

$$\begin{cases} a_1 = \frac{2}{3}Ae^{iKz} + \frac{1}{3}Ae^{-2iKz} \\ a_2 = \frac{1}{3}Ae^{iKz} + \frac{1}{3}Ae^{-2iKz} \\ a_3 = \frac{1}{3}Ae^{iKz} + \frac{1}{3}Ae^{-2iKz} \end{cases} \tag{3.2}$$

$$\begin{cases} \left|a_1(L_{coupler})\right|^2 = A^2 - 2\left|a_2(L_{coupler})\right|^2 \\ \left|a_2(L_{coupler})\right|^2 = \frac{2}{9}A^2(1-\cos 3KL_{coupler}) \\ \left|a_3(L_{coupler})\right|^2 = \frac{2}{9}A^2(1-\cos 3KL_{coupler}) \end{cases} \tag{3.3}$$

where $L_{coupler}$ is the coupler length

The phase of light beam in the second output fiber of the first coupler is modulated by the position of moving object. The additional phase related to the position of movable target is added to the light beam in the second fiber. Comparing both inputted light beams in second and third fiber of the second coupler, their phase difference ϕ is shown in (3.4). Note that the θ in (3.4) is the initial phase difference between the light beam in second and third fibers.

$$\phi = \frac{4\pi L}{\lambda} + \theta \tag{3.4}$$

where L is the distance between the mirror and collimator

λ is wavelength of the light beam

After the phase modulation is taken place, the two light beams are injected to second coupler with the initial condition as:

$$a_I(0) = 0,\ \ a_{II}(0) = \frac{B}{\sqrt{2}} e^{i\phi},\ \ a_{III}(0) = \frac{B}{\sqrt{2}}$$

where B^2 is $2\times|a_2(L_{coupler})|^2 = 2\times|a_3(L_{coupler})|^2$

Similar to the operation of the first coupler, the outputs of the second coupler can be solved as shown in (3.5)

$$\begin{cases} \left|a_I(L_{coupler})\right|^2 = \dfrac{2}{9}B^2(1-\cos 3KL_{coupler})(1+\cos\phi) \\ \left|a_{II,III}(L_{coupler})\right|^2 = \dfrac{1}{18}B^2[(7+2\cos 3KL_{coupler}) \\ -2\cos\phi(1-\cos 3KL_{coupler}) \mp (6\sin\phi \sin 3KL_{coupler})] \end{cases} \tag{3.5}$$

Note in (3.5) that $|a_{II}|$ takes the minus sign and the $|a_{III}|$ takes the plus sign. The output from second and third fibers (O_1 and O_2) can be used as the signals for measuring the displacement. By measuring these two signals, the displacement of the movable target can also be obtained. The intensities of O_1 and O_2 are plotted in Fig.3-3 and they are based on the fact that the $KL_{coupler} = 30^o$ since a 33:33:33 optical coupler is employed. In addition, O_1 and O_2 are the function of phase difference ϕ and the distance between collimator and movable target L. This is also illustrated in Fig.3-3.

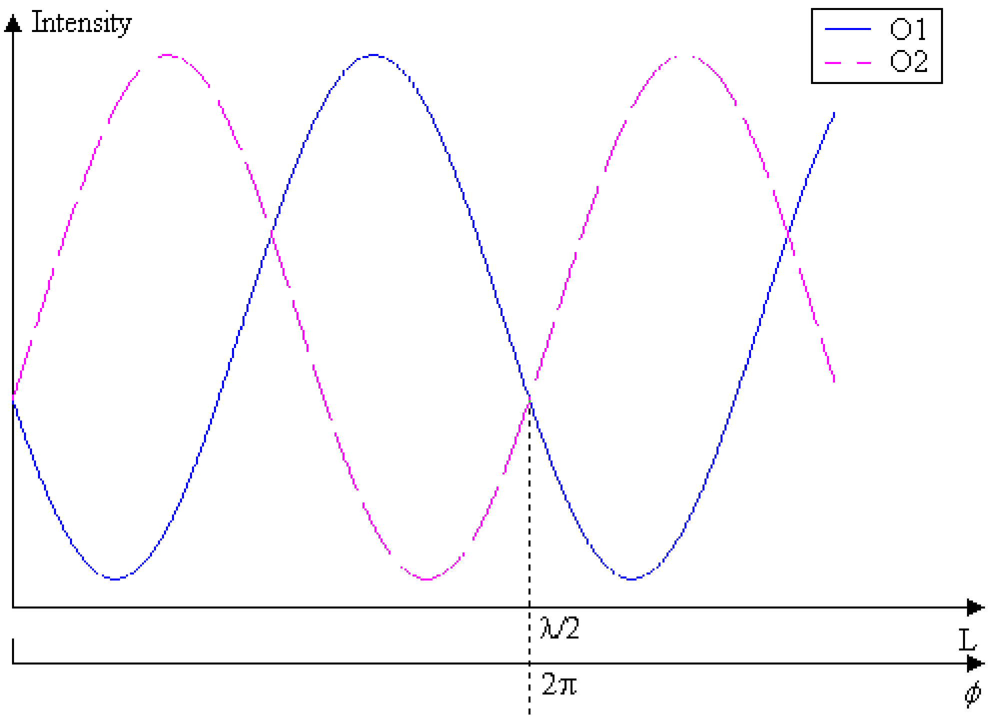

Fig.3-3 Intensity plot of O_1 and O_2

Note that the phase difference between O_1 and O_2 are 120^o and they are not in quadrature.

3.3 Output modification and resolution enhancement scheme

In general, the outputs of the interferometer are directly converted to square wave pulses for high precision displacement measurement. Assume the offsets of optical signals O_1 and O_2 can be removed and they become signals O_1' and O_2'. These two offset eliminated signals are converted to digital pulses by comparing with zero. Digital signals of O_1' and O_2' are shown in Fig.3-4.

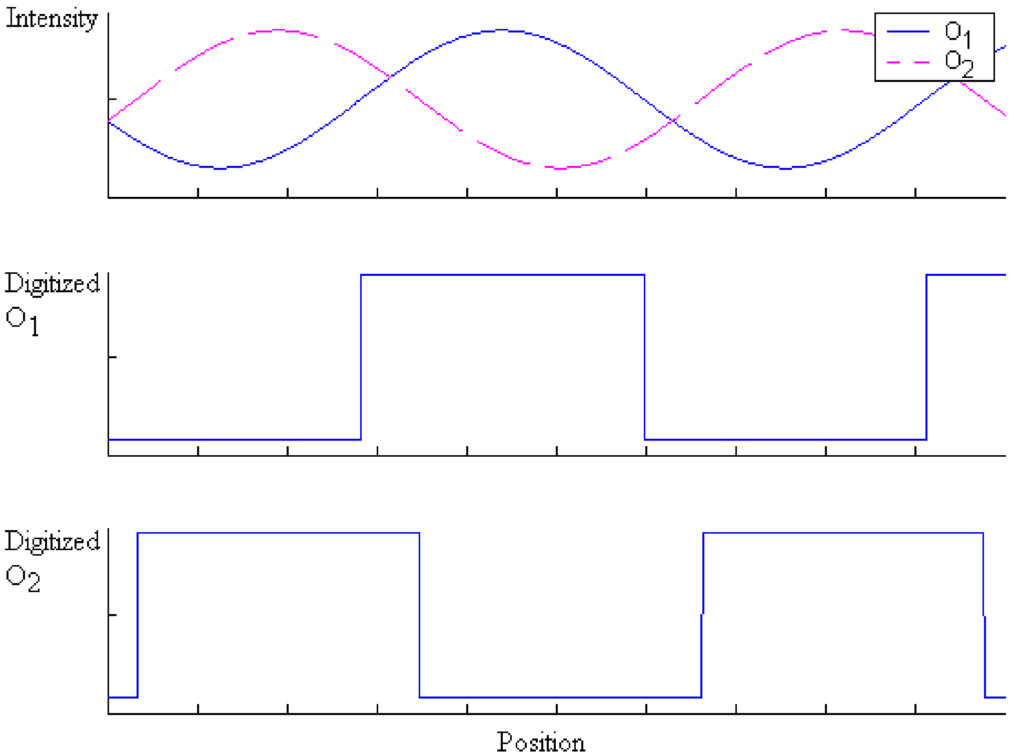

Fig.3-4 Digital signals obtained from O_1' and O_2'

Although the digital signals are capable for displacement measurement (by counting the number of pulses and determining the phase relationship, with a resolution of $\lambda/2$), these sensor outputs are not suitable for the conventional industrial controller since the square waves are not quadrature in nature.

In this project, the outputs of the interferometer with a 3×3 fiber coupler are modified to another set of signals which is suitable for the generic industrial controller interface. By doing this, the resolution of the modified sensing system can be enhanced.

3.3.1 Explanation of resolution enhancement scheme by Lissajous figure

Consider the two signals O_1' and O_2' with their offset removed:

$$O_1' = \frac{1}{18}B^2[(-2\cos\phi(1-\cos 3KL_{coupler}) - (6\sin\phi\sin 3KL_{coupler})]$$
$$O_2' = \frac{1}{18}B^2[-2\cos\phi(1-\cos 3KL_{coupler}) + (6\sin\phi\sin 3KL_{coupler})] \tag{3.6}$$

O_1' and O_2' are varying with the position of the movable target. These two signals can be utilized to plot the Lissajous figure as shown in Fig.3-5. If the signal point travels a completed ellipse, this is equivalent that the movable target move a distance λ/2. In addition, the rotating direction of the signal point is changing with the traveled direction of movable target. In order to enhance the resolution of the sensor, the slanting ellipse is further divided into eight different sectors by the following equations:

$$O_1' = O_2'$$
$$O_1' = -O_2'$$
$$O_1' = -2O_2' \tag{3.7}$$
$$O_1' = -\frac{1}{2}O_2'$$

Although the lengths of different arcs, as shown in Fig. 3-5, are not equal, the equivalent traveled distances of the measured object are the same. This fact is also illustrated in Fig. 3-6. In fact, the equations shown in (3.7) can be modified as a resolution enhancement method.

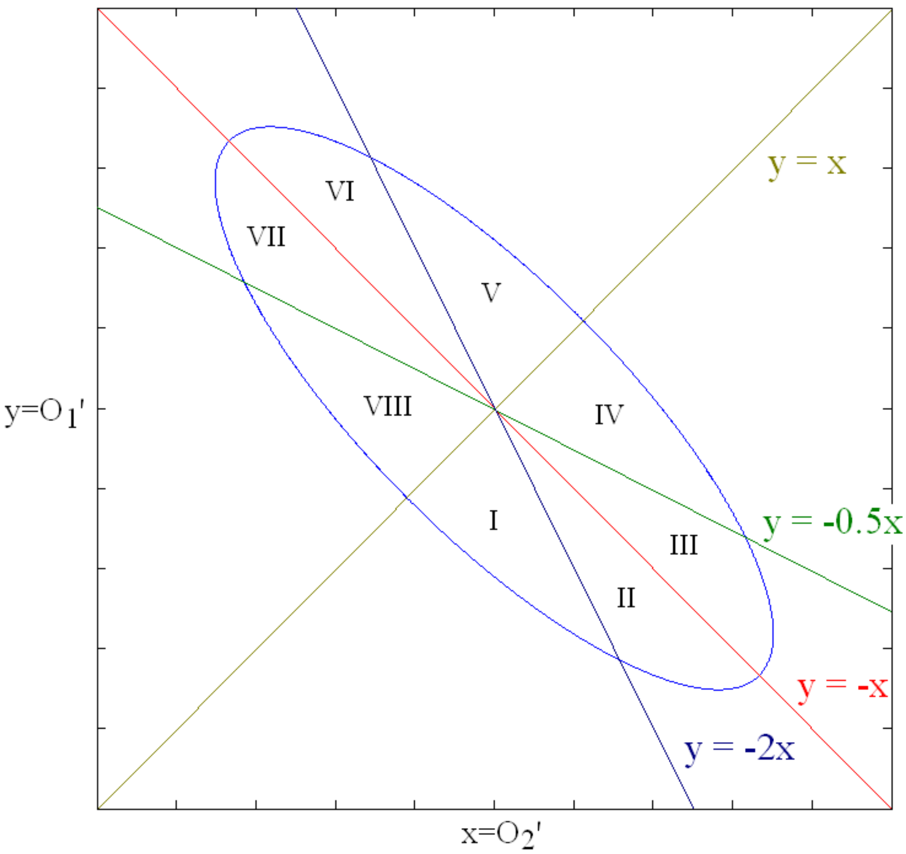

Fig.3-5 Lissajous figure with inputs signals O_1' and O_2'

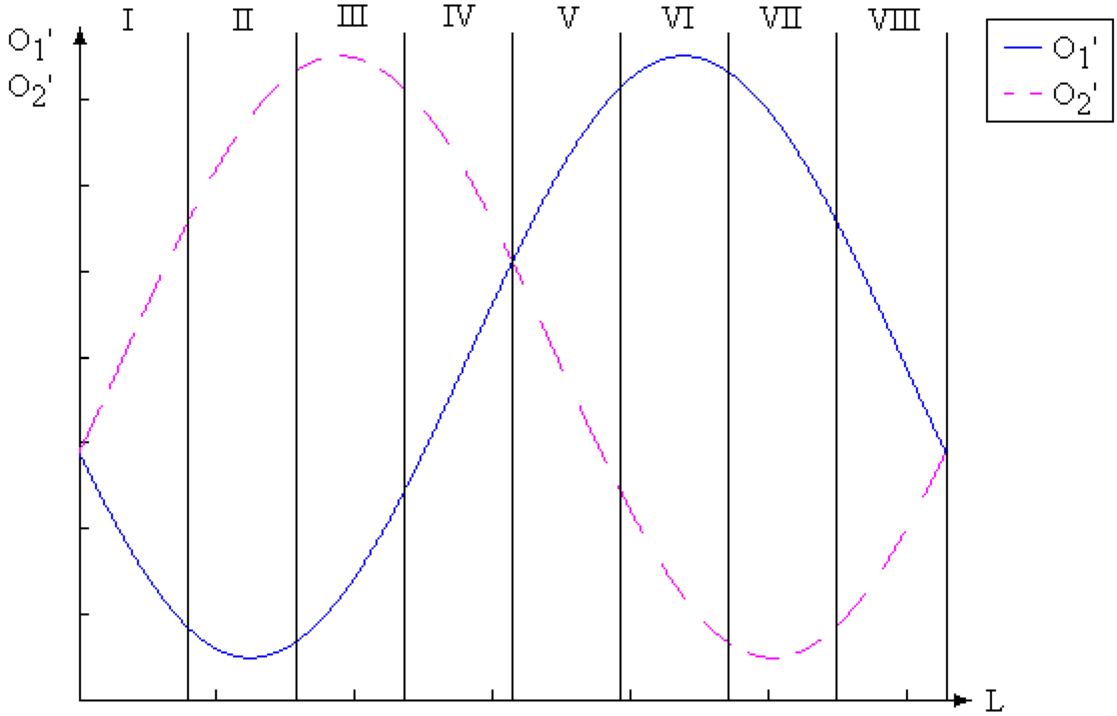

Fig.3-6 Eight sectors indication with O_1' and O_2'

If O_1' and O_2' are compared with different conditions, quadrature signals can be obtained. If O_1' and O_2' are compared with the criteria as shown in (3.8) and (3.9), two quadrature digital signals (S_1' and S_2') can be obtained and they are shown in the first two panels of Fig. 3-7.

$$S_1' = \begin{cases} 1 & for \quad O_1' > -O_2' \quad (III, IV, V, VI) \\ 0 & for \quad O_1' < -O_2' \quad (I, II, VII, VIII) \end{cases} \tag{3.8}$$

$$S_2' = \begin{cases} 1 & for \quad O_1' > O_2' \quad (V, VI, VII, VIII) \\ 0 & for \quad O_1' < O_2' \quad (I, II, III, IV) \end{cases} \tag{3.9}$$

Two comparing criteria as shown in (3.10) and (3.11) can generate another two quadrature digital signals (S_3' and S_4') and they are also shown in Fig. 3-7.

$$S_3' = \begin{cases} 1 & for \quad 2O_1' > -O_2' \quad (IV, V, VI, VII) \\ 0 & for \quad 2O_1' < -O_2' \quad (I, II, III, VIII) \end{cases} \tag{3.10}$$

$$S_4' = \begin{cases} 1 & for \quad O_1' > -2O_2' \quad (II, III, IV, V) \\ 0 & for \quad O_1' < -2O_2' \quad (I, VI, VII, VIII) \end{cases} \tag{3.11}$$

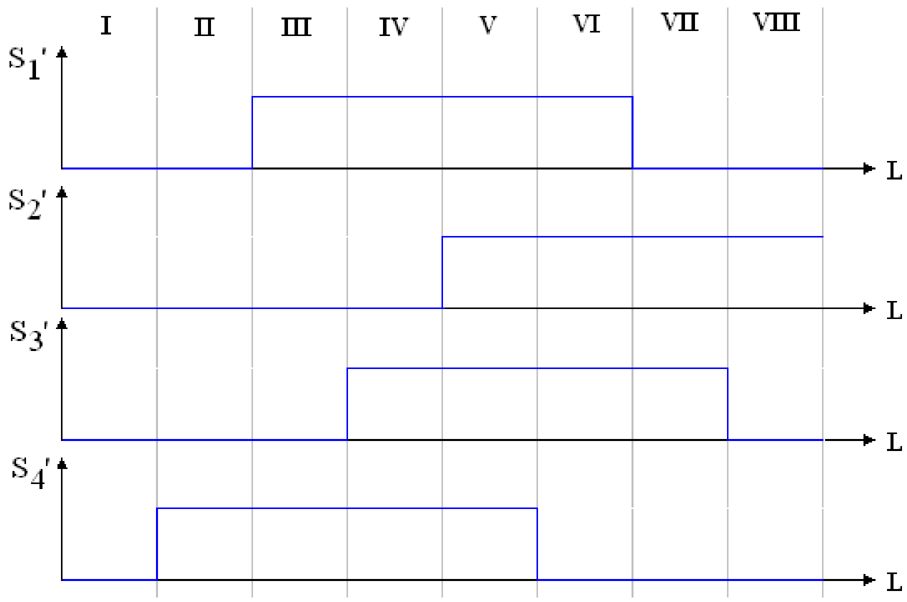

Fig.3-7 Modified signals from outputs of laser interferometric displacement sensor

Any one set of quadrature digital signals can act as sensor outputs. Since the signals outputs are in the format of incremental signals. They can be converted to displacement by a conventional decoder with a resolution of *λ/8.*

3.3.2 Further resolution enhancement

Some applications require a higher precision position measuring system and the following processing can be employed. Apart from utilizing S_1' and S_2', or S_3' and S_4', four signals can further enhance the resolution of the displacement sensor. Before the further resolution enhancement is explained, the phase relationships between S_1', S_2', S_3', and S_4' have to be investigated.

Four regenerated sensor outputs (S_1, S_2, S_3, and S_4) can be formulated by modifying (3.7). These four analog signals are represented mathematically in (3.12). Note that $KL_{coupler}$ is 30^o for 3×3 optical coupler with same coupling ratio.

$$\begin{aligned}
&S_1 : O_1'+O_2' = -\frac{2}{9}B^2(1-\cos 3KL_{coupler})\cos\phi \propto \sin(\phi-90^o) \\
&S_2 : O_1'-O_2' = -\frac{2}{3}B^2(\sin 3KL_{coupler})\sin\phi \propto \sin(\phi-180^o) \\
&S_3 : 2O_1'+O_2' = -\frac{1}{3}B^2(1-\cos 3KL_{coupler})\cos\phi - \frac{1}{3}B^2(\sin 3KL_{coupler})\sin\phi \\
&\qquad\qquad \propto \sin(\phi-135^o) \\
&S_4 : O_1'+2O_2' = -\frac{1}{3}B^2(1-\cos 3KL_{coupler})\cos\phi + \frac{1}{3}B^2(\sin 3KL_{coupler})\sin\phi \\
&\qquad\qquad \propto \sin(\phi-45^o)
\end{aligned} \tag{3.12}$$

As illustrated in (3.12), the phase differences between these four signals are 45^o. (S_2 is 45^o leading S_3, S_3 is 45^o leading S_1, S_1 is 45^o leading S_4, and S_4 is 45^o leading S_2) Based on this feature, a signal processing method for resolution enhancement is proposed, so that these four signals can generate another two incremental signals with better resolution.

Four analog signals (S_1, S_2, S_3, and S_4) can be digitized to generate four square waves (S_1', S_2', S_3', and S_4') by comparing the analog signals with zero. In order to develop the better resolution outputs, a logic circuit is proposed in this project. The truth table is designed and constructed as shown in Table 3-1. Based on the truth table, the combinational logic for Phase A and Phase B can be derived and Phase A= $S_1'\oplus S_2'$ and Phase B= $S_3'\oplus S_4'$.

Input				Output	
S_1'	S_2'	S_3'	S_4'	Phase A	Phase B
0	0	0	0	0	0
0	0	0	1	0	1
1	0	0	1	1	1
1	0	1	1	1	0
1	1	1	1	0	0
1	1	1	0	0	1
0	1	1	0	1	1
0	1	0	0	1	0

Table 3-1 Truth table for resolution improvement of interferometric displacement sensor with 3×3 fiber coupler

These two outputs of XOR gates are in quadrature and they become the incremental outputs of the proposed sensor (Phase A and Phase B). The resolution of these two new outputs can be dramatically improved to $\lambda/16$, which is eight times less than the measuring system which only uses the digital form of O_1' and O_2'. The two proposed sensor outputs are illustrated in the last two panels of Fig. 3-8.

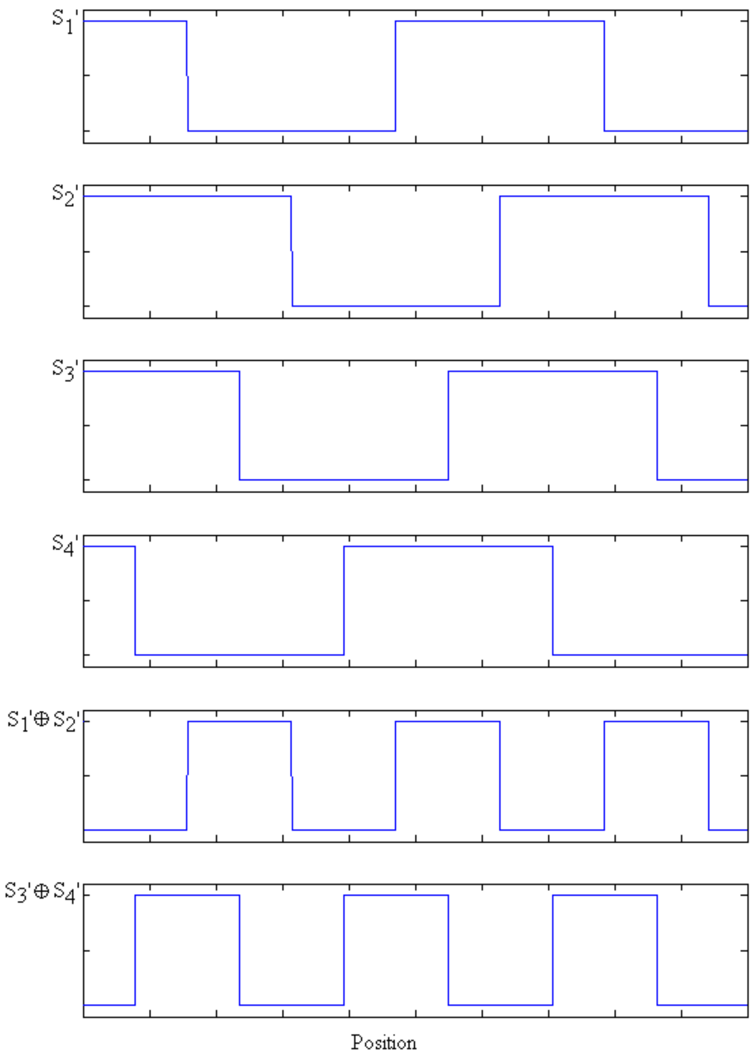

Fig.3-8 Digital signals of S_1', S_2', S_3', S_4', Phase A and Phase B

In this project, the number of conditions for comparison is 4. However, if the proposed idea is generalized, the number of conditions will be expanded to 2^n, where n is a positive integer. This design rule is based on the truth that the final outputs of the position sensor are two digital signals in quadrature. The logical and simple way for formulating these quadrature signals is therefore to use 2^n conditions.

3.4 Practical implementation for signal processing

An incremental decoder is usually embedded in an industrial motor controller and the incremental quadrature signal becomes a standard position encoder interface. In order to convert the optical signal outputs of the interferometer into favorable incremental signals, a set of analog circuits is proposed and constructed to implement the conversion method mentioned before. Note that the modification should not be handled by the digital signal processor (DSP) since the data sampling frequency in the DSP is limited. The configuration analog circuit is described as shown in Fig.3-9. The whole circuit can be classified into three different parts:

1) Signal conversion stage
2) Offset elimination stage
3) Signal amplification and resolution enhancing stage

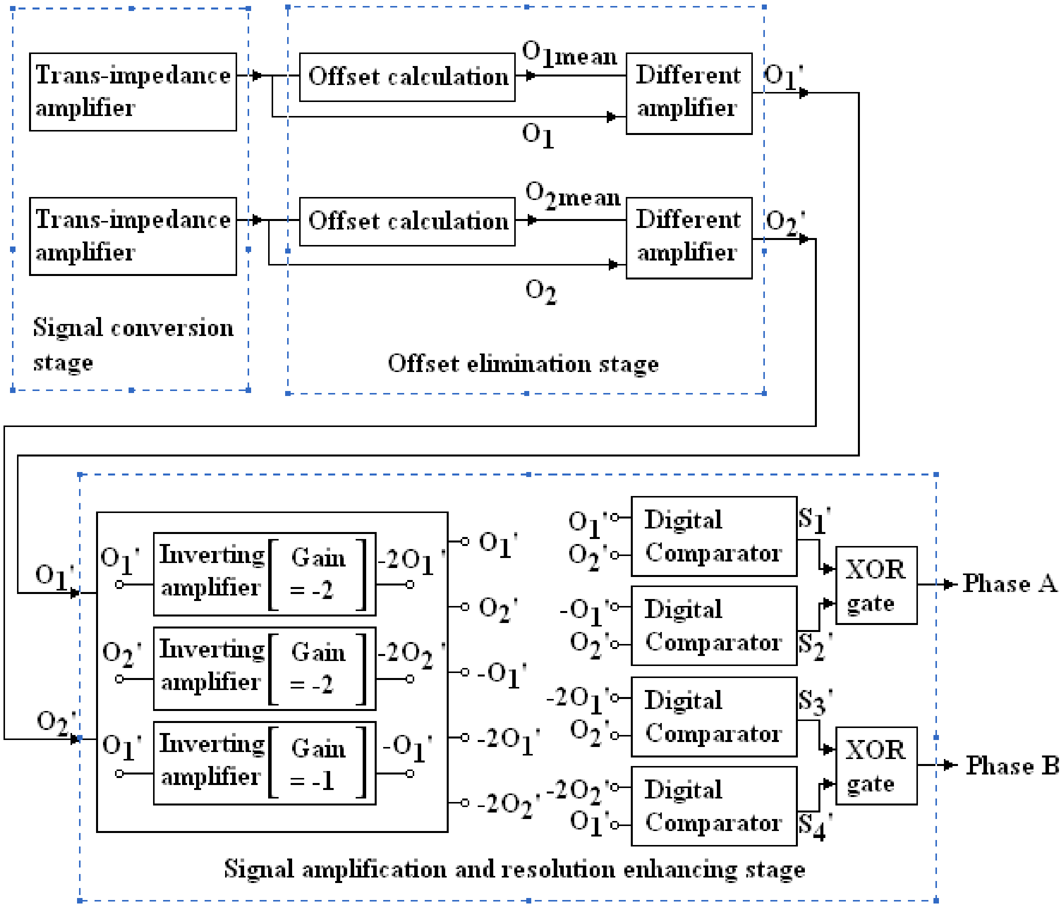

Fig.3-9 Block diagram of the proposed optical interferometric displacement sensor

3.4.1 Signal conversion

A trans-impedance amplifier is a photo-current I_f to voltage conversion circuit. Photodiode is an optical device which converts the light intensity into photo-current with ratio equal to responsivity R_e (with unit A/W). Fig.3-10 shows the circuit connection of a trans-impedance amplifier. The relationship between input and output of trans-impedance amplifier is:

$$V_o = RI_f \tag{3.13}$$

where R is the resistance of the variable resistor

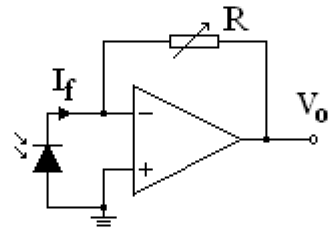

Fig.3-10 Trans-impedance amplifier

The converted voltage outputs from the interferometer are O_1 and O_2. The amplitudes of these two signals may not be identical since the bending of optical fiber in interferometer and R_e of two photodiodes are not identical. Unequal amplitudes will affect the displacement measurement and this issue can be solved by finely adjusting the variable resistors in the trans-impedance amplifier.

3.4.2 Offset elimination

The aim of this stage is to generate the offset eliminated signals (O_1' and O_2'). The mean value of O_1 and O_2 are measured by low pass filters (LPF). Since DC offsets vary with low frequency, the "offset calculation" (LPF) can be achieved by a DSP.

When the object travels at an extremely low speed, the outputs of low pass filters will be the signals instead of their mean values (O_{1mean} and O_{2mean}). In order to prevent fault operation in offset elimination, two buffers are inserted at the outputs of the LPFs. The DSP will keep storing the outputs of LPFs into the buffers. The values in the buffers will be delivered to act as measured DC values. When the movable target moves fast, the value storing and delivering will be processed continuously. If the speed of the target is very low (the frequency of O_1 and O_2 will be lower than the cutoff frequency of LPFs), the DSP will stop the value storing process. The previous stored values in buffers (recorded when the target moves fast) will be delivered.

The signals O_1 and O_2 will be subtracted by their mean values. This function is achieved by the difference amplifiers as shown in Fig.3-11. The voltage outputs of the difference amplifiers for O_1 and O_2 are shown in (3.14).

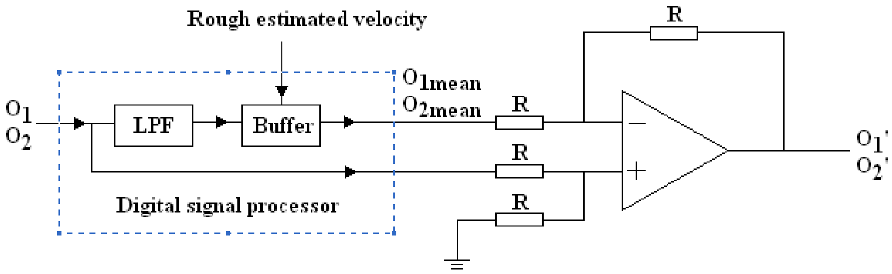

Fig.3-11 Circuit of offset elimination stage

$$\begin{aligned} O_1' &= (O_1 - O_{1mean}) \\ O_2' &= (O_2 - O_{2mean}) \end{aligned} \tag{3.14}$$

3.4.3 Signal amplification and resolution enhancement

O_1' and O_2' have to be modified so the outputs of displacement sensor can be employed by the conventional analogue incremental decoder. The signals O_1' and O_2' are amplified by inverting amplifiers. These five modified signals are then delivered to the four precise voltage comparators. The function of comparators can be summarized as shown in Table 3-2.

Output of comparator	Condition for output = 5V	Condition for output = 0V
S_1'	$O_1' > -O_2'$	$O_1' < -O_2'$
S_2'	$O_1' > O_2'$	$O_1' < O_2'$
S_3'	$2O_1' > -O_2'$	$2O_1' < -O_2'$
S_4'	$O_1' > -2O_2'$	$O_1' < -2O_2'$

Table 3-2 Function of the comparators

XOR gates are then applied to obtain the $S_1' \oplus S_2'$ and $S_3' \oplus S_4'$. These two logic gate outputs fulfill the interface requirement of incremental encoded signals (quadrature square waves) named as Phase A and Phase B. Generic interface of the incremental encoder contains four terminals ($A, B, \overline{A}, \overline{B}$) so that the line drivers (absence in Fig.3-9) are installed at the terminals of Phase A and Phase B. Hence, this laser interferometric displacement sensor with better resolution can be used in generic motor controller directly. Note that the line drivers are also responsible for providing enough current to drive the decoder circuitry.

3.5 Experimental results and discussion

3.5.1 Experimental setup

Fig.3-12 shows the experimental setup of the measuring system. This was used to verify the performance of the proposed laser interferometric displacement sensor with 3×3 fiber coupler and the proposed circuit. Several important points regarding the experiment setup should be highlighted. The moving target (mirror) was installed on a controlled voice coil motor (VCM) which was oscillated and driven by constant voltage source and H-bridge driver. VCM also belongs to the PMLM with a single coil in the translator and two poles magnets in the stator. The variable resistors in the trans-impedance amplifiers were used for small manual adjustment to compensate the difference in amplitudes of O_1 and O_2. DSP was responsible for offset detection (offset updating rate is 10Hz) and converting Phase A and Phase B to displacement by an embedded incremental decoder. In addition, the position of the VCM was also measured by a reference sensor (optical linear incremental encoder) and the outputs of sensor were also converted to position information by a decoder in the DSP. Note that all equipments, including mirror mounting apparatus and linear voice coil motor, are put on the flat table so that the external disturbance and vibration are minimized. Models and specifications of all equipments used in this experiment are shown in Table 3-3. The experimental results are shown and its details are explained.

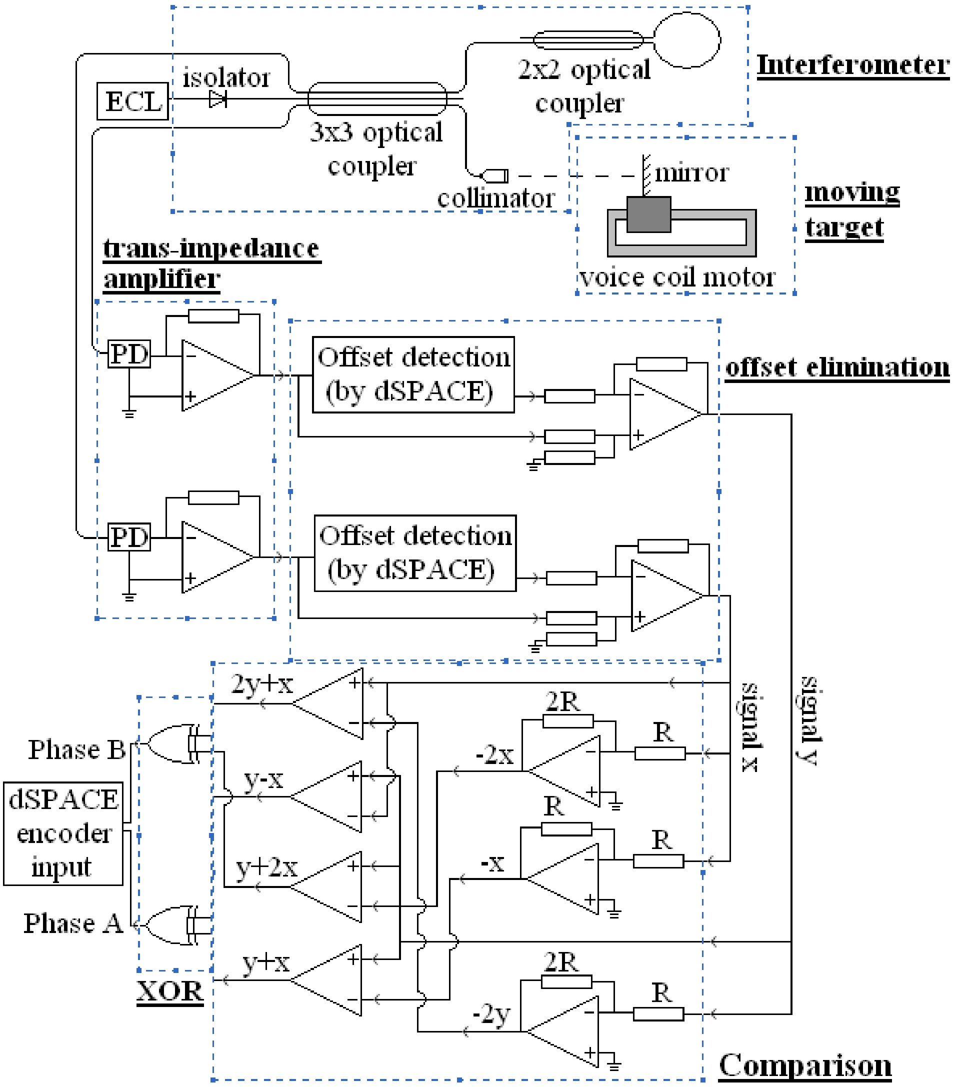

Fig.3-12 Experiential setup for proposed interferometer demonstration

Name of equipment	Company	Model	Other specification
External-cavity laser (ECL) operated at 1528nm wavelength	New Focus	6262	linewidth 5MHz at wavelength =1550nm
1550nm Single mode standard 3×3 coupler	Go4fiber	SSS-3x3-15-33/ 33/33-Q-9-1	
1550nm dual stage optical isolator	Go4fiber	GISD-P-15-9-10-00	
1550nm Standard 2x2 Coupler	Go4fiber	SSS-2x2-15-50/ 50-Q-9-1	
PCB wiring-head-machine (voice coil motor)	ASM		Max. acc = $5ms^{-2}$, max. continue current = 5A
Mirror	Newport	10D20ER.2	For wavelength between 480nm to 20μm
Mirror mounting	Newport	U100-A3K	
Collimator	Go4fibe	GPMC-15-05-B-G-M-C-10-FC	1mm lens diameter, with FC/PC connector
InGaAs PIN Photodiode	Go4fiber	GT322D-A-FC	
Digital Signal Processor Board	dSPACE	DS1104 R&D controller board	
Operational amplifiers	Analog Device	OP37	
Comparators	National semiconductor	LM339	
XOR gates	Texas Instruments	SN74ACT86N	
Linear optical incremental encoder	Renishaw	RGH24H30D30A	Resolution of 50nm

Table 3-3 Models and specifications of equipments for the interferometric displacement sensor with 3×3 fiber coupler

During the experiment, the VCM is driven to oscillation with a frequency of 10Hz. The position information from the proposed method and decoded position from the optical linear incremental encoder are recorded, the velocity of the movable target is calculated by differentiating the position from the output of the reference sensor. The acceleration is further calculated by differentiating the velocity of the movable target. The experimental results are shown in Fig.3-13. The displacement measured by both the proposed sensor and the reference sensor are recorded and the results are shown in the Fig.3-13(a). Note that the position-time graph actually contains two curves and the difference between them is too small to be observed. The difference (error) between two curves is shown in the bottom panels. Magnified plots between 0.2s to 0.4s are shown in Fig.3-14. This figure can help to explain the phenomenon during the operation of the sensor.

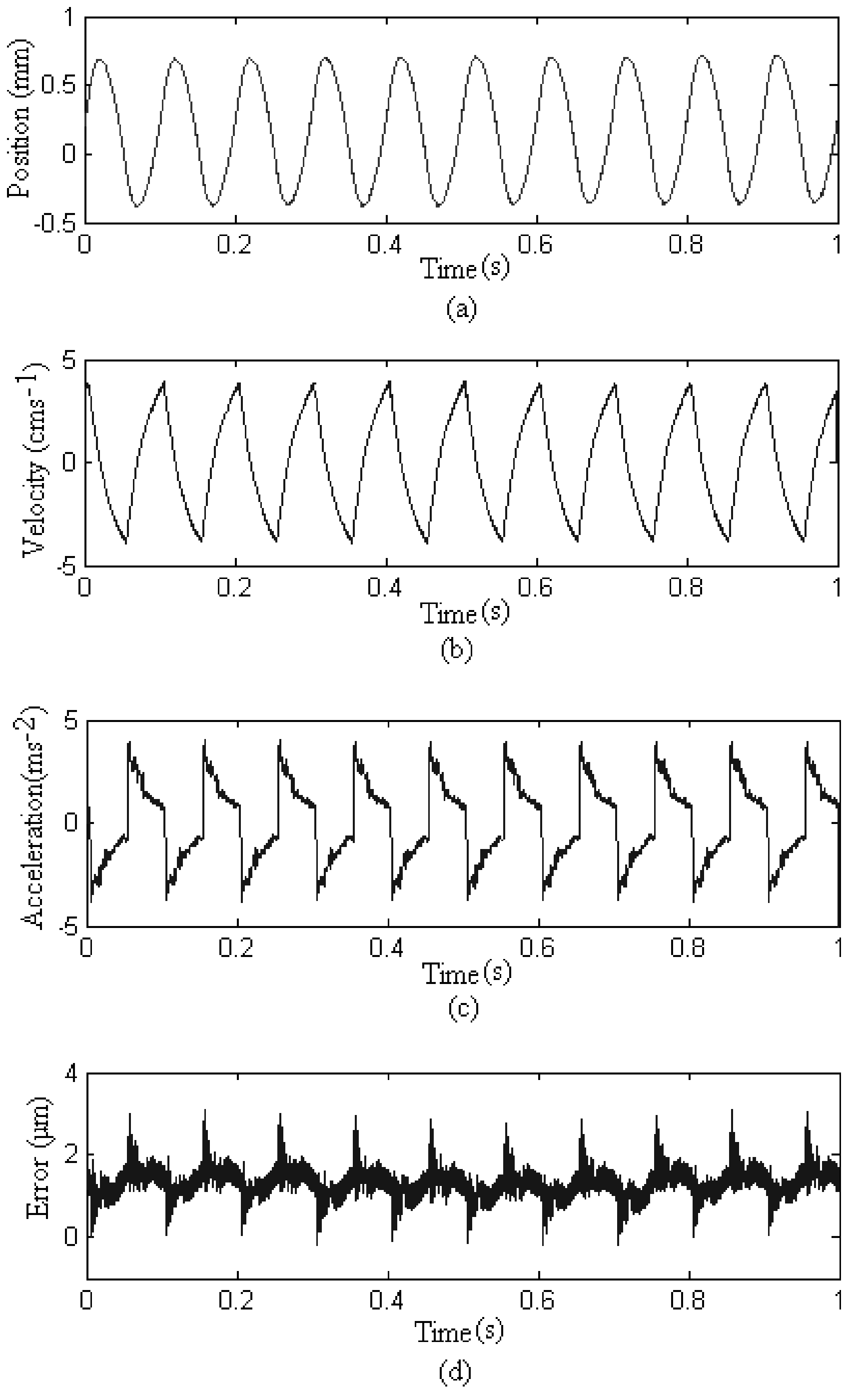

Fig.3-13 Experimental results of the proposed sensor with VCM; (a) position time graph with measurements from proposed method and incremental encoder; (b) velocity time graph from the measurement of the incremental encoder; (c) acceleration time graph from the measurement of the incremental encoder; (d) position difference between the measurements from the proposed method and the incremental encoder

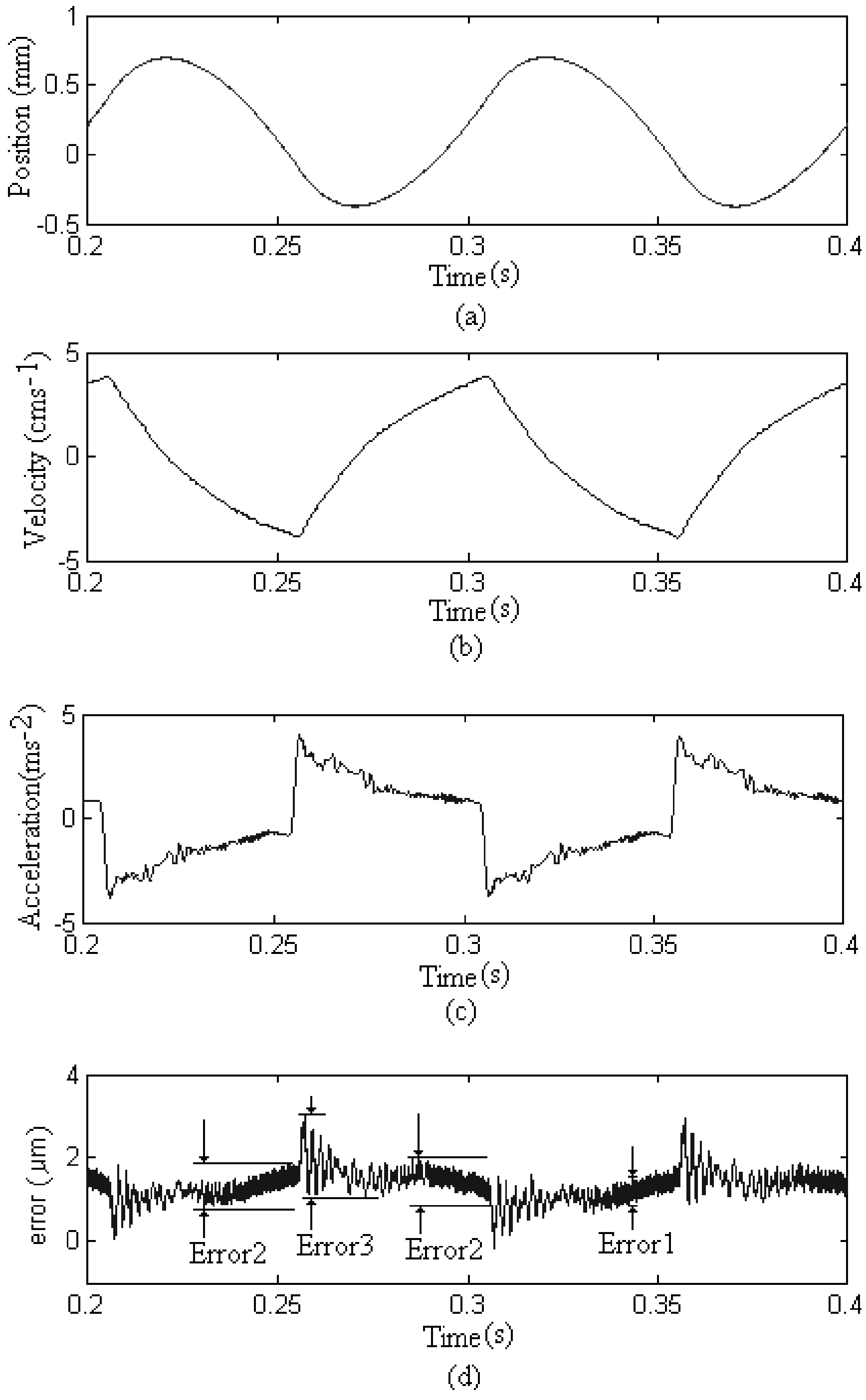

Fig.3-14 Magnified results of the proposed sensor (between 0.2s and 0.4s); (a) position time graph with measurements from proposed method and incremental encoder; (b) velocity time graph from the measurement of the incremental encoder; (c) acceleration time graph from the measurement of the incremental encoder; (d) position difference between the measurements from the proposed method and the incremental encoder

If the position measurements of proposed sensor and reference sensor are compared, the laser interferometric displacement sensor tracks the actual position and provides the correct position measurement. When the magnified error curve is investigated further, three types of errors can be observed. “Error 1” is caused by unequal amplitude and non-zero offset in O_1’ and O_2’. “Error 2” and “Error 3” result from the acceleration of actuator and the elastic properties of the mirror mounting installed on the movable target.

3.5.2 Discussion on resolution error (Error 1)

Considering the Lissajous figure of O_1’ and O_2’, the shape of the slanting ellipse may be irregular as shown in Fig.3-15 and Fig.3-16. Two reasons can cause these two irregular ellipses, which are unequal amplitudes and residue offsets in O_1’ and O_2’.

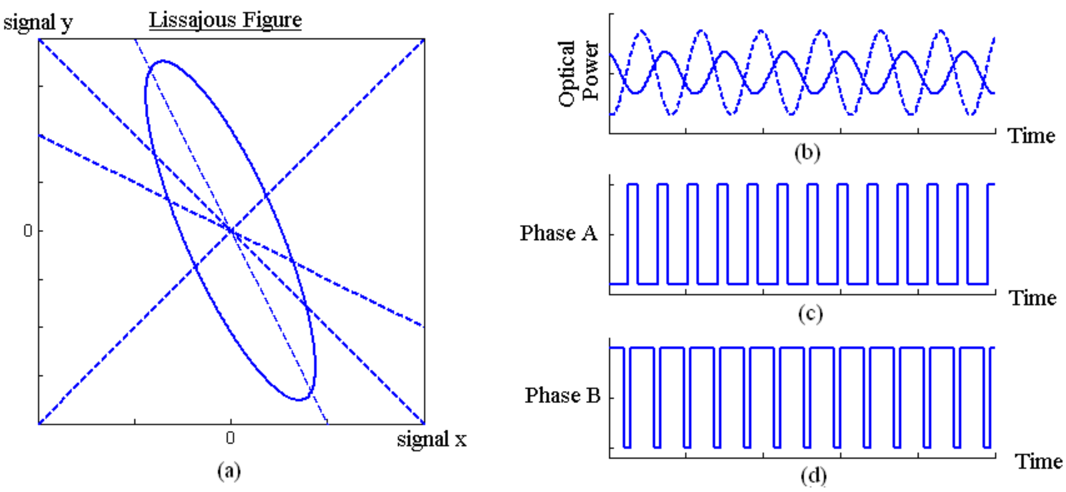

Fig.3-15 Waveforms of proposed sensor outputs when the offset of signals are not zero; (a) Lissajous figure; (b) Optical outputs of the proposed sensor; (c) Phase A output of the proposed sensor; (d) Phase B output of the proposed sensor

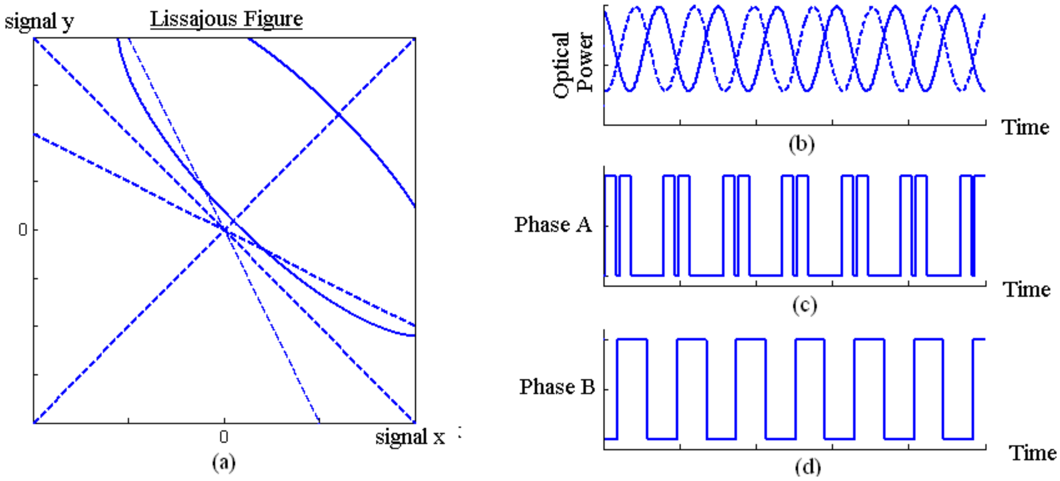

Fig.3-16 Waveforms of proposed sensor outputs when the amplitudes of the signals are difference; (a) Lissajous figure; (b) Optical outputs of the proposed sensor; (c) Phase A output of the proposed sensor; (d) Phase B output of the proposed sensor

Although variable resistors are embedded in trans-impedance amplifiers for fine adjustment of amplitudes, there are still some fluctuations in their amplitudes. This can be influenced by the non-linearity of the 3×3 coupler [20]. It can also be caused by a slight difference in the photodiodes.

The DC values of O_1 and O_2 are calculated by DSP which outputs are updated at 10Hz. Discrete calculated outputs may not reflect the actual DC values of O_1 and O_2. As a result, O_1' and O_2' are not completely compensated and residual offsets appear. These residue offsets also cause irregular ellipse in Lissajous figure. Note that the case illustrated in Fig.3-16 is the extreme case. In this case, the outputs of the proposed sensor are deformed and cannot perform as incremental signals. In practical case, the offset elimination stage will prevent large offsets appearing. The residual offset of O_1' and O_2' are expected to be small so that the incremental outputs will not be distorted.

As shown in Fig. 3-15 and Fig. 3-16, once the shape of the slanting ellipse is distorted, the shapes of incremental encoded signals (quadrature pulses Phase A and Phase B) are no longer regular. In this project, the effect of unequal amplitude has already been minimized by adjusting a variable resistor within the trans-impedance amplifier so that the difference between amplitudes of two signals from the interferometer outputs can be reduced. The offset detection and elimination circuits shown in Fig.3-11 aim to reduce the non-zero signal offset effect. Unfortunately, small residue offsets may still exist. If the offsets are not as serious as shown in Fig.3-16 such that the ellipse can still cross four lines, this performance may still be regarded as acceptable and the measurement errors are bounded to $\lambda/4$.

To conclude, the above mentioned distortion can not be completely eliminated. The maximum deviation between the actual position and sensor measurement can be limited to $\lambda/4$. This maximum deviation is approximately equal to the deviation in "Error 1".

3.5.3 Discussion on mirror displacement error (Error 2)

The photograph of experiment setup shown in Fig.3-17 has to be studied. The mirror is installed on the mirror holder and the mirror mount. The mirror mount includes three screws and two stiff springs to support the mirror holder and adjust the angle of mirror. The round mirror is fixed on the mirror holder by a rubber screw which provides horizontal pressure to fix the position of the mirror.

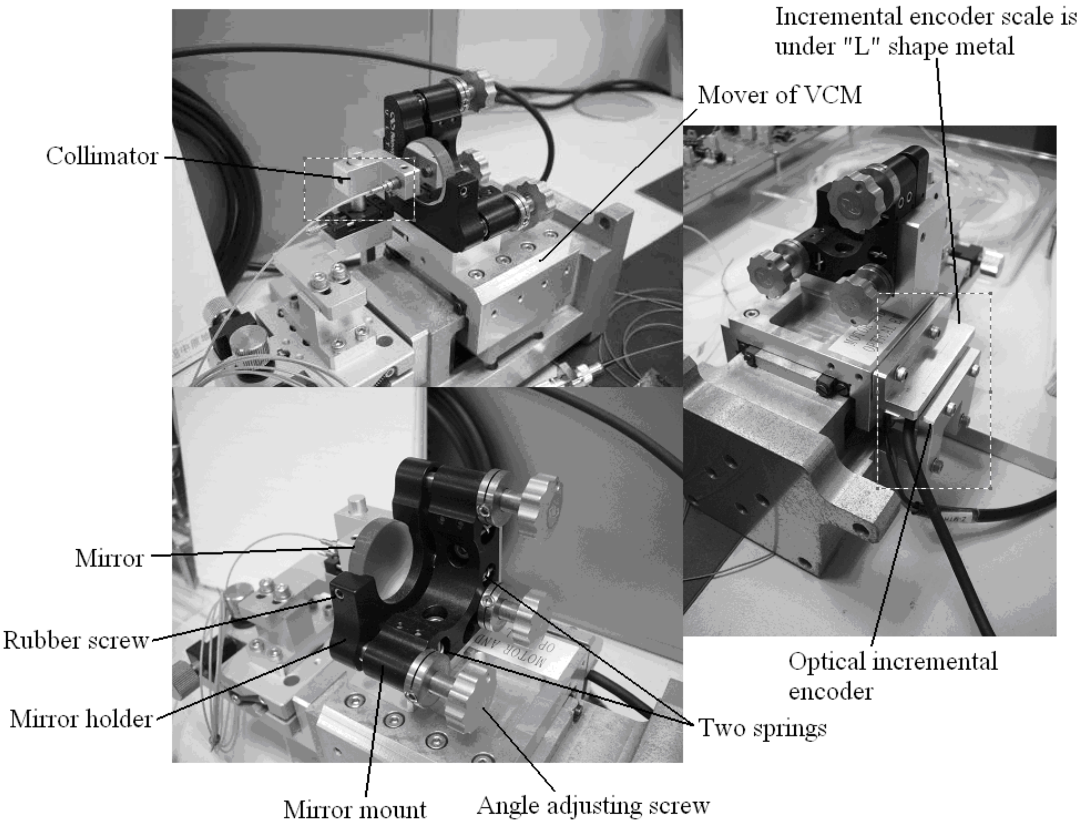

Fig.3-17 Snapshot of the experimental setup (collimator, mirror and mirror)

When the motor is accelerated, a torque is applied to the base of the mirror mount so mirror holder will be tilted with a small angle due to the springs and inertia of the mirror holder. In addition, the rubber screw can further reinforce the tilting effect. This tilted angle increases with the motor acceleration. When the mirror is tilted, its position of mirror will drift forward or backward slightly. The relationship between the acceleration and titled angle can also be observed in Fig.3-13 and Fig.3-14. Actually, the proposed sensor is measuring the position of the mirror and the reference sensor is measuring the position of the VCM translator. The mirror mount is relatively elastic and the mounting of encoder is rigid, so “Error 2” is produced.

This error is caused by the elastic properties and mechanical design of mirror holder and mirror mount. Re-designing the mirror holder can improve the performance of the sensor and the effect of “Error 2” can be reduced.

3.5.4 Discussion on mirror oscillation (Error 3)

This kind of error always appeared after a sudden change in acceleration (i.e. the motor is reversing the moving direction). It is caused by the step-like force exerted on the mirror mounting and this force causes oscillation in the spring of mirror mount and mirror.

In order to verify the suggested explanation, another experiment was conducted. The VCM was driven by a smooth acceleration profile so that the step-like force disappeared throughout the experiment. The experimental results are shown in Fig.3-18. When there is an absence of step-like force, “Error 3” is completely absent. It proves that the “Error 3” is caused by a sudden change in acceleration of the movable target.

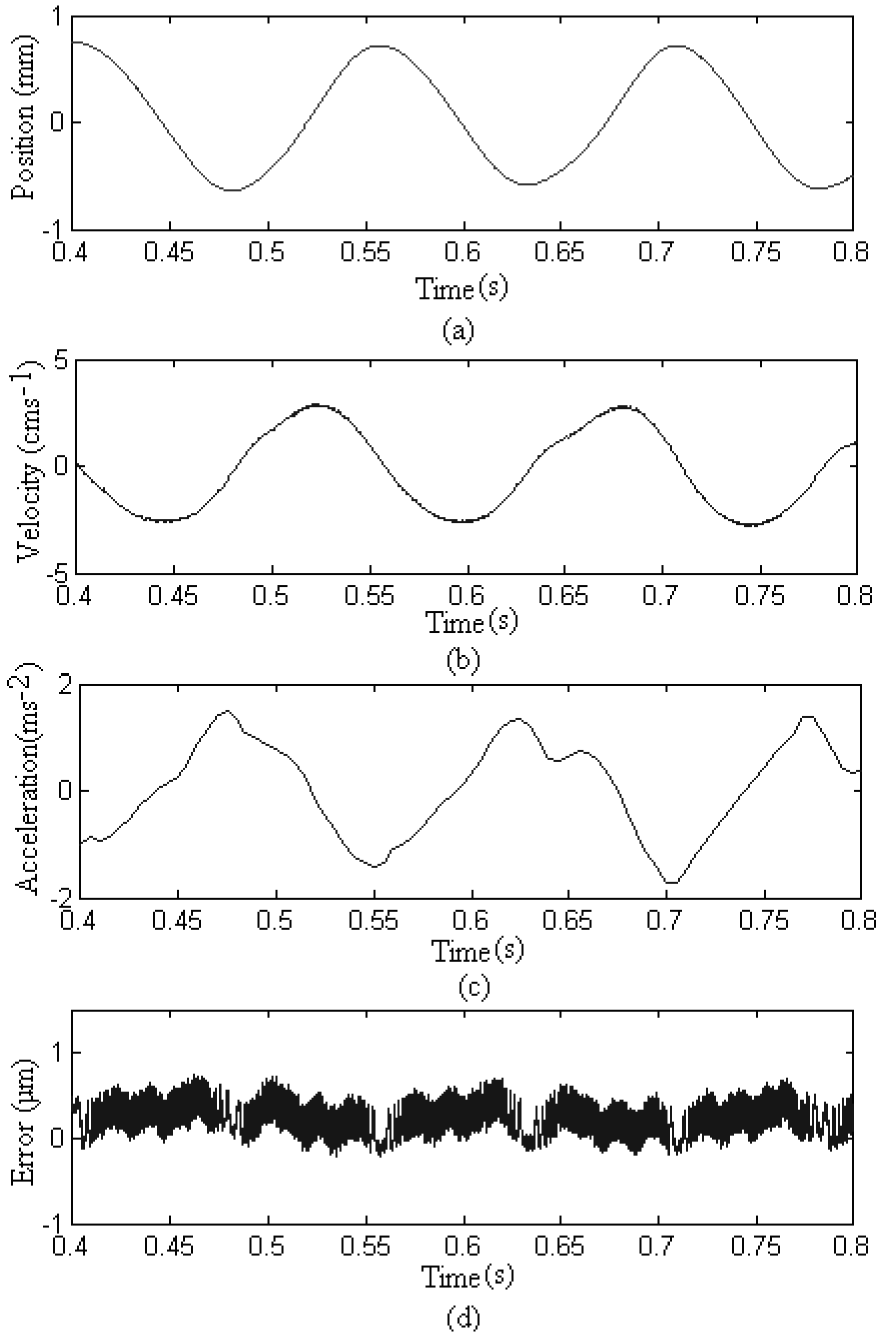

Fig.3-18. Experimental result of the proposed sensor under small acceleration; (a) position time graph with measurements from the proposed method and the incremental encoder; (b) velocity time graph from the measurement of the incremental encoder; (c) acceleration time graph from the measurement of the incremental encoder; (d) position difference between the measurements from the proposed method and the incremental encoder

3.5.5 Discussion on the measurement speed, the repeatability and the resolution of the sensor

The maximum measurement speed of the incremental encoder is determined by the frequency bandwidth modification circuitry mentioned in section 3.2.4. In the demonstration prototype, the 3dB cutoff frequency of the whole circuitry is about 150 kHz. This means that the measurement speed can be as high as $\lambda * 150k/4 = 37500\lambda s^{-1}$.

The repeatability of this proposed sensor is affected by the speed of the measured target, the operation of the offset elimination circuit, and the wavelength of the laser source. Some precautions have been carried out to ensure the repeatability.

1) The wavelength of the laser source is stabilized with line width 5MHz at λ=1550nm. The corresponding wavelength deviation is 0.04pm, which is a very small value compared with the resolution.
2) The updating rate of the buffer in offset elimination circuit is limited by the sampling frequency of the DSP. The rate of change of the measured offset should not be too high so that the buffers can deliver the correct offset values.
3) The maximum measurable speed of the sensor is governed by the frequency bandwidth of the electronic circuit. The measured target should be moved within the limitation.

Regarding the resolution of the sensor, the laser light injected to the optical system is 1528nm monochromic laser and hence the resolution is equal to 1528nm/16 = 95.5nm.

3.6 Summary

A low cost and high precision incremental encoder sensor constructed by the 3×3 fiber coupler and the resolution modification circuit is described. The displacement measurement is based on two converted square waves from outputs of the interferometer. The resolution of the sensor can be up to 95.5nm with a maximum measurement speed of $10cms^{-1}$.

The most expensive component in this sensing system is the ECL light source and it can be replaced by the inexpensive light source mentioned in [21] and [22] (DFB laser locked to a gas absorption line). The frequency of the DFB laser can be stabilized with r.m.s. deviation equal to or smaller than 50MHz, which is about 0.4pm in terms of wavelength variation. Compared with ECL, frequency deviation of DFB laser with locking is larger. The trade-off of this replacement is shorter coherence length and shorter measurement range.

In this proposed sensor, the IC in the modification circuit is designed for general purpose. The measurement speed of sensor can be further improved by other ICs with high frequency bandwidth. In addition, the precision of this sensing system can be further improved by a shorter wavelength laser. The proposed method is especially suitable for high precision oscillation displacement measurement, such as the sensor in feedback control of a high precision mechatronic system.

Chapter 4
Background studies on the limitations of incremental encoder enhancement and the data fusion algorithm

4.1 Limitation of the optical linear incremental encoder

The most popular linear motion sensor used in high precision linear motion system is the optical linear incremental encoder but this high precision sensor usually limited by a common problem described in this section.

As mentioned in Section 2.2, a quadrature decoder samples the output Phase A and Phase B in order to obtain the position from the incremental encoder. Based on the past and present binary state of these two phases, the decoder delivers the “count signal” and the “direction signal” in order to calculate the position of the movable target. Note that an external high frequency clock is necessary for the quadrature decoder. This clock frequency has to be at least six times higher than the frequency of Phase A and Phase B. A high frequency clock will ensure that there is at least one clock period appearing within one state. If the noise in signals Phase A and Phase B are serious, the frequency of these two signals has to be further reduced.

Some companies, such as Renishaw, suggest that the minimum clock frequency has to be [7]:

$$clock\ \ frequency = \frac{encoder\ \ velocity}{resolution} \times 4 \tag{4.1}$$

The constant "four" shown in (4.1) is a safe factor in order to guarantee that the asynchronous inputs are stable and the effect of noise is eliminated. The limitation of clock frequency definitely affects the maximum measurement velocity of encoder as shown in (4.2).

$$\max imum\ \ measurement\ \ velocity = \frac{clock\ \ frequency\ \ \times resolution}{4} \tag{4.2}$$

Industrial applications usually request a fast and high precision motion control system. This speed limitation is definitely an important issue to be considered during high precision motion control. In this project, the outputs of incremental encoder are enhanced so as to overcome the limitation and enlarge the measurement speed.

4.2 Data fusion algorithm

[28] shows a proved fusion algorithm. In order to join the data together, two statistics parameters (mean μ and variance σ^2) of the measured data have to be obtained. If traditional algorithms shown in (4.3) are used, a lot of memories have to be utilized in order to store measured data. The number of storage devices can be greatly reduced and (4.3) can be reformulated as shown in (4.4). Note that (4.3) calculates the mean and variance by n stored data but (4.4) uses previous calculated values and new measured data only.

$$\begin{cases} \mu_n = \frac{1}{n}\sum_{i=1}^{n} x_i \\ \sigma_n^{\ 2} = \frac{1}{n}\sum_{i=1}^{n} (x_i - \mu_n)^2 \end{cases} \tag{4.3}$$

$$\begin{cases} \mu_{n+1} = \frac{1}{n+1}\sum_{i=1}^{n+1} x_i = \mu_n + \frac{1}{n+1}(x_{n+1} - \mu_n) \\ \sigma_{n+1}^{\ 2} = \frac{1}{n+1}\sum_{i=1}^{n+1} (x_i - \mu_{n+1})^2 = (1 - \frac{1}{n+1})[\sigma_n^{\ 2} + \frac{1}{n+1}(x_{n+1} - \mu_n)^2] \end{cases} \tag{4.4}$$

At time n+1, once the new measured data x_{n+1} are obtained, previous calculated mean μ_n and variance σ_n^2 are utilized for calculating updated mean μ_{n+1} and variance σ_{n+1}^2 by (4.4).

Assume the target is moved at a velocity $\dot{x}$, there are two velocity measurements from two motion sensors (v_1 and v_2). These two measurements can be approximated by a normal probability density function with means ($v_{1\mu}$ and $v_{2\mu}$) and variances (σ_1^2 and σ_2^2). It is expected that the means ($v_{1\mu}$ and $v_{2\mu}$) are equal to the current measurement of sensors (v_1 and v_2). The probability of the first sensor which can measure the actual velocity is:

$$p_1(v) = \frac{1}{\sqrt{2\pi\sigma_1^{\ 2}}} e^{-[(\dot{x} - v_{1\mu})^2 / 2\sigma_1^{\ 2}]} \tag{4.5}$$

The probability of the second sensor which can measure the actual velocity is:

$$p_2(v) = \frac{1}{\sqrt{2\pi\sigma_2^{\ 2}}} e^{-[(\dot{x} - v_{2\mu})^2 / 2\sigma_2^{\ 2}]} \tag{4.6}$$

The probability that both sensors can measure actual velocity at the same time is

$$p_1(v)p_2(v) = \frac{1}{\sqrt{2\pi\sigma_1^2\sigma_2^2}} e^{-[(\dot{x}-v_{1\mu})^2/2\sigma_1^2]-[(\dot{x}-v_{2\mu})^2/2\sigma_2^2]} \\ = Ge^{-\frac{1}{2}(\frac{\sigma_1^2+\sigma_2^2}{\sigma_1^2\sigma_2^2})(\dot{x}-\frac{v_{1\mu}\sigma_2^2+v_{2\mu}\sigma_1^2}{\sigma_1^2+\sigma_2^2})^2} \qquad (4.7)$$

where G is a constant with complex expression.

Note that the mean of the probability density function is $\frac{v_1\sigma_2^2+v_2\sigma_1^2}{\sigma_1^2+\sigma_2^2}$ and the variance of the probability density function is $\frac{\sigma_1^2\sigma_2^2}{\sigma_1^2+\sigma_2^2}$. Since another interpretation of mean is the expectation of the measured data, the mean of this probability density function can be used for combining information from the two sensors as shown in (4.8).

$$v_{fused} = \frac{v_1\sigma_2^2 + v_2\sigma_1^2}{\sigma_1^2+\sigma_2^2} \qquad (4.8)$$

where v_{fused} is the fused velocity

v_1 is the measured velocity of the first sensor

v_2 is the measured velocity of the second sensor

σ_1 is the standard deviation velocity of the first sensor

σ_2 is the standard deviation velocity of the second sensor

This combined information will be more accurate since the variance $\frac{\sigma_1^2\sigma_2^2}{\sigma_1^2+\sigma_2^2}$ is smaller than σ_1^2 and σ_2^2.

In this thesis, the presented data fusion algorithm is further extended to develop a novel enhancement for the outputs of linear incremental encoder, which aims to improve the maximum measurement speed of the motion sensing system.

Chapter 5
Enhancement approaches to improve the performance of incremental encoders

High measurement speed and high accuracy can not appear at the same time in the incremental encoder since the maximum measurement speed is inversely proportional to the resolution of the sensor. The maximum measurement speed of a linear incremental encoder is also limited by the maximum clock frequency of decoder circuitry. In this chapter, a sensing system which provides high measurement speed and high accuracy is proposed. The new proposed method uses information from two separate sensors to generate the position measurement. These two sensors have very different properties.

(i) The first sensor has a wider measurement speed range but a lower accuracy

(ii) The second sensor has a limited measurement speed range and higher accuracy.

The proposed method combines the advantage of these two sensors (i.e. high accuracy and wide speed range) to obtain the fused position output.

The high precision sensor is an optical linear incremental encoder with a resolution down to 50nm. The outputs of this high precision sensor are modified by a dedicated circuit called “resolution increasing circuit”. This circuit can enlarge the measurement speed range of the original incremental signals and step up the resolution from 50nm to 100nm. The circuit outputs and the original incremental signals are combined to generate the fused motion information which has a higher accuracy and a wider measurement speed range.

5.1 The operation of the novel resolution increasing circuit

When the linear incremental encoder is utilized for feedback of motion control, high frequency outputs (Phase A and Phase B) are generated. The frequency of Phase A and Phase B is proportional to the velocity of the movable target. The information from the incremental encoder requires a decoder circuitry for the position information conversion. However, this decoder circuitry usually has a fixed and limited frequency bandwidth. Therefore, the frequency of Phase A and Phase B cannot be too high (i.e. the measurement speed is bounded).

In order to handle the frequency limitation problem, two approaches can be considered. The first approach is to develop a new decoding circuitry so that the frequency bandwidth of the decoder can be improved. This method requires complex and costly integrated circuit development. Another approach is to modify the outputs of the encoder so that the resolution of the sensing system is increased and frequency of Phase A and Phase B is reduced. However, the accuracy of the sensing system will be deteriorated.

In this chapter, the second method is investigated. A resolution increasing circuit is designed and constructed in order to modify the outputs of incremental encoder. The circuit diagram is shown in Fig.5-1. This circuitry can be divided into three sections: the direction detection unit, the resolution step-up unit, and the combining unit.

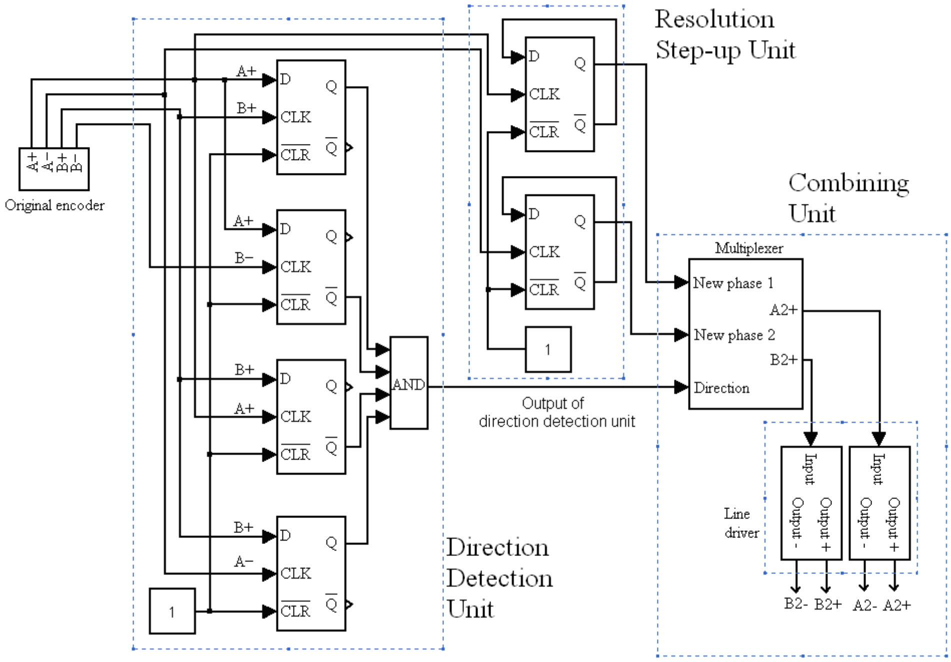

Fig.5-1 Resolution increasing circuit

5.1.1 Direction detection unit

The approach used in direction detection unit is different from that of a conventional incremental decoder. The generic detection method detects the state sequence from Phase A and Phase B. Generally, this state determination must utilize a high frequency clock signal and a high frequency circuitry. Instead of the state detection method, this project presents a simplified detection circuit which is an asynchronous circuit and uses the edge of Phase A and Phase B for direction checking. The edge detecting method is illustrated in Fig.5-2.

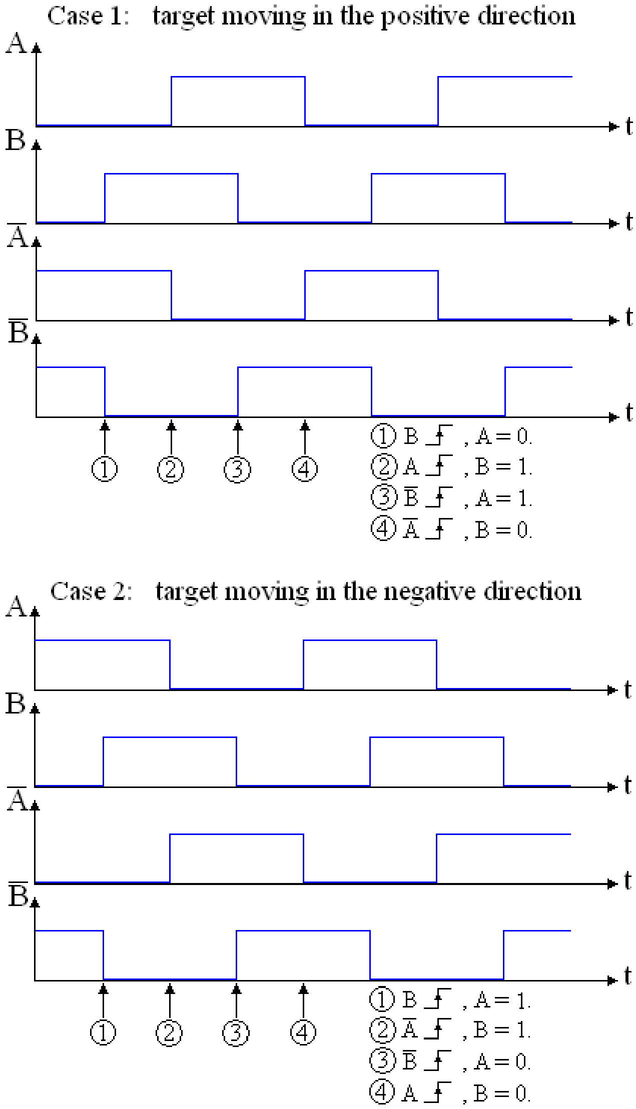

Fig.5-2 Simplified direction detection method

Consider case 1, when the movable target is moved in the positive direction, one of four triggering conditions will appear.

1) when Phase B is rising edge, Phase A is low
2) when Phase A is rising edge, Phase B is high
3) when Phase not-B is rising edge, Phase A is high
4) when Phase not-A is rising edge, Phase B is low

Similarly, in case 2, another four situations will be appeared when movable target moves in negative direction. Triggering situations are:

1) when Phase B is rising edge, Phase A is high
2) when Phase not-A is rising edge, Phase B is high
3) when Phase not-B is rising edge, Phase A is low
4) when Phase A is rising edge, Phase B is low

Obviously, the situations for positive and negative direction are complementary. The traveling direction can be determined when any one of the eight stages is detected. The observed characteristic is applied to direction detection unit. Four D-type flip flops and four-inputs-AND gate are connected to determine the direction of movable target. Each flip flop is responsible for one triggering situation and their connections of the flip flops are shown in Fig.5-1. The output of the direction detection unit will deliver logic “1” when the movable target is traveling in the positive direction and logic “0” when it is traveling in the negative direction.

5.1.2 Resolution step-up unit

The resolution step-up unit is responsible for doubling the resolution of the sensor and halves the frequency of the outputs of the encoder. Since the frequency of the encoder outputs is reduced, the maximum measurement speed of the sensing system can be doubled. This resolution step-up function is achieved by two frequency reducers which are constructed by D-type flip-flops [24]. The relationships between the encoder outputs and resolution step-up circuit outputs are shown in Fig.5-3. The top panel illustrates the actual position of the movable target. The incremental encoder will generate two signals Phase A and Phase B as shown in second and third panels. If these two signals are inputted to the resolution step-up unit, two new signals (New phase 1 and New phase 2) can be obtained and shown in last two panels of Fig.5-3.

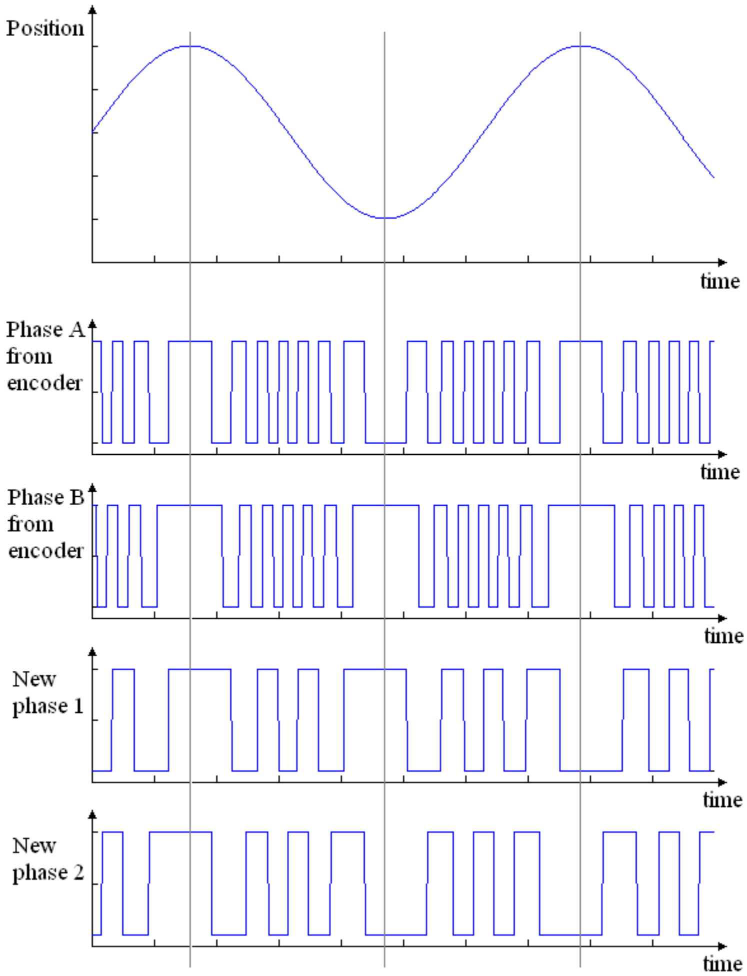

Fig.5-3 Inputs and outputs of resolution step-up unit

In this unit, the clock input of D-type flip-flop responds to a rising edge only. Phase A and Phase not-A are inputted to the upper and lower flip-flop respectively (as shown in Fig.5-1). In other words, the upper flip-flop responds to the rising edge of Phase A and the lower flip-flop responds to the falling edge of Phase A. The outputs of these two flip-flops also produce quadrature digital signals.

Although the new outputs (New phase 1 and New phase 2) are reduced in frequency and increased in resolution step-up signals, they do not contain the direction information since only one phase from the encoder (Phase A) is used. Even though the moving direction of movable target is reversed, the phase relationship between New phase 1 and New phase 2 are still maintained. Therefore, this signal can not reflect the actual moving direction of the target.

5.1.3 Combining unit

The outputs of the direction detection unit and the resolution step-up unit are inputted to the combining unit to generate displacement information. This combining function is accomplished by a multiplexer. It swaps the phases (New phase 1 and New phase 2) when the moving direction of the target is changed. New phase 1 and New phase 2 will be delivered at terminals Phase A2 and Phase B2 respectively when a positive direction is detected. If a negative direction is detected, the outputs of multiplexer will deliver New phase 2 to Phase A2 and New phase 1 to Phase B2. This process is illustrated in Fig.5-4. The first three graphs (the position-time graph, the Phase A and Phase B-time graph, the New phase 1 and New phase 2-time graph) are repeated from Fig.5-3 for comparison. The last panel simulates the outputs of resolution step up circuit. In addition, two line drivers are installed at the terminals of Phase A2 and Phase B2. They are used for generating Phase not-A2 and Phase not-B2 so that four signals are developed to fulfill the interface requirement of incremental decoder.

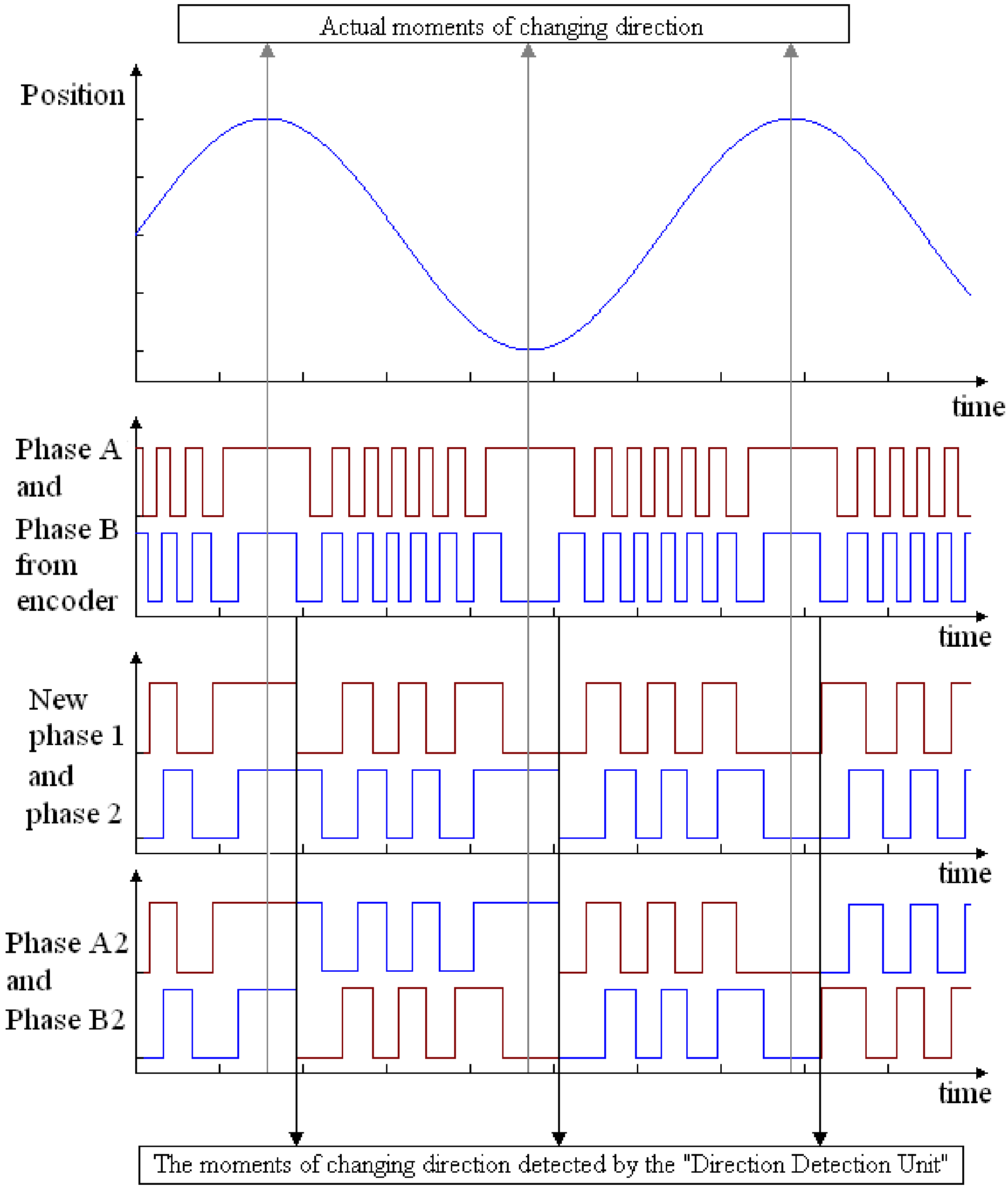

Fig.5-4 Inputs and outputs of resolution increasing circuit

5.2 Experimental investigation of outputs of the resolution increasing circuit

In order to verify the proposed idea, the resolution increasing circuit shown in Fig.5-1 was constructed. The linear optical incremental encoder was installed on the PMLM which was commanded to travel at different velocities. The output signals of the linear optical incremental encoder were connected to the decoder of the DSP and the inputs of the resolution step-up circuit. The outputs of resolution step-up circuit were also connected to the decoder of DSP.

Name of equipment	**Company**	**Model**
Permanent magnet linear motor with the Hall Effect motion sensor (PMLM)	Copley Control Corporation	SM1104
Servo driver	Copley Control Corporation	ADP-090-09-S
Digital Signal Processor Board	dSPACE	DS1104 R&D controller board
Linear optical incremental encoder (with resolution of 50nm)	Renishaw	RGH24H30D30A
AND gates	Texas Instruments	SN74HC21N
D type flip flop	Texas Instruments	SN74F74N
Multiplexer	Texas Instruments	SN54HC153
Line driver	Texas Instruments	SN75ALS192NE4

Table 5-1 Specifications and model of experiment equipments for the resolution increasing circuit and the data fusion method

During this experiment, the following valid assumptions and setup processes were carried out and they are designed to demonstrate the practical situation.

1) The maximum clock frequency for incremental decoder is assumed to be 14MHz. This assumption is referred to the actual specification of industrial decoder, such as HCTL-2000. The incremental encoder provides resolution of 50nm. In other words, the combination of the industrial decoder and the linear optical incremental encoder can provide the maximum measurement velocity equal to $0.175ms^{-1}$. Note that the maximum measurement velocity is calculated by (4.2).

2) The decoders (embedded in DSP) used in this experiment have higher clock frequency. If this decoder and the optical linear incremental encoder are used together, they will become a measurement system with a maximum measurement velocity equal to $0.33ms^{-1}$. In order to demonstrate the operation of an industrial decoder (with 14MHz clock frequency), an “artificial distortion” is added to the output of the decoder. This artificial distortion will distort the measured velocity and output to zero if the actual velocity is faster than $0.175ms^{-1}$.

For convenience of explanation, the distorted velocity output from the “artificial distortion” is named as “velocity from the incremental encoder” and the original velocity output from the optical linear incremental encoder is named as “reference velocity”. In fact, “reference velocity” and the corresponding “reference position” are provided by the most accurate sensor in the whole system.

5.2.1 Operation of the resolution increasing circuit

To illustrate the properties of the resolution increasing circuit, the experimental set up shown in Fig. 5-5 was devised. When the motor traveled at different velocities, the variances of two measured velocities (the velocity from the resolution increasing circuit and the velocity from the optical linear incremental encoder) were calculated. The variance-velocity plots of the linear optical incremental encoder and the resolution increasing circuit were obtained as shown in Fig.5-6.

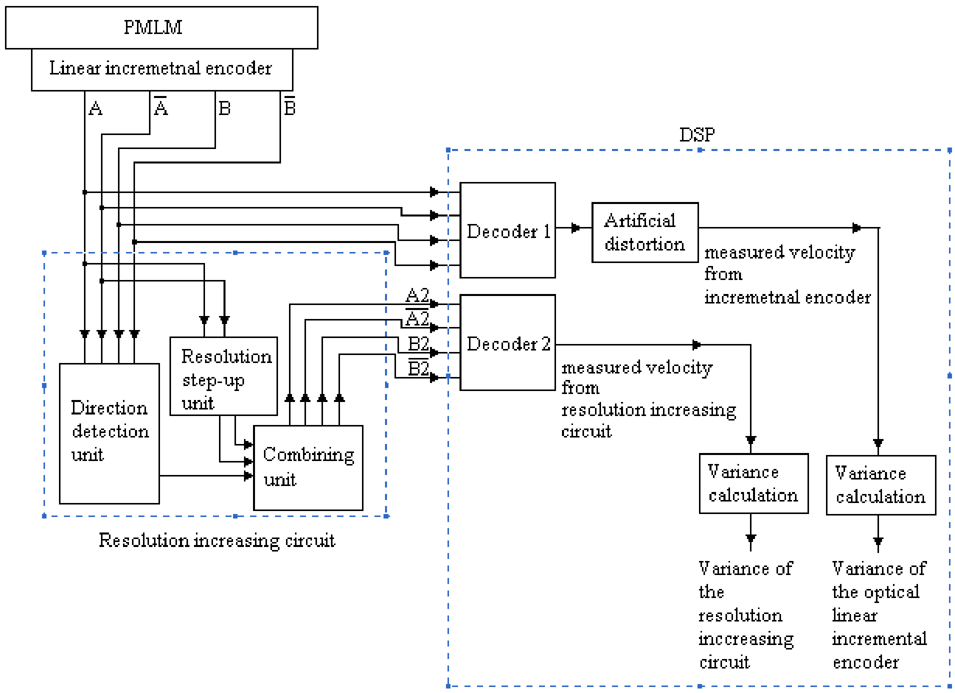

Fig.5-5 Experimental setup for testing the variance the resolution increasing circuit

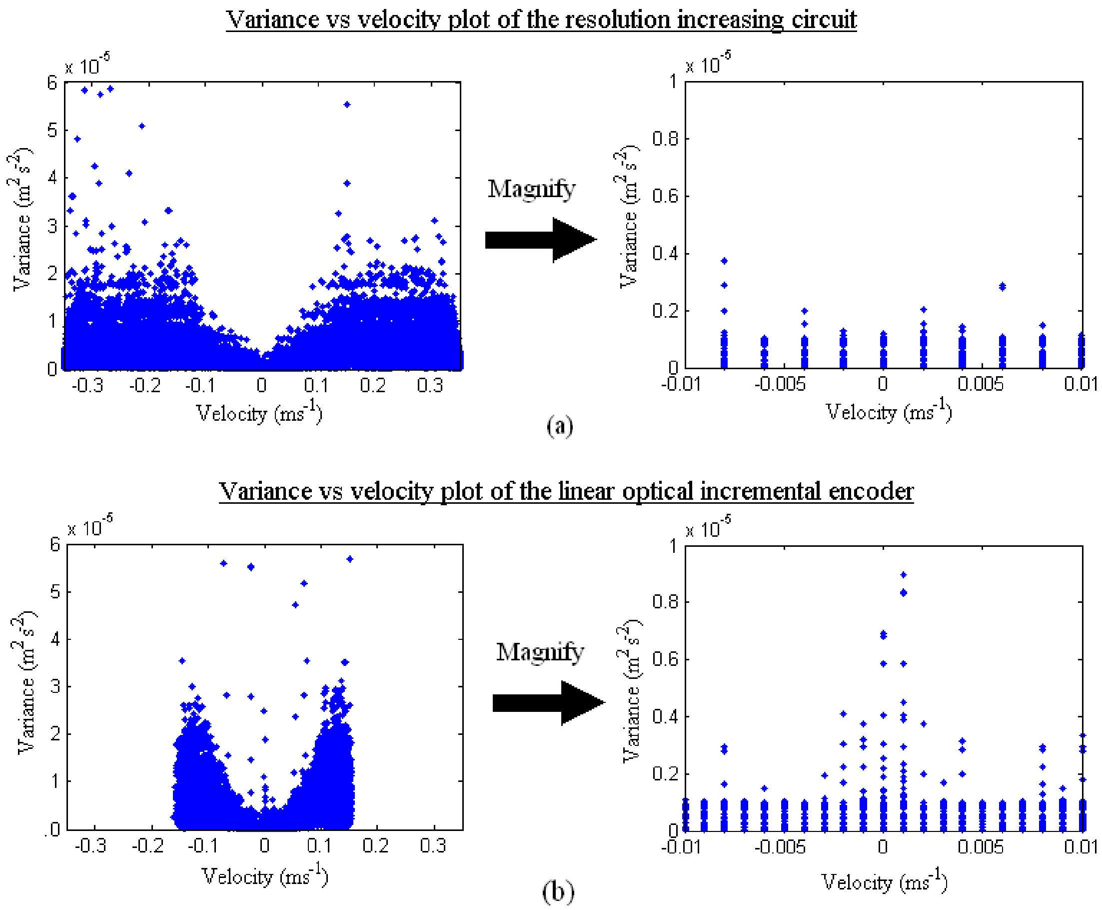

Fig.5-6 Variance-velocity graph of (a) resolution increasing circuit and (b) optical linear incremental encoder

The variance plots of the two sensing methods are very similar, except that the velocity ranges of them are different. The range difference is caused by the maximum measurement speed range of these two sensing methods. The maximum measurement speed of the optical linear incremental encoder is $0.175ms^{-1}$ and the maximum measurement speed of the resolution increasing circuit will be doubled and equal to $0.35ms^{-1}$. Referring the resolution of both velocity measuring systems (magnified graph of Fig. 5-6), the resolution of the resolution increasing circuit ($2mms^{-1}$) is two times of the optical linear incremental encoder ($1mms^{-1}$). This observation also proves that the proposed circuit can step-up the resolution of the incremental signal and enlarge the maximum measurement range. Referring the value of variance of both sensing methods, the mean value of variance of the linear incremental encoder is similar to that of the resolution increasing circuit.

5.2.2 Problems of the resolution increasing circuit

If the outputs of the resolution increasing circuit are converted to the position measurement, there will be a problem when the movable target reverses its traveling direction. During the experiment, the positions and the velocities measured by the optical linear incremental encoder and the resolution increasing circuit were recorded. The difference between two measured positions (error) was also calculated. All measured data are presented in Fig.5-7 and Fig. 5-7(b) is the magnified version of Fig.5-7(a).

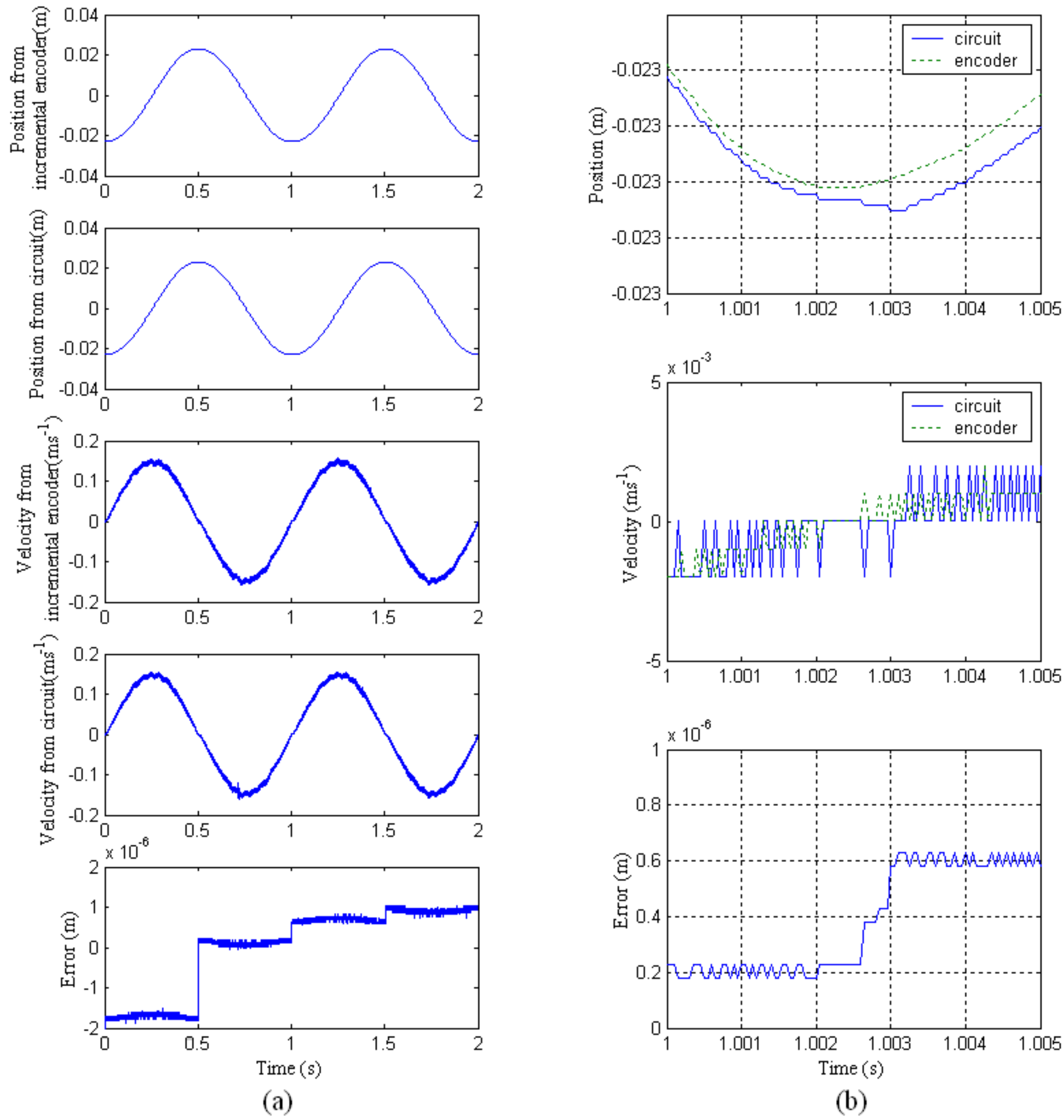

Fig.5-7(a) The position and velocity measurements from the optical linear incremental encoder and the resolution increasing circuit; Fig.5-7 (b) The magnified plot of Fig.5-7(a)

The most obvious problem appears when the velocity curve crosses zero. When the movable target reverses its direction, a "jump" appears in the error curve. This is caused by the abnormal state transition during the direction reversal. The stage sequence of the incremental encoder is recalled in order to explain the process. The stages are assigned with different names and the sequence of state transition is shown in Fig.5-8.

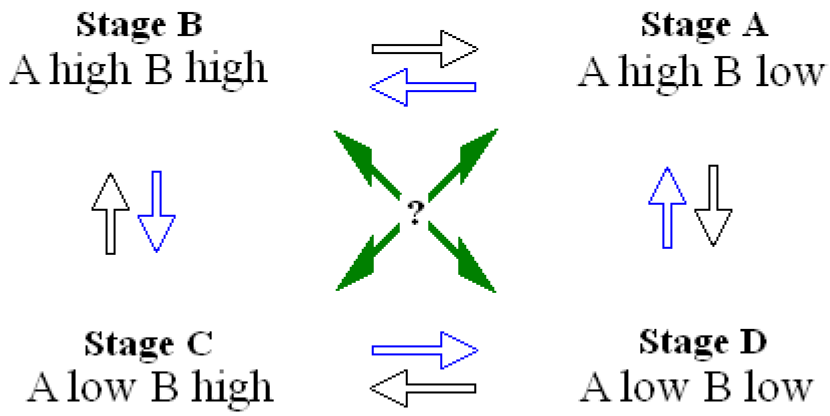

Fig.5-8 Stage sequence of quadrature signals with stage assignment

In the normal operation, the stage of outputs of incremental encoder is changed in hollow arrows direction and the decoder can operate properly. That means the position count will be added or subtracted by one if stage is changed normally. However, the proposed circuit develops some abnormal sequence as shown in solid arrows in Fig.5-8 when the movable target is reversing its direction. Consider the moments that the direction is reversed, stage of Phase A2 and Phase B2 jumps in the following patterns (referring the Fig. 5-4):

1) from stage B to stage D
2) from stage A to stage C
3) from stage D to stage B
4) from stage C to stage B

Once the abnormal state transition appears, the operation of decoder is perturbed and the decoder will give incorrect position count. As a result, the measured position will deviate from the actual position (as shown in the position-time graph of Fig. 5-7(b)). A data fusion algorithm is utilized to combine the information from the incremental encoder and the resolution increasing circuit in order to generate a correct measurement when the movable target is reversing its direction.

Another observation is related to the propagation delay of the resolution increasing circuit. Referring the error-time graph of Fig.5-7(a), the shape of the error curve is similar to the measured velocity and it should be because of the presence of the propagation delay in the resolution increasing circuit. The error curve is obtained by subtracting the position time graph of the resolution increasing circuit from the position time graph of the optical linear incremental encoder. The subtraction process is similar to velocity calculation (final position minus initial position). The equation for calculating the propagation time delay Δt can be proved as shown below:

$$B\cos(\omega t+\varepsilon)=A\sin(\omega t)-A\sin(\omega t-\omega\Delta t)$$

$$B\left[\cos(\omega t)\cos(\varepsilon)-\sin(\omega t)\sin(\varepsilon)\right]=A\sin(\omega t)-A\left[\sin(\omega t)\cos(\omega\Delta t)-\sin(\omega\Delta t)\cos(\omega t)\right]$$

$$\begin{cases} B\cos(\varepsilon)=A\sin(\omega\Delta t) \\ -B\sin(\varepsilon)=A\left[1-\cos(\omega\Delta t)\right] \end{cases}$$

$$B^2\cos^2(\varepsilon)+B^2\sin^2(\varepsilon)=A^2\sin^2(\omega\Delta t)+A^2\left[1-\cos(\omega\Delta t)\right]^2$$

$$B^2=A^2\sin^2(\omega\Delta t)+A^2\left[1-2\cos(\omega\Delta t)+\cos^2(\omega\Delta t)\right]$$

$$\Delta t=\frac{1}{\omega}\cos^{-1}\left(1-\frac{B^2}{2A^2}\right) \qquad (5.1)$$

where A is the amplitude of the position curve

B is the amplitude of the error curve

ε is the phase difference between error curve and the position curve

ω is the angular frequency of the position function

The propagation time delay Δt can be calculated by (5.1) and it is about 1.2μs.

5.3 Improvement of the resolution increasing circuit by the data fusion algorithm

The measurement from the resolution increasing circuit is not correct when the target is reversing direction, but the rest of the outputs can also be utilized. After the resolution of outputs of the incremental encoder has been stepped-up, the new outputs can provide a higher measurement velocity. By combining the outputs of the incremental encoder and the resolution increasing circuit, the improved measurement speed and high precision measuring system can be accomplished.

Based on the results from Fig.5-6, the variances of both sensing methods are nearly the same but the resolutions of them are different. The data fusion algorithm shown in (4.8) is therefore modified based on the idea in [25]. Instead of only using the variances of the sensors, the resolutions and the correctness of the measured data are also considered. Therefore, two varying weighting factors are defined as W_1 and W_2 for the optical linear incremental encoder and the resolution increasing circuit. The value of the W_1 and W_2 are the function of speed and they are shown in Fig.5-9.

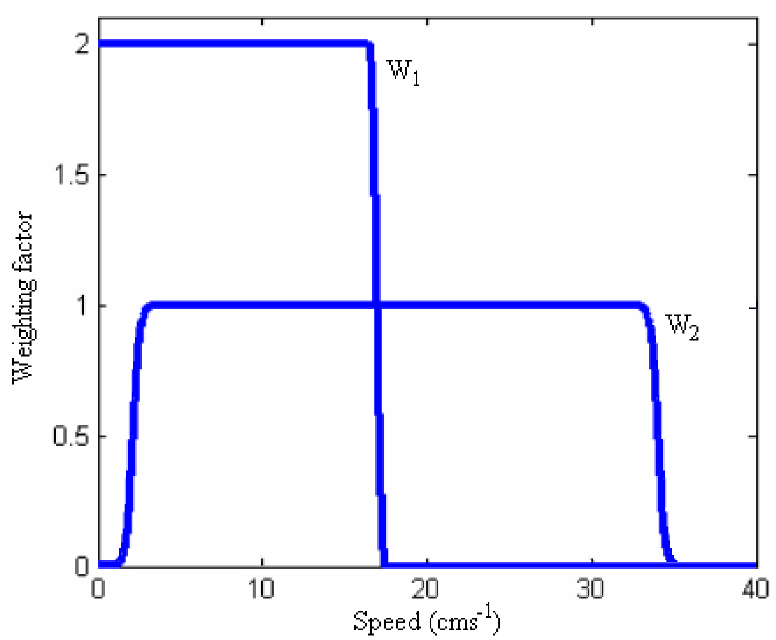

Fig.5-9 Weighting factors vs. velocity graph

Based on the properties and the accuracy of the two sensing methods, four speed regions can be defined as shown below:

1) The actual speed is low (i.e. the speed is lower than 10mms^{-1}):

   The resolution increasing circuit may operate under the abnormal state transition when the movable target is reversing its direction. W_2 is assigned to be zero in order to eliminate the abnormal measurement from the resolution increasing circuit disturbing the fused velocity. W_1 can be any non-zero value and it is assigned to be two.

2) The actual speed is between 10mms^{-1} and 160mms^{-1}:

   When the speed of the movable target is larger than 10mms^{-1}, W_2 can be larger than zero since the operation of resolution increasing circuit becomes normal. The variances of both sensing methods are nearly the same within this speed range and this means that their reliability is similar. However, if their resolution is also considered, the information from the optical linear incremental encoder will be more accurate compared with the information from the resolution increasing circuit. Therefore, W_1 is assigned to be two and W_2 is assigned to be one.

3) The actual speed is between 160mms^{-1} and 350mms^{-1}:

   When the target travels faster than 175mms^{-1}, the decoded information from the optical linear incremental encoder is no longer correct due to the limited clock frequency in the decoder. To prevent the perturbation from the incremental encoder, W_1 is assigned to be zero. At the same time, the information from the resolution increasing circuit is still correct and W_2 is therefore assigned to be a non-zero value ($W_2 = 1$).

4) The actual speed is higher than 350mms^{-1}:

   When the speed is larger than 350mms^{-1}, the information from the two sensors is no longer useful. Both W_1 and W_2 should be assigned as a very small value.

With the modification of weighting factors, the measured velocity from the two sensing methods can be combined to produce a fused velocity by (5.2).

$$fused\ \ velocity = \frac{v_{encoder} \times W_1 + v_{circuit} \times W_2}{W_1 + W_2} \tag{5.2}$$

where $v_{encoder}$ is the measured velocity from the optical linear incremental encoder

$v_{circuit}$ is the measured velocity from the resolution increasing circuit

W_1 is the weighting factor for the optical linear incremental encoder

W_2 is the weighting factor for the resolution increasing circuit

Note that when the actual speed is higher than 350mms^{-1}, W_1 and W_2 can not be both zero since the denominator of (5.2) can not be zero. The "undefined" fused velocity must be prevented and therefore W_1 is maintained at zero and W_2 is assigned as a small value 0.001.

5.4 Implementation and experimental results of the proposed data fusion algorithm

5.4.1 Implementation and experimental results

In order to verify the proposed fusion idea, the experimental setup shown in Fig. 5-10 is constructed with the equipments shown in Table 5-1.

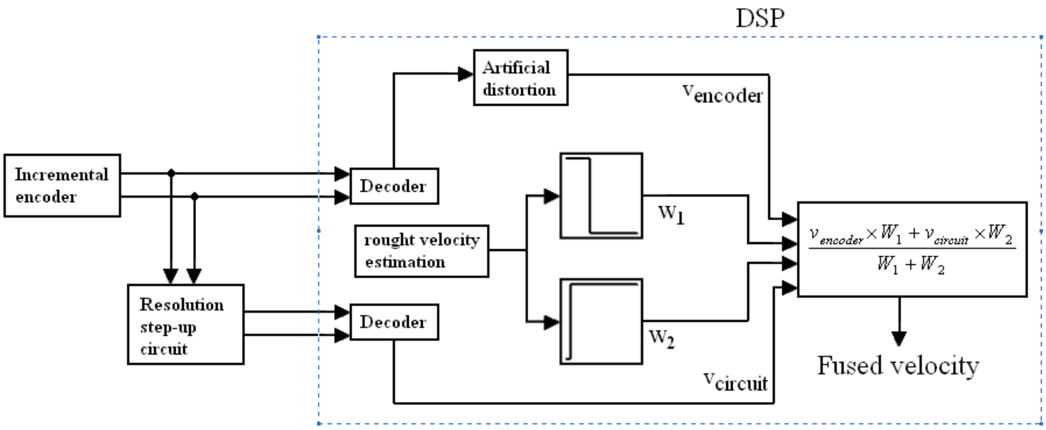

Fig.5-10 Experimental setup for the data fusion algorithm

The optical linear incremental encoder is connected to the first decoder embedded in DSP and the resolution setting of this decoder is 50nm. Meanwhile, the outputs of the resolution increasing circuit are connected to the second decoder in DSP and the corresponding resolution setting is 100nm. The "rough velocity estimation" in Fig. 5-10 is responsible for calculating W_1 and W_2. Note that the "rough velocity estimation" can be any velocity sensing method such as Hall Effect motion sensor or estimated velocity from back e.m.f. In this project, the estimation is provided by the outputs of the resolution increasing circuit. The PMLM is commanded to operate with velocities which are within the range between +330mms^{-1} and -330mms^{-1}. The measured positions and velocities from the optical linear incremental encoder, the resolution increasing circuit, and the data fusion algorithm are plotted as shown in Fig. 5-11(a-f). In this experiment, the outputs of the optical linear incremental encoder (before distortion) are acting as a reference velocity and a reference position. The difference between the reference position and the fused position is shown in Fig.5-11(g). The variance-velocity plot of fused velocity is also plotted and shown in Fig.5-12.

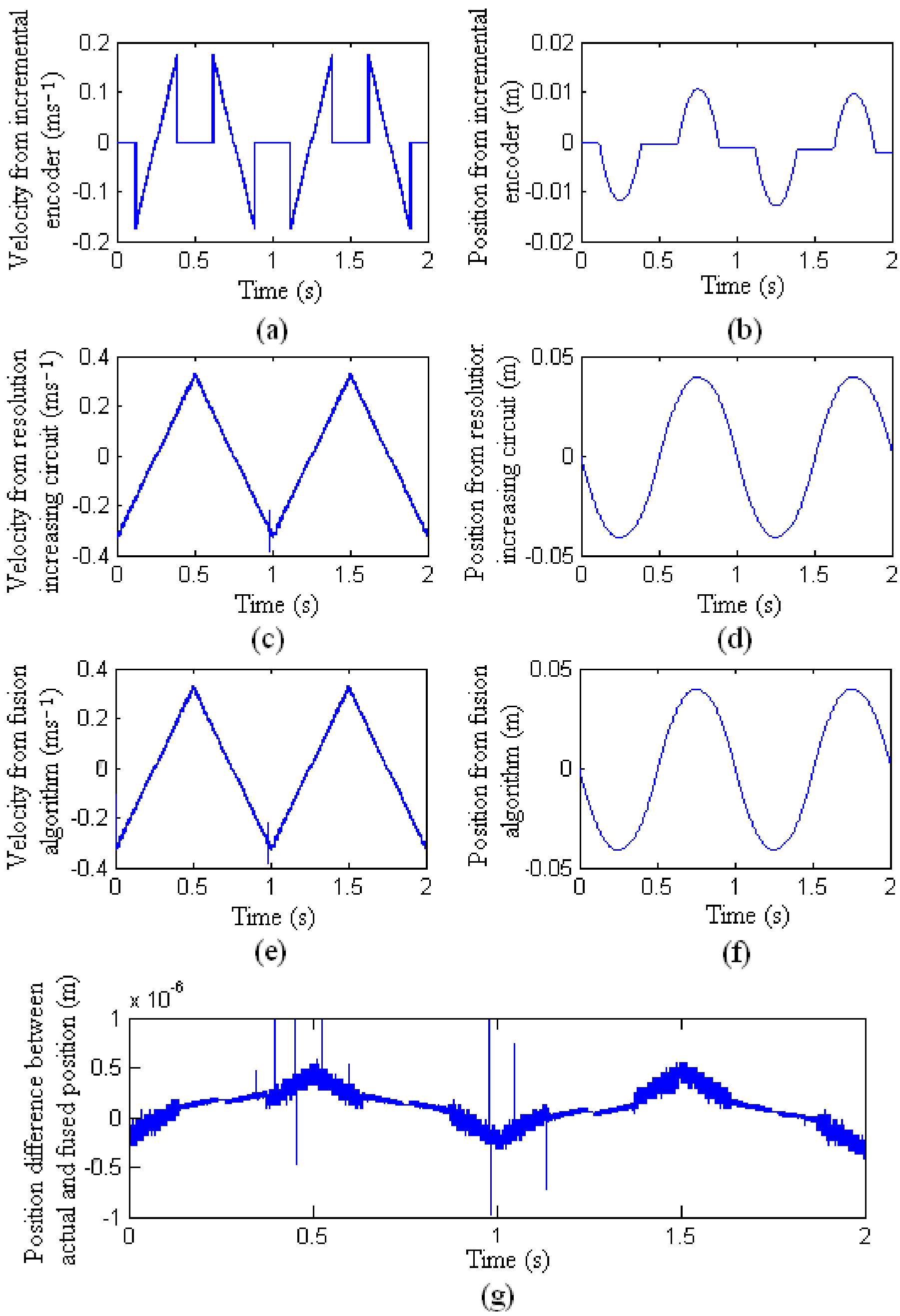

Fig.5-11 Experimental results for the data fusion algorithm; (a) the measured velocity from the optical linear incremental encoder; (b) the measured position from the optical linear incremental encoder; (c) the measured velocity from the resolution increasing circuit; (d) the measured position from the resolution increasing circuit; (e) the measured velocity from the fusion algorithm; (f) the measured position from the fusion algorithm; (g) the position difference between reference and fused position

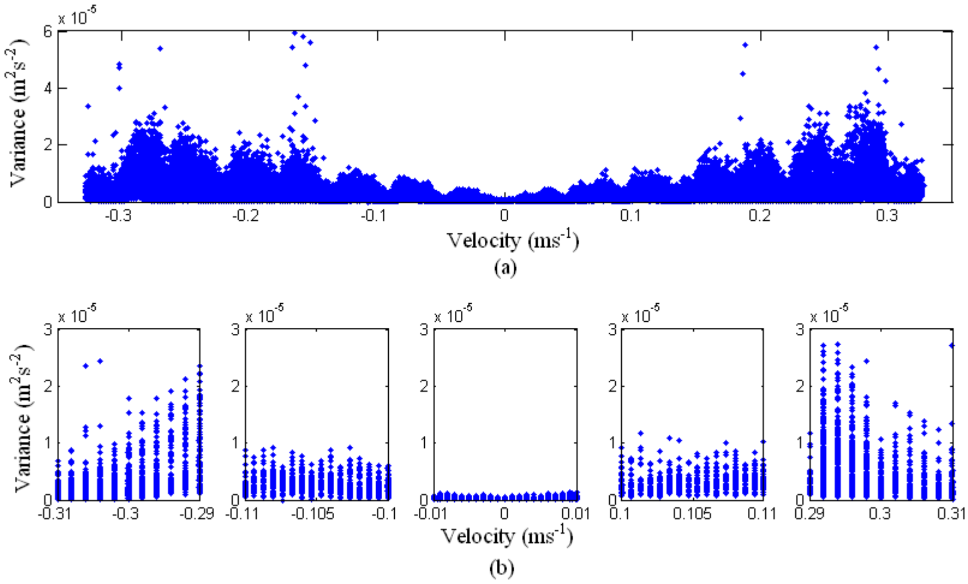

Fig.5-12 Variance vs. velocity graph of fused velocity; (a) ranged between +350mms^{-1} and -350mms^{-1}; (b) magnified plots with five different velocity ranges

5.4.2 Discussion on the performance of proposed data fusion algorithm

When the speed of the movable target is higher than 175mms^{-1}, the decoder with clock frequency 14MHz can not decode the information from the incremental encoder. This can be observed from the Fig.5-11 (a) and (b). When the speed is higher than 175mms^{-1}, the measured velocity and the converted position will not be correct.

The outputs of the resolution increasing circuit and the fused algorithm are shown in Fig. 5-11 (c)-(f). The "jump" phenomenon shown in Fig. 5-7, which is caused by the abnormal state sequence, has disappeared in the fused position as shown in Fig.5-11(g). The effect of abnormal state sequence can be eliminated by the proposed data fusion algorithm successfully.

Consider the variance plots shown in Fig.5-12, the value of variance of fused velocity is approximately equal to the variance of the resolution increasing circuit and the variance of the incremental encoder, but the resolution of the fused velocity is very different. There are three different values of resolution and they appear at different velocity ranges as shown below:

1) When speed is less than $10mms^{-1}$, the resolution is $1mms^{-1}$.
2) When speed is between $10mms^{-1}$ and $160mms^{-1}$, the resolution is $0.667mms^{-1}$.
3) When speed is higher than $160mms^{-1}$, the resolution is $2mms^{-1}$.

Another effect from the data fusion algorithm is observed when the speed of the movable target is between $10mms^{-1}$ and $160mms^{-1}$. The resolution of the fused velocity is $0.667mms^{-1}$, which is smaller than the resolution of the incremental encoder and the resolution increasing circuit. In other words, the accuracy of the output of fusion algorithm is more accurate than both of the original sensing methods.

5.5 Summary

This chapter has presented a novel delicate electronic circuitry, the resolution increasing circuit, to modify the outputs of the optical linear incremental encoder so as to provide a higher measurement speed. The performance of the resolution increasing circuit is investigated and its advantages and weaknesses are explored. By employing the data fusion algorithm and combining the information from both outputs (the outputs of the resolution increasing circuit and the optical linear incremental encoder), the shortcomings of the resolution increasing circuit can be overcome and a wider measurement speed range and high accuracy motion sensing system can be developed.

Chapter 6
Background studies on high precision linear motion system

6.1 Linear actuator for high precision linear motion system

Precise linear motion actuator has to be developed in order to convert electrical energy into mechanical energy in a single and linear direction. Generally, electro-mechanical machine is designed for rotating motion instead of linear motion. Some forms of mechanisms or methods have been developed for the conversion of rotary into linear motion. There are two approaches to achieve the linear motion output:

(1) The rotating machine drives the mechanism which converts the rotating motion into linear motion (indirect drive actuator).

(2) Re-designing the structure of the machine so that the new actuator converts the electrical energy into linear motion directly (direct drive actuator).

6.1.1 Indirect drive actuator for high precision linear motion system

The rotating motion from motor can be converted into linear motion through some mechanisms or devices such as gears and bearings. The force or torque is applied to the moving target indirectly. There are four typical examples of indirect drive actuator as shown below: [26]

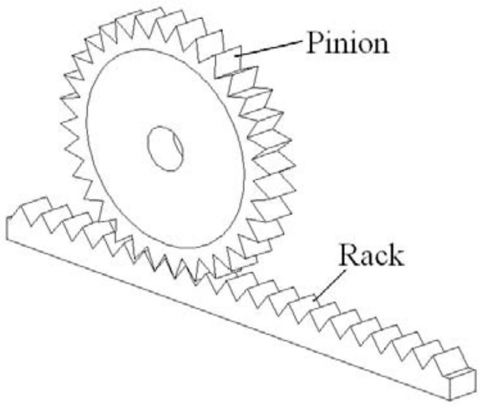

Fig.6-1(a) Rack and pinion system

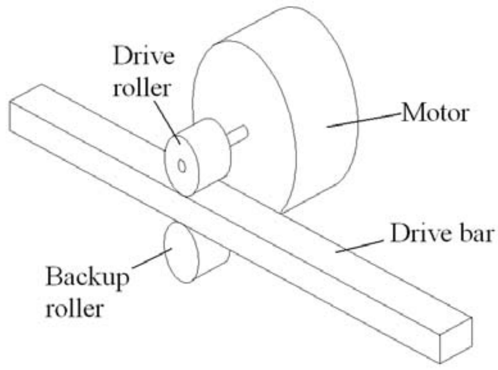

Fig.6-1(b) Friction drive system

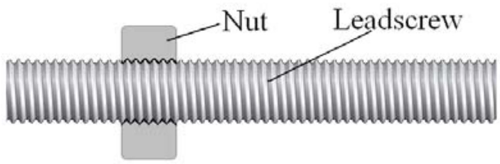

Fig. 6-1(c) Leadscrews and nuts

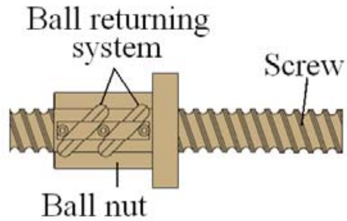

Fig. 6-1(d) Ball bearing system

Example 1: Rack and pinion system (Fig.6-1(a))

It is difficult to obtain the optimal transmission ratio for the system and it needs to operate at a low speed in order to generate a high force and to achieve high precision linear motion.

Example 2: Friction drive (Fig.6-1(b))

This kind of driving system provides the minimum backlash and deadband. The design of this system is not complicated. The disadvantages of this system are low drive force, low stiffness, minimal transmission gain, and the occurrence of hysteresis or damping.

Example 3: Leadscrews and nuts (Fig.6-1(c))

This is a low efficiency linear motion system with a high friction and stiction. However, it features a self-lock mechanism which automatically operates when the motor is stopped. Also, this system can be manufactured easily.

Example 4: Ball screw (Fig.6-1(d))

The friction of the mechanism is minimized, and it helps to establish the high precision linear motion. Backlash is effectively eliminated and efficiency of this system is also greatly improved as compared to leadscrews and nuts system. Since ball bearings are employed, ball returning system is necessary. The whole system becomes bulky, complicated, and very expensive.

6.1.2 Direct drive actuator for high precision linear motion system

A direct drive actuator is an electromagnetic device which converts the input electrical energy into linear motion without other transmission mechanism such as gears and bearings. Brushless PMLM is a type of direct drive actuator for a high precision linear motion system. The reasons are: [27]

1) Permanent magnets can replace the field excitation system in the motor. No excitation loss is absorbed and, therefore, the efficiency of the system can be improved.
2) Higher thrust force and output power can be produced compared with an indirect drive system if same amount of input energy is applied.
3) Higher magnetic flux density in air gap can be provided and thus better performance can be achieved.

4) Construction of a brushless PMLM is simple.

5) A brushless motor requires less maintenance and experiences less loss.

Three types of brushless PMLM which are typically utilized in a high precision linear motion controlled system are suggested in [28]. They are forcer-platen linear motor, U-shaped linear motor, and tubular linear motor.

The **forcer- platen linear motor** is a brushless DC servo motor which has been developed for more than 40 years [28]. The structure of this motor is quite simple and is shown in Fig.6-2.

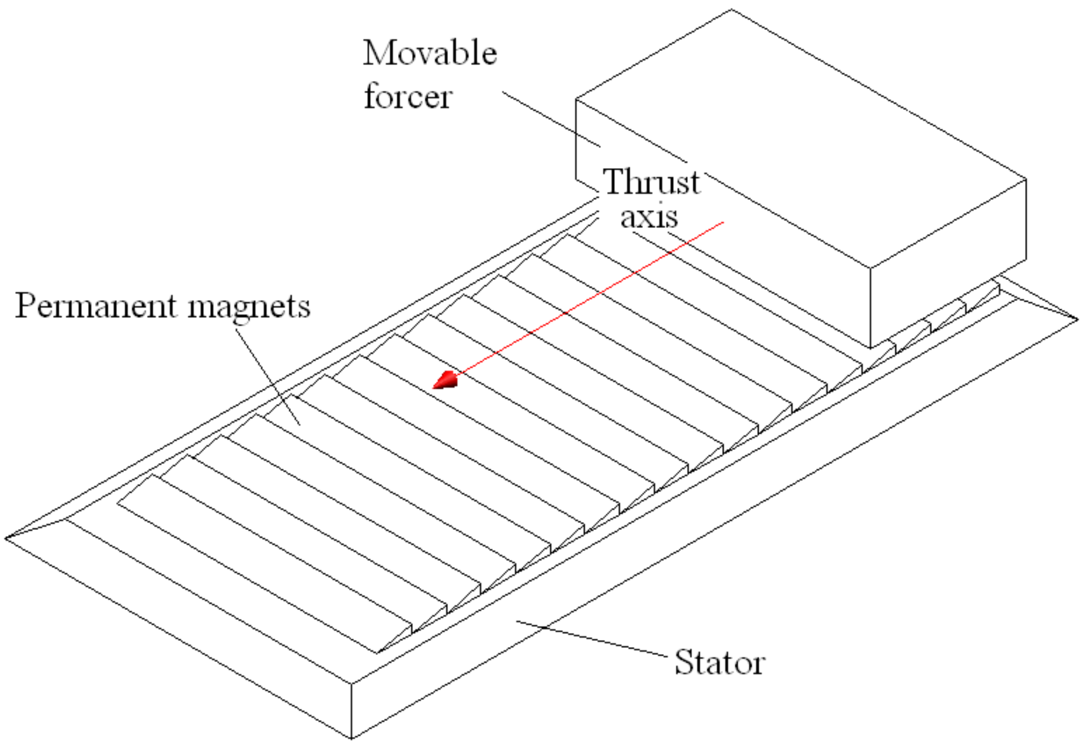

Fig.6-2 Forcer-platen linear motor

The motor includes a movable forcer and a stationary platen consisting of permanent magnets. The magnetic field from the permanent magnets is perpendicular to the thrust axis. When current is injected to the conductors inside the forcer, the electromagnetic thrust force will exert onto the movable forcer, which will travel along the thrust axis.

The forcer contains iron cores which cause the cogging force and eddy current. A large amount of heat is generated, and magnetic saturation commonly occurs. Forced cooling is necessary in order to improve the performance of the PMLM. In general, the permanent magnets are often skewed slightly so as to reduce the force ripple effect. However, skewing of magnets can not maximize the thrust force from the forcer, so that higher current is necessary to compromise this arrangement and substantial heat loss will occur. Between the stationary platen and forcer, a narrow air gap (less than 0.5mm) has to be maintained rigidly. The fluctuation in air gap width will cause the thrust force variations. Therefore, the installation of forcer-platen linear motor is complex.

The **U-shaped linear motor** is commonly used in high precision linear motion system. The arrangement of the motor is shown in Fig.6-3. The armature of this motor consists of a planar winding which is epoxy bounded to form a plastic blade. This movable armature is placed between two rows of magnets (U-shaped). Since the winding is immersed inside the magnetic field, electromagnetic force (thrust force) can be induced by injecting current into the windings of armature. This type of motor has no detent force and attractive force between stator and translator. The motion of this motor is smooth and cost effective design. In addition, the traveling range can be long and no precise air gap is required.

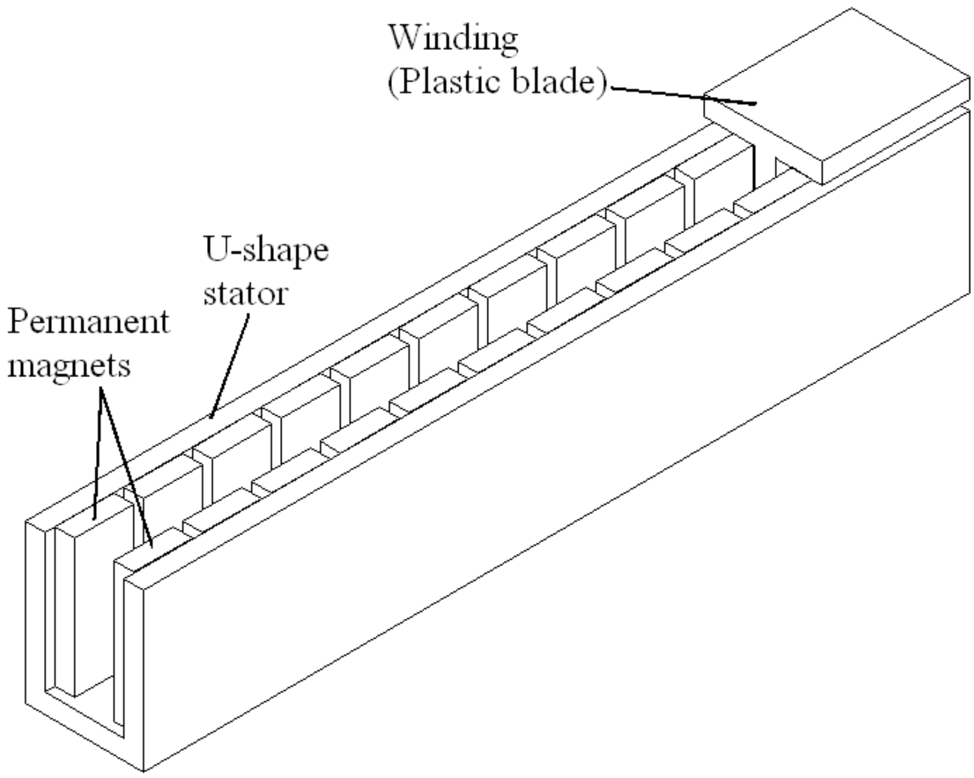

Fig.6-3 U-shaped linear motor

The armature of the motor has no iron core and is protected by low stiffness epoxy. When the motor is carrying a high current and is traveling with a high acceleration, resonance in the armature occurs easily. The heat generated from the armature is trapped in the U-shaped rail. This large amount of hot air must be eliminated by forced cooling or large heat sink. Note that the arrangement of permanent magnets in this motor results in inefficient utilization of magnetic flux.

A **tubular linear motor** consists of a thrust rod and a movable translator and it is shown in Fig. 6-4. The thrust rod is made of a column of permanent magnets and the movable translator consists of a set of coils. From the point of view of force generation and energy efficiency, this motor arrangement is most effective since this type of motor can fully utilize the magnetic flux from the permanent magnets.

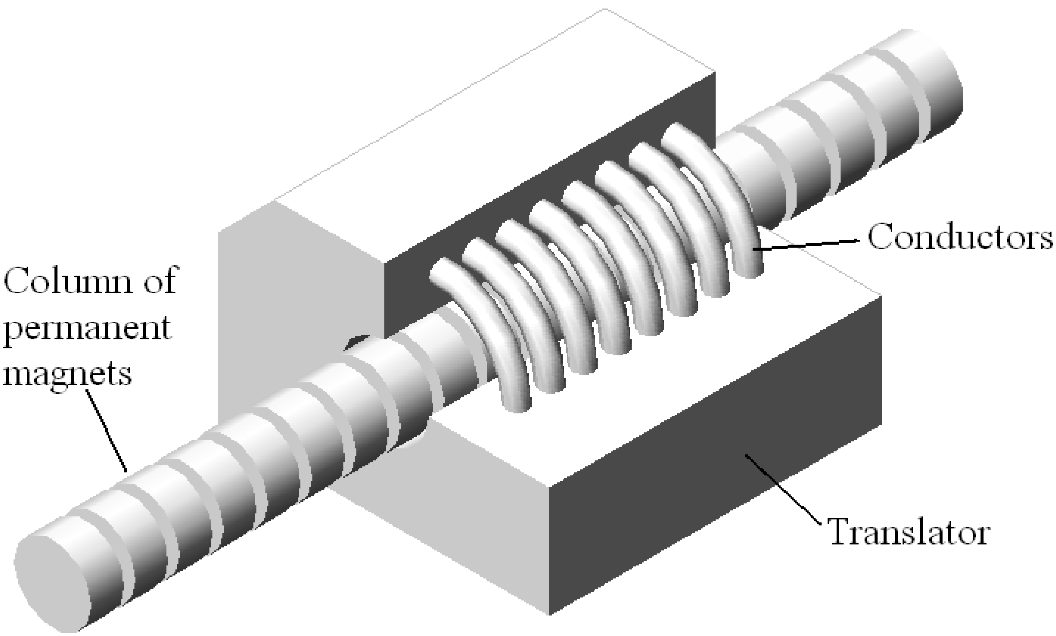

Fig. 6-4 Tubular linear motor

The separation of the air gap of this motor (around 1mm) has little restriction and it can be much wider than that in the “forcer-platen motor” and the “U-shaped linear motor”. Therefore, the installation of this motor is easier and simpler. All the magnetic flux intersects the coils perpendicularly and the maximum thrust force can be generated. In addition, the symmetrical structure of the motor balances the B-field and reduces the attractive force between the translator and the stator. Regarding to the heat generation of the coil, the thrust block is installed on the outside surface of the motor and heat can be dissipated from the heat radiator.

However, since both ends of the thrust rod have to be supported, the traveling distance of the actuator is limited. Also the rod is sagged under its own weight. The size of this type of motor is relatively large and its overall height is tall.

6.1.3 Summary

Different types of linear actuators which can be utilized in high precision motion system have been mentioned in this section. Indirect drive actuators including “rack and pinion”, “friction drive”, “leadscrews and nut”, and “ball screw” are discussed and their pros and cons are pinpointed. Regarding to direct drive actuators, the most popular one for high precision motion system is PMLM and three common configurations of this type of motor are also investigated. These include “force-platen linear motor”, “U-shape linear motor”, and “tubular linear motor”.

After this study, it is obvious that the direct drive actuator is more suitable for constructing high precision motion systems. Compared with indirect drive actuators, direct drive actuators require less maintenance and provide higher efficiency since they are absence of conversion mechanisms. The actuator which is the most suitable for high precision linear motor is the tubular linear motor. The separation of air gap has little restriction so that installation is much simpler and its production cost is cheaper. It also offers the advantages of high efficiency, high acceleration density, less maintenance requirements. This type of actuator is therefore employed in this thesis.

6.2 Problems encountered in implementing high precision motion control using the PMLM

Although the PMLM stands on a vantage point for accomplishing the high precision linear motion system, some problems still need to be solved.

6.2.1 Force ripple

PMLM drives by a sequence of attracting and repelling forces between the poles and permanent magnets. The force exerting on the translator is known as thrust force which is along the thrust axis. If ferromagnetic core is used for the windings, force ripples will exist and increase the difficulty of achieving high precision motion control. The force ripple consists of two components: cogging and reluctance force [28].

Cogging force is caused by the mutual attraction between the permanent magnets and the iron core even when no current is injected to the coil. The cogging force exhibits a periodic relationship with respect to the position of the translator. Reluctance force is caused by variation in the self inductance of the winding. The reluctance force is related to the relative position between windings and permanent magnets. Note that these two forces are periodic in nature.

The effect of force ripple dominates at low velocities. It is because the translator has very low momentum to overcome the magnetic force. Since the actuator of the PMLM is direct-driven, the force ripple effect will significantly and directly affect the accuracy in controlled position. Force ripple phenomenon is causing oscillation and stability problem. Handling this phenomenon is an important issue during the high precision linear motion control.

The force ripple can be modeled as:

$$F_{ripple}(x) = A_{ripple}(x, \dot{x})\sin(\omega x + \theta) \tag{6.1}$$

where A_{ripple} is the amplitude of force ripple which is function of position

ω is the angular frequency of the force ripple function

θ is the initial phase for x is zero

Note that the ripple periodic is independent on the velocity and it is related to the position of translator. The amplitude of the ripple depends on the position and the velocity of the translator. If the translator travels faster, the amplitude of the ripple will be smaller [28].

6.2.2 Friction

Friction is present in all moving mechanisms in the real world and it is the major obstacle to achieve high precision motion control. Friction can be further divided into static and dynamic. Static friction includes stiction, kinetic force, viscous force, and Stribeck effect. The dynamic characteristics include pre-sliding displacement, varying breakaway force, and frictional lag. Many friction models are developed for achieving high precision motion system. One of the classical friction models which include Stribeck effect is described as below [29]:

$$F_{friction} = \begin{cases} F_{fri\_\mathrm{model}}(\dot{x}) & if \quad \dot{x} \neq 0 \\ F_e & if \quad \dot{x} = 0 \quad and \quad |F_e| < F_s \\ F_s \cdot \mathrm{sgn}(F_e) & if \quad \dot{x} = 0 \quad and \quad |F_e| \geq F_s \end{cases} \tag{6.2}$$

where F_{fri_model} is the model of friction

F_e is the external applied force

F_s is the maximum value of the static friction

Note that F_{fri_model} is a non-linear velocity function and this friction model is shown in Fig. 6-5. There are many variations to this model and they are summarized in [29]. For example, Bo and Pavelescu [30] developed as "exponential friction model", Tustin [31] built another friction model called "Tustin friction model", Canudas and his colleagues [32] constructed a "non-linear friction model" for the friction when velocity is not equal to zero. For better accuracy, some researchers developed the friction model by using the "seven parameter friction model" [33] and "LuGre friction model" [34].

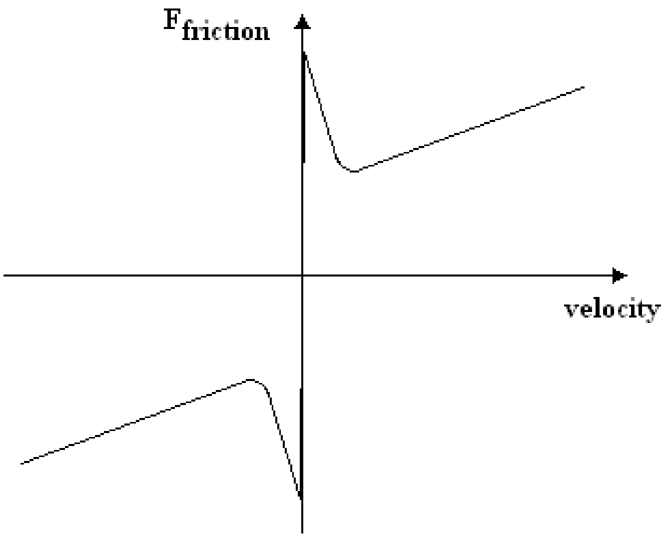

Fig. 6-5 Classical friction model

6.2.3 Model uncertainties

When the system model is being developed for a high precision linear motion system, a balance must be strike between these two objectives:

1) to build a simple motion control algorithm, and
2) to provide adequate information for high precision motion control.

[35] mentioned some categories of model uncertainties. They are summarized as shown below:

Category 1: Unstructured uncertainties

When the system is obtained by analyzing the frequency response, the frequency range of the plot is usually limited due to the noise corruption. Only the low frequency part of the model can be accurately constructed and the high frequency model may not be reliable. This kind of model uncertainty is called unstructured uncertainties.

This uncertainty or perturbation can be classified into three different types. They are additive, multiplicative, and stable factor perturbation. For the actual system function $P(s)$ and the model of the plant $P_m(s) = N_m(s)/D_m(s)$, three perturbation models can be described as:

Additive perturbation model: $P(s) = P_m(s) + \Delta_a(s)$ (6.3)

Multiplicative perturbation model: $P(s) = P_m(s)(1 + \Delta_m(s))$ (6.4)

Stable factor perturbation model: $P(s) = \dfrac{N_m(s) + \Delta_n(s)}{D_m(s) + \Delta_d(s)}$ (6.5)

where $\Delta_a(s)$ is additive plant perturbation

$\Delta_m(s)$ is multiplicative plant perturbation

$\Delta_n(s)$, $\Delta_d(s)$ are stable factor perturbations

Category 2: Structured uncertainties

The mathematical equations of the system are accurately formulated, but some parameters of the plants are relatively small and hence they may be neglected during the modeling process. This can simplify the controller design but gives rise to structured uncertainties.

For example, the model of PMLM without non-linear disturbance can be formulated as:

$$\frac{\dot{X}(s)}{V_{apply}(s)} = \frac{1}{\frac{L_a M}{K_f} s^2 + \frac{R_a M}{K_f} s + K_e} \approx \frac{1}{\frac{R_a M}{K_f} s + K_e} \tag{6.6}$$

where $X(s)$ is position of the motor

$V_{apply}(s)$ is input voltage

L_a is the armature inductance

M is mass of the translator

K_f is force constant

R_a is armature resistance

K_e is back e.m.f constant

In some applications, the armature inductance L_a is small compared with other parameters. L_a may be neglected in order to simplify the order of the system model and the controller design.

Category 3: Parameter variation

Even when there is absence of the model uncertainties, the parameters of the system will be affected by environment or the state of the system. For example, the operating temperature will affect the armature resistance R_a, while the self inductance of armature L_a is usually affected by the operating frequency and the position of PMLM translator.

6.2.4 Load variation

Apart from the problem of ripple force and friction, load variation is another dominant factor in high precision linear motion application. In the industrial environment, linear motors are often responsible for pick and place jobs which require transporting loads with varying weight. This variable external load force will affect the performance of linear motion control. The controller parameters have to be adjusted for different loads and this causes a complex controller in a linear motor system.

6.2.5 Summary

PMLM is a suitable motor for a high precision linear motion system. It can overcome the major problems such as backlash and hysteresis. However, some obstacles still have to be overcome. They include force ripple phenomenon, friction, model uncertainties, and load variation.

With the knowledge of limitation of PMLM, suitable control algorithm can be developed to reduce the effect of limitation and to achieve a precision positioning system. In this thesis, a solution is suggested to solve the problems of force ripple phenomenon, friction, load variation, and parameters uncertainties.

6.3 Modeling of permanent magnet linear motor and motor drive

The model of PMLM is formulated in the following sections. In addition, the transfer functions and performances of the motor drive are also reviewed.

6.3.1 Scalar modeling of PMLM

The PMLM can be modeled by the following equations [28]:

Mechanical equation: $F_{thrust} = M\ddot{x} + F_{friction} + F_{ripple} + F_{load}$ (6.7)

Electrical equation: $K_e\dot{x} + L_a\dfrac{dI_a}{dt} + R_a I_a = V_{applied}$ (6.8)

Force equation: $F_{thrust} = K_f I_a$ (6.9)

where M is mass of translator

F_{thrust} is thrust force from the motor

F_{load} is load force

$F_{friction}$ is frictional force

F_{ripple} is ripple force

K_e is back e.m.f. constant

L_a is armature inductance

I_a is armature current

R_a is armature resistance

V_{apply} is applied voltage

K_f is force constant

(6.7), (6.8) and (6.9) can be joined together and they can be represented by a block diagram as shown in Fig.6-6. Note that the electrical time constant is typically much smaller than the mechanical time constant (since L_a is relatively small) and therefore the combined equation can be formed as shown in (6.10).

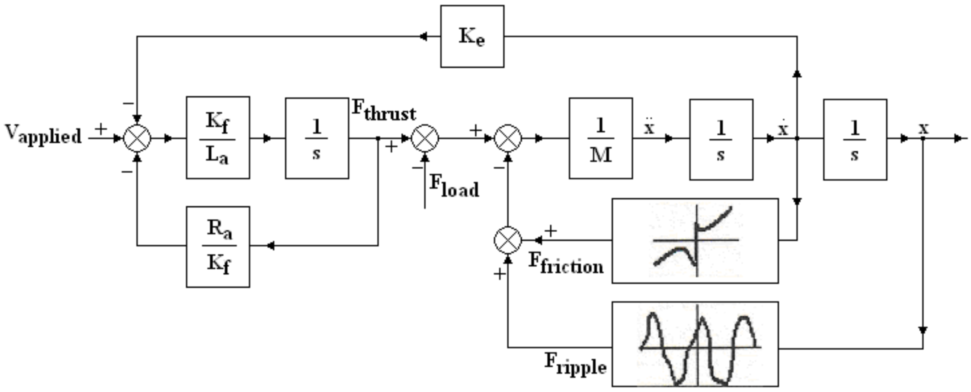

Fig.6-6 Block diagram of PMLM

$$\ddot{x} = -\frac{K_e K_f}{MR_a}\dot{x} + \frac{K_f}{MR_a}V_{applied} - \frac{1}{M}(F_{load} + F_{friction} + F_{ripple}) \tag{6.10}$$

This is a second order linear dynamical model with non-linear perturbation such as friction and force ripple.

6.3.2 Vector modeling of PMLM

The vector modeling of PMLM can be modified from vector model of rotating permanent magnet motor which has been developed in [36] and [37]. Fig.6-7 shows the mounting of the magnets on the rotor. This kind of magnets arrangement can provide the highest air gap flux density. The rotor magnet axis is defined as the direct axis (d-axis) and the inter-polar axis is the quadrature axis (q-axis). Before the motor is modeling, the following assumptions have to be made:

1) Rotor flux concentrated along the d-axis

2) Zero flux along the q-axis

3) Core loss is neglected

4) Rotor flux is constant at a given operating point between the rotor and the stator

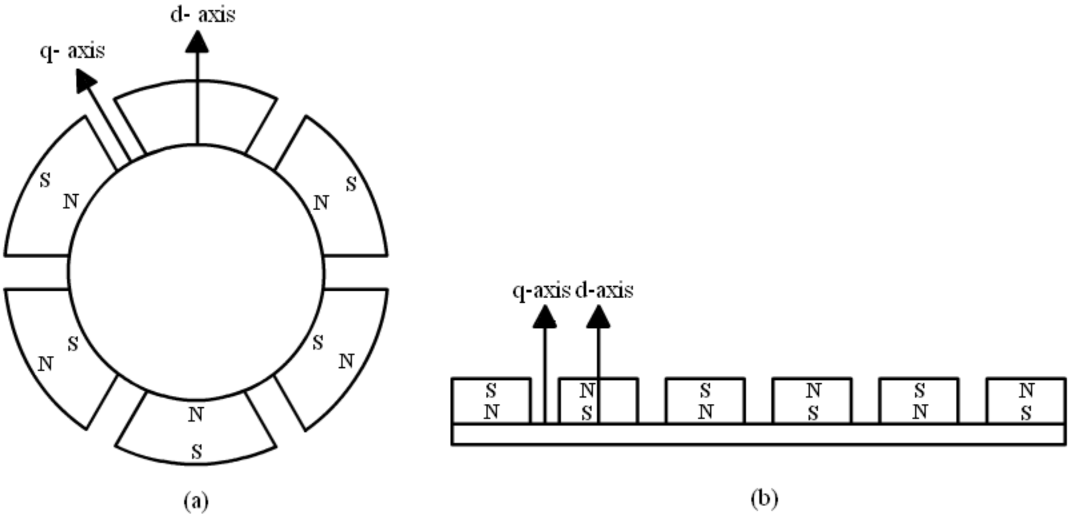

Fig.6-7 d-axis and q-axis definition for (a) rotor of the rotating permanent magnet motor; (b) stator of PMLM

When the speed of rotor is steady, there is no speed difference between the stator rotating field and rotor rotating speed. Both axes of the stator and the rotor have a fixed phase relationship (i.e. the phase is δ). The stator equations referred to the rotor axis can be formulated and shown in (6.11).

$$
\begin{aligned}
V_{qs} &= R_q i_{qs} + \frac{d}{dt}\lambda_{qs} + \omega_r \lambda_{ds} \\
V_{ds} &= R_d i_{ds} + \frac{d}{dt}\lambda_{ds} + \omega_r \lambda_{qs}
\end{aligned}
\tag{6.11}
$$

where	R_q	is	q-axis winding resistance of stator
	R_d	is	d-axis winding resistance of stator
	d/dt	is	differential operator
	ω_r	is	applied electrical frequency
	λ_{qs}, λ_{ds}	are	stator flux linkages
	i_{qs} , i_{ds}	are	the stator currents
	V_{qs}, V_{ds}	are	the stator voltages

The resistance R_d and R_q are equal and it is assigned as R_s. The stator flux linkages can be obtained as shown in (6.12)

$$\begin{aligned} \lambda_{qs} &= L_q i_{qs} + L_m i_{qr} \\ \lambda_{ds} &= L_d i_{ds} + L_m i_{dr} \end{aligned} \tag{6.12}$$

where	L_m	is	mutual inductance between stator winding and rotor magnets
	i_{qr}, i_{dr}	are	the rotor current

The self-inductances of the stator q- and d- axes windings are equal to L_s only when the rotor magnets have arc of electrical 180^o. However, it is not always true in practical situation. These two inductances are d-axis and q-axis synchronous inductances and they vary with the phase angle δ. The inductance for d-axis and q-axis are named as L_d and L_q. Note that if the stator winding (d-axis) is facing the rotor magnet axis, the reluctance referred to the d-axis is maximum value and the reluctance referred to the q-axis is minimum value. When the phase δ is fixed in space, the winding inductance does not change.

The rotor is permanent magnet and all magnetic flux is concentrated along the d-axis. The excitation can be modeled as a constant current, i.e. $i_{dr} = i_{fr}$. In addition, since there is no flux along the q-axis, i_{qr} is equal to zero. The stator flux linkage and the motor d-q model can be modified as shown in (6.13) and (6.14) respectively.

$$\begin{aligned} \lambda_{qs} &= L_q i_{qs} \\ \lambda_{ds} &= L_d i_{ds} + L_m i_{fr} \end{aligned} \tag{6.13}$$

$$\begin{bmatrix} V_{qs} \\ V_{ds} \end{bmatrix} = \begin{bmatrix} R_s + \dfrac{d}{dt} L_q & \omega_r L_d \\ -\omega_r L_q & R_s + \dfrac{d}{dt} L_d \end{bmatrix} \begin{bmatrix} i_{qs} \\ i_{ds} \end{bmatrix} + \begin{bmatrix} \omega_r L_m i_{fr} \\ 0 \end{bmatrix} \tag{6.14}$$

6.3.3 Operation of PWM Driver

A three phase permanent linear motor is usually driven by a PWM driver because it is able to achieve 70~90% efficiency [28]. The PWM amplifier converts sinusoidal signals into six sets of pulse trains with a variable duty cycle. Six pulse trains are utilized to drive the motor through the bridge circuit. The most important advantage of implementing the PWM driver is reducing the order of harmonics in the input voltage. The basic structure of the three phase PWM driver is shown in Fig.6-8. This driver consists of a three-phase bridge inverter, an oscillator, and a drive circuitry. The gate driver signals (G1-G6) can be described as shown in Fig.6-9. Note that the terminals V_a, V_b, and V_c are the applied voltages to the input terminals of the PMLM. Also, G1-G6 are varying with the inputted control command.

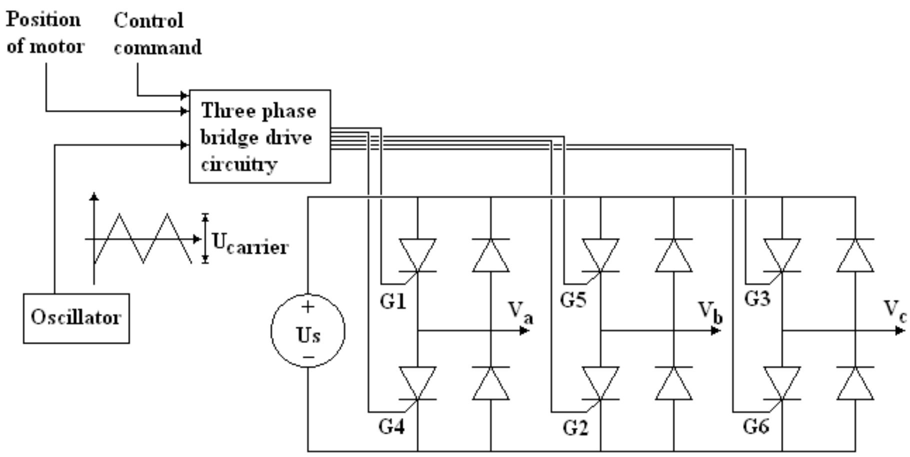

Fig.6-8 Basic structure of a PWM amplifier

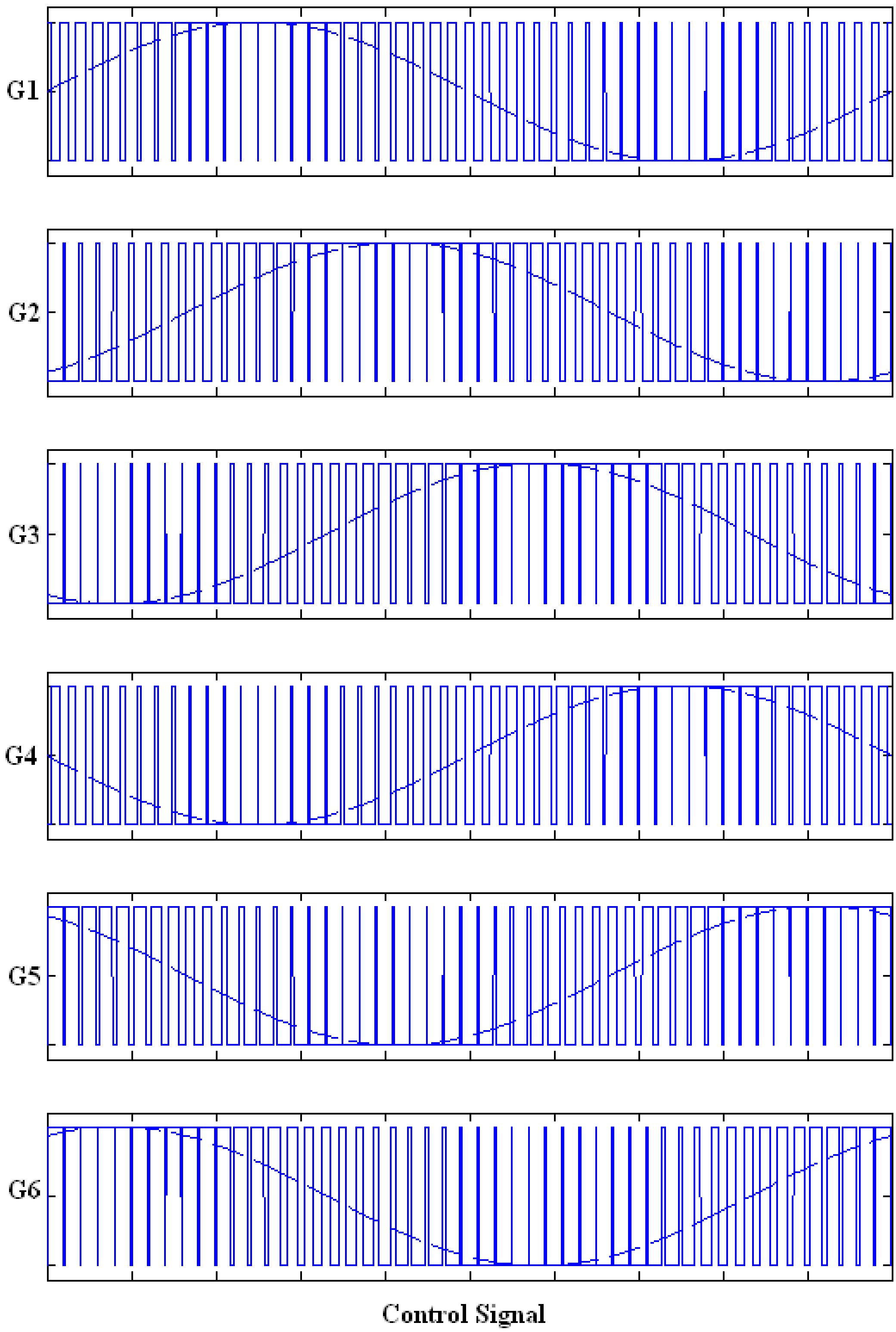

Fig.6-9 Three-phase gate driver signals (solid lines show the pulse signals and dash lines illustrate the fundamental harmonic of the pulse signals)

The three outputs of the PWM driver (V_a, V_b, V_c) are expected to be three pulse trains with a variable duty cycle. Let the amplitude of the fundamental of the driver outputs be u_{h1} and the amplitude of control command voltage be u_{cmd}, the transfer function of the PWM driver $G_{PWM}(s)$ can be described as:

$$G_{PWM}(s) = \frac{u_{h1}}{u_{cmd}} = \frac{2U_s}{U_{carrier}} \tag{6.15}$$

Note that the phase of the transfer function is expected to be small and neglected. The ratio of u_{h1}/u_{cmd} should be equal to $2U_s/U_{carrier}$ because the gain is assumed to be linear. Overall, the transfer function of PWM driver is a constant gain $2U_s/U_{carrier}$.

6.3.4 The PMLM driving algorithm (constant force operation)

The driving algorithms are usually derived based on a rotating motor instead of a linear motor. In this section, the driving strategies for the permanent magnet rotating motor are discussed. The conversion between rotating motor and linear motor are then carried out and the corresponding control algorithms are derived.

Referring [36], there are five common control strategies for permanent magnet rotating motors which are:

1) Constant torque operation

2) Unit power-factor control

3) Constant mutual air gap flux-linkages control

4) Optimum torque-per-ampere control

5) Flux-weakening control

In this thesis, the PWM driver is configured to operate in the current mode. It is suitable for constant force / torque operation. This control methodology is being explained in this section.

The input power of the PMLM P_{in} can be formulated in term of d-q model parameters.

$$
\begin{aligned}
P_{in} &= (V_a i_a + V_b i_b + V_c i_c) \\
&= \frac{3}{2}(V_d i_d + V_q i_q) + 3V_0 i_0 \\
&= \frac{3}{2}[R_s(i_q{}^2 + i_d{}^2) + i_q(\frac{d}{dt}\lambda_q) + i_d(\frac{d}{dt}\lambda_d) + \omega_r(\lambda_d i_q - \lambda_q i_d)] \\
&\quad + 3R_0 i_0{}^2 + 3i_0(\frac{d}{dt}\lambda_0)
\end{aligned}
$$

where V_a, V_b, V_c are the applied voltage to motor

i_a, i_b, i_c are the injected currents to motor

V_d, V_q, V_0 are the applied voltages to motor in d-q frame

i_d, i_q, i_0 are the injected currents to motor in d-q frame

After the ohmic losses and the rate of change in magnetic energy have been eliminated, the electromagnetic power output P_{out} and electromagnetic torque T_{em} can be described as:

$$P_{out} = \frac{3}{2}\omega_r(\lambda_d i_q - \lambda_q i_d) = \frac{3}{2}\frac{p}{2}\omega_{mr}(\lambda_d i_q - \lambda_q i_d) \tag{6.16}$$

$$T_{em} = \frac{3}{2}\frac{p}{2}(\lambda_d i_q - \lambda_q i_d) = \frac{3}{2}\frac{p}{2}[L_m i_{fr} i_q + (L_d - L_q) i_q i_d] \tag{6.17}$$

where p is number of poles

ω_{mr} is mechanical angular speed of the rotor

Generally, the input currents to the motor are described in (6.18) and these three components can be transformed to d-q axis of rotor by Park's transformation as shown in (6.19):

$$\begin{bmatrix} i_a \\ i_b \\ i_c \end{bmatrix} = I_s \begin{bmatrix} \sin(\omega_r t + \delta) \\ \sin(\omega_r t + \delta - \frac{2\pi}{3}) \\ \sin(\omega_r t + \delta + \frac{2\pi}{3}) \end{bmatrix} \tag{6.18}$$

$$\begin{bmatrix} i_q \\ i_d \end{bmatrix} = \begin{bmatrix} \cos(\omega_r t) & \cos(\omega_r t - \frac{2\pi}{3}) & \cos(\omega_r t + \frac{2\pi}{3}) \\ \sin(\omega_r t) & \sin(\omega_r t - \frac{2\pi}{3}) & \sin(\omega_r t + \frac{2\pi}{3}) \end{bmatrix} \begin{bmatrix} \sin(\omega_r t + \delta) \\ \sin(\omega_r t + \delta - \frac{2\pi}{3}) \\ \sin(\omega_r t + \delta + \frac{2\pi}{3}) \end{bmatrix} I_s$$

$$= I_s \begin{bmatrix} \sin(\delta) \\ \cos(\delta) \end{bmatrix} \tag{6.19}$$

where I_s is the amplitude of the current

By substituting (6.19) into (6.17), the electromagnetic torque can be calculated based on the following equation:

$$T_{em} = \frac{3}{2}\frac{p}{2}[\frac{1}{2}(L_d - L_q)I_s^{\,2}\sin(2\delta) + L_m i_{fr} i_s \sin(\delta)] \tag{6.20}$$

For constant torque operation, the motor is operated with $\delta = 90^{o}$ and T_{em} is as shown in (6.21) and the motor model is given by (6.22).

$$T_{em} = \frac{3}{2}\frac{p}{2}[L_m i_{fr} I_s] = K_t I_s \tag{6.21}$$

$$\begin{aligned} V_{qs} &= R_q I_s + \omega_r L_m i_{fr} \\ V_{ds} &= -\omega_r L_q I_s \end{aligned} \tag{6.22}$$

where K_t is the torque constant

It should be noted that the main objective of this section is developing the model for the PMLM instead of the rotating motor. The equations of the rotating machine can be transformed into linear motor by the relationship as shown in (6.23) and the force equation can become (6.24).

$$\omega_r = \frac{2\pi}{x_p}(\dot{x}) \tag{6.23}$$

$$F_{em} = \frac{3}{2}\frac{p}{2}\frac{2\pi}{x_p}[L_m i_{fr} I_s] = K_f I_s \tag{6.24}$$

where K_f is the force constant

6.3.5 Summary

The linear motion system employed in this thesis (PMLM) has been modeled as the scalar model and the vector model. The control strategy used by the PMLM driver is constant force operation and the details of this operation are also highlighted.

With the actual model of PMLM and the detail of constant force operation, the relationship between the injected current and thrust force generated by in a PMLM is obtained in (6.24). Based on this relationship which links the electrical parameter to mechanical parameter, the development of the control algorithm for high precision linear motion can be realized.

6.4 Control algorithm

Many engineers have paid much effort to achieve high precision motion control. They used different approaches to cope with the non-linear phenomenon in a PMLM and handle the problems mentioned in the previous section. These approaches are summarized in the following sections.

6.4.1 Composite control

This control algorithm includes feed-forward control and PID feedback control [28]. It is commonly used in industrial applications for many years since it is simple and easy to apply. The block diagram of this algorithm is shown in Fig.6-10:

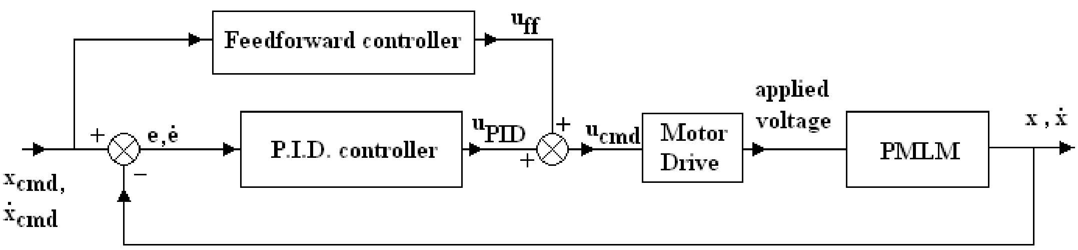

Fig.6-10 Composite control scheme

The PMLM can be modeled with an uncertain and nonlinear perturbation. The model of the motor is reviewed again before the composite control algorithm is explained. Let

$$K_1 = \frac{K_e K_f}{R_a},$$
$$K_2 = \frac{K_f}{R_a}, \tag{6.25}$$
$$\frac{K_2}{M} f_1(x,\dot{x}) = \frac{1}{M}(F_{load} + F_{friction} + F_{ripple})$$

Assumption shown in (6.25) can simplify the model as shown in (6.26)

$$\ddot{x} = -\frac{K_1}{M}\dot{x} + \frac{K_2}{M}u_{cmd} + \frac{K_2}{M} f_1(x,\dot{x}) \tag{6.26}$$

For tracking error e defined from command position x_{cmd} and actual position x:

$$e = x_{cmd} - x \tag{6.27}$$

(6.26) can be expressed as:

$$\ddot{e} = -\frac{K_1}{M}\dot{e} - \frac{K_2}{M}V_{applied} - \frac{K_2}{M} f_1(x,\dot{x}) + \frac{K_2}{M}\left(\frac{M}{K_2}\ddot{x}_{cmd} + \frac{K_1}{K_2}\dot{x}_{cmd}\right) \tag{6.28}$$

As shown in (6.28), the last two terms in the equation will cause residual acceleration error $\ddot{e}$ and they have to be eliminated by a suitable control method.

Feed-forward control is a straightforward control method to eliminate the residual $\ddot{e}$. Referring (6.28), the term $\frac{K_2}{M}\left(\frac{M}{K_2}\ddot{x}_{cmd} + \frac{K_1}{K_2}\dot{x}_{cmd}\right)$ can be eliminated by injecting a feed-forward control signal u_{ff} which is added through the applied voltage and it is designed as:

$$u_{ff} = -\frac{M}{K_2}\ddot{x}_d - \frac{K_1}{K_2}\dot{x}_d \tag{6.29}$$

Obviously, x_{cmd} must be twice differentiable in order to develop a proper control signal. A filter has to be added after u_{ff} in case x_{cmd} is not twice differentiable. In addition, this control method can be further applied to compensate the non-linear function $-\frac{K_2}{M} f_1(x, \dot{x})$ if the models of the non-linear functions $f_1(x, \dot{x})$ are formulated. The performance critically depends on the accuracy of the model parameter.

Three-term PID controller is widely accepted by the manufacturing industry, because of its simple, effective, and reliable structure. More complex controllers are less preferred by motor operators, although these controllers can provide better performance. In addition, complex controllers require a higher cost for implementation and more efforts for control tuning. It is difficult for operators to handle the unfamiliar advanced tuning algorithm.

The PID control signal u_{PID} utilized for full-state feedback is shown below:

$$u_{PID} = k_p e + k_i \int e dt + k_d \dot{e} \tag{6.30}$$

where k_p, k_i, and k_d are gains in the PID controller

The PID controller can provide specific control action designed for specific process requirements by tuning k_p, k_i, and k_d. The performance of the controller can be described in terms of steady state error, the degree of overshoot, and the degree of system oscillation. Note that the use of the PID algorithm for control does not guarantee optimal control of the system or system stability.

Referring [38] and [39], some engineers develop pre-defined tuning methods, such as Ziegler-Nichols tuning rules and relay auto-tuner, in order to provide some easier ways for choosing k_p, k_i, and k_d. For some advanced control schemes, the optimal PID control parameters are calculated by Linear Quadratic Regulator technique so that the optimal and robust performance can be obtained.

6.4.2 Adaptive feed-forward compensation

Force ripple can be minimized and eliminated by changing the structure of the motor. However, the cost of re-construction of motor is very high and only experienced engineers can handle the modification. Force ripple can also be compensated by using a suitable control method. The feed-forward control mentioned in the previous section can be further modified into an adaptive feed-forward control algorithm (AFC). In [28] and [40], the equations of AFC for force ripple are formulated and the details are given in the rest of this section.

Although the force ripple is a periodic function of position and this periodic characteristic does not vary with velocity, the amplitude of the ripple force may not be constant and it will vary with the velocity and position of the translator. Assume the actual ripple force is shown as below:

$$F_{ripple}(x) = A_{ripple}(x)\sin(\omega x + \phi) = A_1(x)\sin(\omega x) + A_2(x)\cos(\omega x) \qquad (6.31)$$

The ripple force can be viewed as a response to a virtual input which is perturbing the system. This virtual input is shown below:

$$V_{ripple}(x) = A'_1(x)\sin(\omega x) + A'_2(x)\cos(\omega x) \qquad (6.32)$$

A control signal V_{afc} is injected to the motor so that the force ripple can be neutralized. V_{afc} is designed as:

$$V_{afc}(x) = a_1(x)\sin(\omega x) + a_2(x)\cos(\omega x) \qquad (6.33)$$

The system output x due to V_{ripple} and V_{afc} can be formulated and shown below:

$$x = P(s)\begin{bmatrix} a_1(x) + A'_1(x) & a_2(x) + A'_2(x) \end{bmatrix}\begin{bmatrix} \sin(\omega x) \\ \cos(\omega x) \end{bmatrix} \tag{6.34}$$

where $P(s)$ is the function of the system.

(6.34) fulfills the standard framework of adaptive control theory [41]. Therefore, the possible update laws for the parameters $\begin{bmatrix} a_1(x) & a_2(x) \end{bmatrix}$ can be:

$$\dot{a}_1(x(t)) = -ge\sin(\omega x) \tag{6.35}$$

$$\dot{a}_2(x(t)) = -ge\cos(\omega x) \tag{6.36}$$

where g is an adaptive gain

e is the tracking error

Note that the friction can be compensated by a similar method. When the model of friction is obtained, the friction can be compensated if the model of friction can be obtained precisely.

6.4.3 Robust adaptive control

A robust adaptive controlled system usually includes a controller, parameter index, and automatic gain adjustment algorithm. This control method optimizes the performance of the system over the operating range by adjusting the parameters of the controller. The adjustment mechanism utilizes the control signal, system output, and the performance of the system to determine the parameters of controller so as to improve the performance of the motor. The adaptive control mechanism can be integrated with many control algorithms to achieve high precision motion control.

The first common integrated algorithm is sliding mode control (SMC). For example, in [28] and [42], adaptive control is combined with SMC to develop a controlled system which compensates the friction and force ripple. [43] provides another control strategy which is adaptive pole placement control scheme integrated with SMC. This proposed control scheme can achieve a fast transient response and reduce the effect of parametric uncertainties, disturbance, temperature change, and load variation.

Another robust control algorithm utilized in a precision controlled system is model reference adaptive control (MRAC). [28] and [44] show the basic idea of MRAC. The goal of this control method is adjusting the controller so that the output of the plant can follow the output of the reference model. [45] shows the MRAC can be further integrated with neural network so that a robust system can be achieved.

The robust adaptive control method usually requires a full understanding of the plant model and it also requires that the control engineer completely understands the mathematical equations. This is also one of the difficulties of achieving precision motion control with this method.

6.4.4 Iterative learning control

Iterative learning control belongs to a model-free learning algorithm in order to enhance PID feedback controller. The objective of this method is to feed-forward a control signal to reject the disturbance and compensate the non-linearity. This algorithm is designed to be repetitive in nature. Memory storages are essential for saving the tracking error and control efforts of the present cycle. Fig.6-11 shows the procedure of iterative learning control algorithm. Note that this kind of control algorithm requires careful variable initialization and rejection of the noise in velocity.

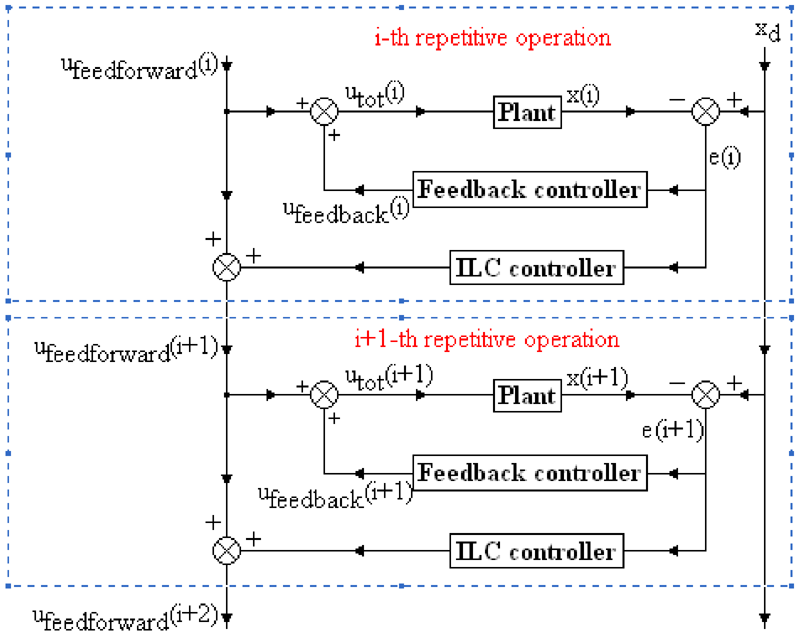

Remark:

$u_{tot}^{(k)}$: command injected to Plant at k-th operation

$u_{feedback}^{(k)}$: command calculated from feedback controller at k-th operation

$u_{feedforward}^{(k)}$: command calculated from ILC controller at k-th operation

$x^{(k)}$: output at k-th operation

$e^{(k)}$: position error at k-th operation

Fig.6-11 Iterative learning control algorithm

Many engineers are motivated by this model-free control algorithm and developed some ILC controller. For example, in [28], [46], and [47], ILC controller is incorporated with PID control algorithm so that a stable and high precision linear motion system can be achieved. In addition, ILC can be further applied to minimize the periodic force ripple.

6.4.5 Disturbance observation and cancellation

In order to control the PMLM to achieve high precision motion, some unavoidable limitations have to be considered. Load change, system parameters perturbation owing to continuous usage, measurement noise, high frequencies generated from amplifier (PWM), and non-linear dynamics are some common problems perturbing the outputs of the PMLM. If the outputs (can be velocity or position of the PMLM) are disturbed, the high precision of the controlled system will be affected. Some engineers focused on deriving equation of disturbances from the inputs and outputs of the system. A disturbance observer based on the outputs and control signal is therefore developed as shown in [22], [48], and [49]. This compensation scheme can be summarized and described as shown in Fig.6-12.

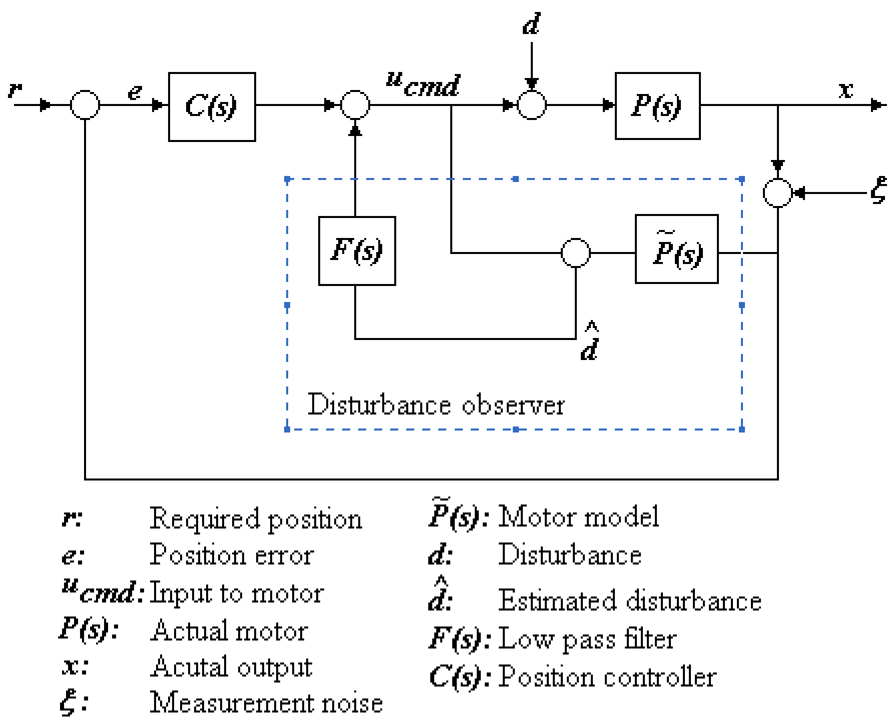

Fig.6-12 The disturbance observer

The transfer function of the PMLM *P(s)* is driven by a control signal u_{cmd}. The estimated disturbance $\hat{d}$ is calculated by the observer which is represented by the dotted box in Fig.6-12. This estimated value is converted to a compensation signal and added back to u through a function *F(s)*. Note that a low-pass filter *F(s)* is designed to ensure that the observer is proper and practical. The compensated signal cancels the actual disturbance d and the resultant process is expected to be disturbance-free. Therefore, better transient and steady state performance can be accomplished through the controller.

6.4.6 Summary

In order to develop a suitable control algorithm, recent researches related to high precision motion are reviewed and their methods are summarized. Generally, the higher order mathematical model for the linear motion system must be developed for building a robust controller. The system models including plant model (PMLM) and external disturbance model are formulated by control engineers. Theoretically, engineers can develop an ideal controller based on the accurate model and achieve the high precision linear motion control easily. However, a perfect model is not easy to be obtained in an actual system. Even though the accurate model can be obtained, a complex controller is usually needed in order to handle the perturbations and external disturbance.

Many engineers, therefore, deliberately use the adaptive control method to obtain the unknown parameters of the plant and develop a robust controller. One of the most significant phenomena, force ripple and friction, can also be minimized by adaptive control method. However, this adaptive control algorithm requires tedious calculation and mathematical derivations. It definitely increases the cost and the difficulty when the controlled system is implemented.

Some engineers utilized ILC to build the controller so as to eliminate the model obtaining process and integrate ILC with traditional PID control algorithm to achieve linear motion control. In addition, the designed controller can also reduce the effect of force ripple and friction. However, since the rule of ILC is determined by engineers, the method is only suitable for experienced users in order to prevent unstable performance. This will increase the difficulty of controller design.

Instead of employing difficult control algorithm to eliminate the appeared obstructions when high precision linear motion system is constructed, some engineers develop disturbance observers and compensators which aim to detect and reduce the effect of disturbances and perturbations. Estimated disturbances are converted to the feedback control signals for perturbation rejection. This compensation method is deliberately employed in this thesis in order to achieve a disturbance-free linear motion system by using simple algebraic calculation only. As a result, the controller for accomplishing a high precision linear motion system will be much easier and simpler.

Chapter 7
High precision motion control with non-linear uncertainty elimination for PMLM

The proposed control method for PMLM is shown in Fig.7-1. A PMLM is driven by a power amplifier which is configured as current driven mode. The velocity and the current command are utilized to estimate the actual disturbances and this estimation is converted into the compensation current by a “disturbance observer and compensator”. This disturbance compensator is a variable structure which is adjusted based on the position error and the operating speed so that the response time on the disturbance can be further improved. The compensated PMLM (disturbance-free motion system) is controlled by an “Internal Model Reference Control Algorithm” with the feedback velocity and position. The detail of each part will be introduced in following sections.

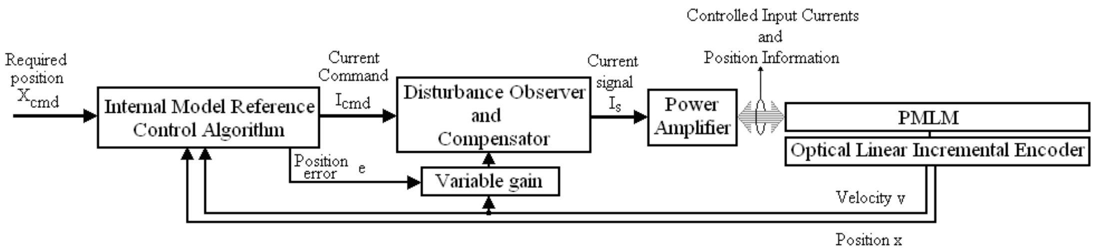

Fig.7-1 Overall block diagram of the proposed linear motion system

Compared with the adaptive IMRC algorithm proposed for many years [50-54], the main difference between the new proposed algorithm and other algorithms is the adaptive mechanism. The general adaptive IMRC algorithm adjusts the structure of the controllers as shown in [50-54] in order to tackle the parameter variation in the plant. However, the new proposed algorithm modifies the structure of the plant which is the “compensated PMLM”. This arrangement can separate the parameter variation compensation and the performance adjustment. From the point of view of the control, this arrangement and the algorithm formulation are much easier.

7.1 Conventional disturbance observer and compensator

The problems including force ripple, friction, and load variations often appear when a high precision motion controlled system is constructed. These perturbations and disturbances interrupt the outputs and performances of the PMLM. They may also cause the fluctuation in outputs and the non-zero steady state error, which reduce the precision of the controlled system.

The general method for accomplishing high precision linear motion system is to obtain the accurate system model, including the non-linear characteristics and external disturbances, etc. However, even though the exact model can be obtained perfectly, the complex controller design process raises the cost and the difficulty during the design process. Another issue is the uncertainty in model parameters, which may lead engineers to adopt a complex adaptive control law to calculate the actual system parameters. In this chapter, the author designs and develops a simple engineering solution for accomplishing a high precision linear motion system. The presented method uses a modified disturbance compensator and an internal model reference control algorithm so as to eliminate the external disturbance and drive the output of PMLM to follow the pre-defined trajectory precisely.

7.1.1 Model of PMLM

If the PMLM motor is driven under its rated speed and the direct axis current is equal to zero, the motor will be operated at the constant force operation [36] and the thrust force F_{em} from motor can be calculated by

$$F_{em} = K_f \times I_s \tag{7.1}$$

K_f and I_s in (7.1) are the force constant and current injected to the motor. (7.1) can be also treated as the model of PMLM. Although the structure of this model is very simple, many engineers [49, 55-57] also employed (7.1) during the controllers design and achieved the high precision motion control. Typically, the direct drive motion system is directly affected by the external disturbances F_{dis}. In other words, this nonlinear F_{dis} perturbs the outputs of the PMLM (velocity v and position x) directly. F_{dis} includes the load variation, force ripple, and some unexpected external disturbances. F_{em} has to overcome F_{dis} and friction to drive the translator of the PMLM. This is an important issue, especially, concerned in precision motion control system.

Note that the conventional disturbance compensation method was adopted by many engineers. [28, 49, 58] are some examples using this disturbance compensator to achieve high precision linear motion control. In this chapter, this conventional method is modified to develop the new compensator. The design process and the operating principle of a conventional disturbance compensator are therefore first reviewed in detail.

7.1.2 Operation of conventional disturbance observer and compensator

In order to minimize the effect of perturbation on PMLM, the "disturbance observer and compensator" are proposed. This observer and compensator are based on the idea mentioned in [49]. The structure of disturbance observer and compensator are shown in Fig.7-2(a). If the equation of the "plant" is formulated, the relationship between I_s and v will be arranged as shown below:

$$I_s(\Delta K_f + K_{fn}) + F_{dis} = (M_n s + \Delta M s + D)v \tag{7.2}$$

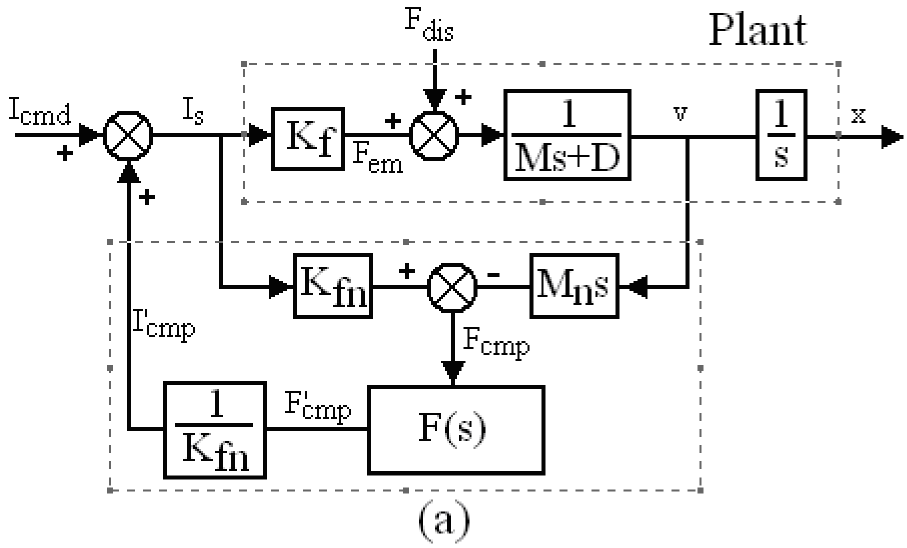

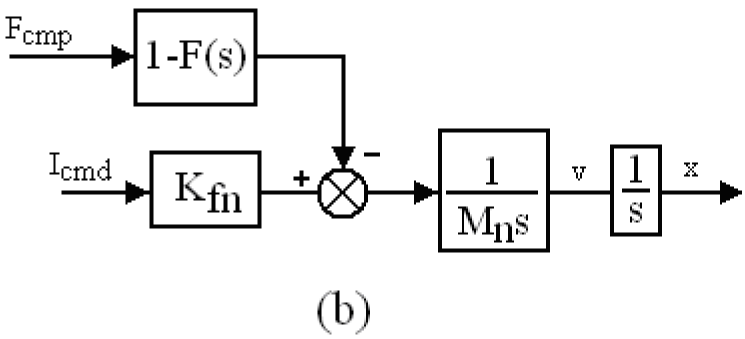

Fig.7-2(a) Block diagram of motion system with disturbance observer and compensator; and (b) Simplified block diagram of motion system

The parameters in Fig.7-2 (a) can be modified by providing their deviation as shown below:

K_f = $K_{fn}+\Delta K_f$ (Nominal force constant + deviation of force constant)

M = $M_n+\Delta M$ (Nominal mass + deviation of mass)

D = viscosity constant

The nominal parameters (M_n and K_{fn}) can be obtained from the datasheets and they usually have slight deviations from the actual values (M and K_f). If all the non-linear disturbances, friction, and deviation terms are grouped together, (7.2) can be rearranged as shown below:

$$F_{cmp} = \Delta M s v + D v - I_s \Delta K_f - F_{dis} = I_s K_{fn} - M_n s v \tag{7.3}$$

External disturbances F_{dis}, kinetic frictional force Dv, and parameter variation $\Delta M_s v\text{-}I_s\Delta K_f$ are grouped as a term called the compensation force F_{cmp} which can be calculated by measuring I_s and v. In fact, this F_{cmp} has to be compensated so that the PMLM can be operated as an ideal model as shown in (7.4) and Fig.7-3:

$$I_{cmd} = \frac{M_n}{K_{fn}} s v \tag{7.4}$$

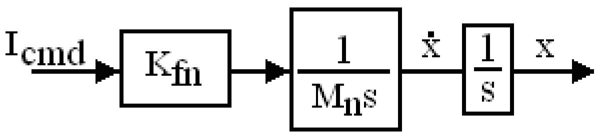

Fig.7-3 Ideal compensated motion model

Compared with the compensator in [49], the new proposed compensator in this thesis also compensates the term Dv, which is not totally rejected by the method in [49]. Since F_{cmp} is calculated by the derivative of velocity dv/dt, a LPF has to be inserted to suppress the high frequency noise in F_{cmp}. The function of LPF is named as $F(s)$. The filtered estimation F'_{cmp} is then converted into the compensation current I'_{cmp} by multiplying a gain $1/K_{fn}$. I'_{cmp} is fed-back to the thrust current I_s so that all low frequency disturbances and frictional force are compensated.

With the presence of LPF, the equation of the compensated PMLM will become (7.5), which is modified from (7.3). The block diagram of the system is shown in Fig.7-2(b).

$$(I_{cmd} + \frac{1}{K_{fn}} F(s) F_{cmp}) K_{fn} - M_n s v = F_{cmp}$$
$$I_{cmd} K_{fn} - M_n s v = [1 - F(s)] F_{cmp} \tag{7.5}$$

7.1.3 Filter design

The design of LPF is a critical process of constructing the “disturbance observer and compensator” since the selection of cutoff frequency of LPF (g_f / 2π) will directly influence the performance of compensation. There are four criteria to determine the value of cutoff frequency g_f:

1) The main function of the LPF is to filter the noise in $I_s K_{fn} - M_n s v$ which mainly comes from the differentiation of velocity. The frequency of noise in acceleration will be $f_{sampling}/2$, where $f_{sampling}$ is the sampling frequency of the DSP. The cutoff frequency of LPF should be much smaller than $f_{sampling}/2$ (i.e. $g_f < \pi \times f_{sampling}$).

2) Consider the input of LPF (I_sK_{fn}-M_nsv), g_f / 2π should not be smaller than the operating frequency of the PMLM system. Otherwise, the LPF will distort the useful information in I_sK_{fn}-M_nsv. In other words, the g_f /2π should be higher than the operating frequency of the PMLM system.

3) Since the LPF is inserted into the observer and compensator, the model of compensated PMLM will become the system shown in (7.5). The term 1-*F(s)* in these two equations is a high-pass filter and only high frequency components of F_{cmp} can perturb the outputs of the PMLM. g_f/2π should be slightly higher than all the dominant components of F_{cmp}.

4) Another restriction of g_f is caused by the "power amplifier" of the PMLM. Under the current control mode, there is a current feedback loop inside the power amplifier and the current loop will have its own cutoff frequency. The g_f/2π should be smaller than this cutoff frequency.

The LPF implemented in this project is a third order critical damping low pass filter as shown in (7.6).

$$F(s) = \left(\frac{1}{\frac{1}{g_f}s + 1}\right)^3 \tag{7.6}$$

It is expected that the noise amplitudes of F_{cmp} are very large and the third order filter can provide a higher ability of noise suppression. Although there are many different forms of third order LPF, the author prefers using the above structure in order to simplify the process of modifying g_f during experiments. In this project, the possible range of g_f is quite wide and the critical value must be determined experimentally.

7.2 Internal model reference control

High precision linear motion control usually requires the output of the system tracking with the specific trajectory and requirements, such as small rising time and critical damping ratio. The objective of IMRC is to design a differentiator-free controller so that the output of the plant can asymptotically follow the output of stable reference model. This algorithm provides a simple controller design process. The engineers require identifying the precise plant model and designing the stable reference model only. It is also a simple and quick method for achieving high precision motion control in industrial application if the controller is integrated with a disturbance compensator.

7.2.1 IMRC algorithm explanation

The block diagram of IMRC is drawn in Fig.7-4 and the relevance equations are derived in (7.7).

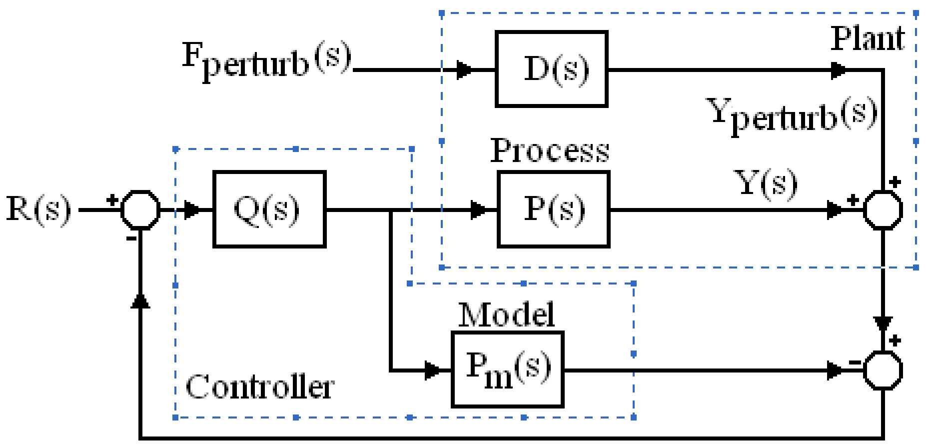

Fig.7-4 Internal model control algorithm

$$(R(s)-Y(s))(\frac{Q(s)}{1-P_m(s)Q(s)})P(s)+Y_{perturb}=Y(s)$$
$$R(s)(\frac{P(s)Q(s)}{1-P_m(s)Q(s)})+Y_{perturb}=(\frac{P(s)Q(s)}{1-P_m(s)Q(s)})Y(s)$$
$$Y(s)=R(s)(\frac{P(s)Q(s)}{1-P_m(s)Q(s)+P(s)Q(s)})+Y_{perturb}(\frac{1-P_m(s)Q(s)}{1-P_m(s)Q(s)+P(s)Q(s)}) \quad (7.7)$$

where *P(s)* is actual process

Q(s) is the transfer function inside the controller

$P_m(s)$ is the model of the process

D(s) is the transfer function which converts the external disturbance and perturbation into the output of process

R(s) is the command input

Y(s) is the system output

$Y_{perturb}(s)$ is the disturbance to system output

If the model of the system and the actual process are identical, (7.7) will be further simplified as below:

$$Y(s)=R(s)P(s)Q(s)+Y_{perturb}(1-P_m(s)Q(s)) \quad (7.8)$$

Consider the system is disturbance-free PMLM and $Y_{perturb}$ should be zero, the output of system can be simply determined by the functions *R(s), P(s),* and *Q(s)*. *Q(s)* in (7.8) is a designable function and therefore it can be designed to be *M(s)/P(s)*, where *M(s)* is the stable reference model with order equal to or higher than *P(s)*. Overall, the system can be simplified as (7.9). Note that the characteristics of the original plant are completely eliminated.

$$Y(s)=R(s)M(s) \quad (7.9)$$

Note that the control algorithm is also called “model reference control” [53]. It requests that the plant *P(s)* should be minimum phase. This requirement is necessary for ensuring the internal stability. It also ensures the model reference control objective, which is cancellation of the plant zeros.

7.2.2 Application to disturbance-free PMLM

In order to achieve the IMRC output given in (7.9), two requirements have to be fulfilled.

1) the model of PMLM have to be precise so that the difference between the plant and the model is very small, and
2) the disturbance of the system should be zero

Without the assistance of disturbance compensation, achieving both requirements is not an easy task. For a pure PMLM, non-linear disturbances including force ripple, friction, and load variation induce the difference between the actual motor model and the constructed model. The compensator will reject disturbances and perturbations if the cutoff frequency of LPF g_f is selected properly. In addition, the presence of the compensator can modify the PMLM to be a disturbance-free PMLM with the model as shown in (7.4). The condition of $P(s)=P_m(s)$ can therefore be achieved.

Referring the compensated PMLM system, the effect of external disturbance is suppressed so the corresponding $Y_{perturb}$ in this system can be equal to zero. The IMRC approach mentioned in the previous section can be directly applied to the PMLM to form the high precision motion control. In this section, a cascaded structure controller with the position and velocity feedback is introduced so that the velocity loop and the position loop can be modified independently.

The controller of velocity loop can be constructed as shown in Fig.7-5 (a). $P_v(s)$ stands for the compensated PMLM with a current command input I_{cmd} and a velocity output. The model of process is shown in (7.2) because the disturbances are completely eliminated. It is restated as follows:

$$P_{mv}(s) = \frac{\dot{X}}{I_{cmd}} = \frac{K_{fn}}{M_n s} \tag{7.10}$$

The stable model reference and controller for the velocity loop are designed as

$$M_v(s) = \frac{1}{\frac{1}{g_v}s + 1} \tag{7.11}$$

$$Q_v(s) = \frac{M_n s}{K_{fn}} \frac{1}{\frac{1}{g_v}s + 1} \tag{7.12}$$

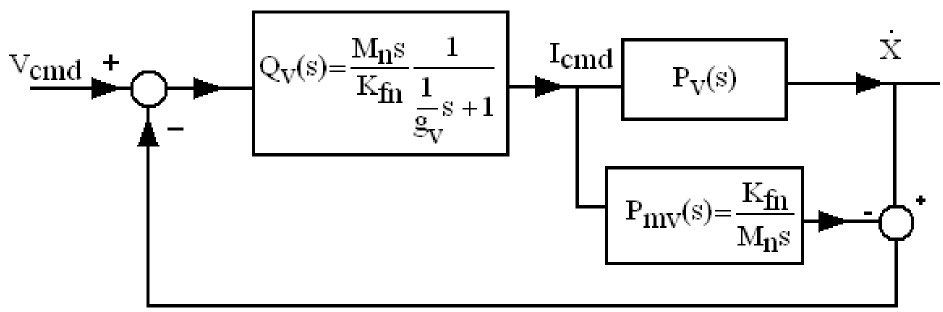

(a)

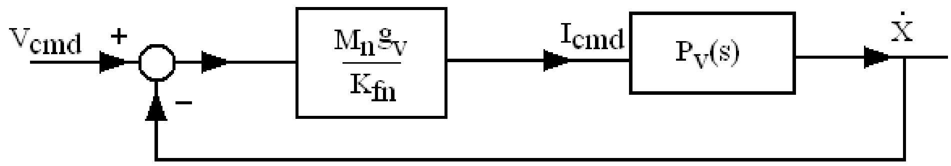

(b)

Fig.7-5(a) Velocity loop with internal model control algorithm; and (b) Simplified velocity loop controller.

Note that the stable reference model $M_v(s)$ chosen in this controller is a first order system with low pass filter characteristic. The dynamic performance can be adjusted by varying the parameter g_v in $Q_v(s)$. The cutoff frequency $g_v / 2\pi$ must be smaller than the cutoff frequency of LPF in the disturbance observer and compensator $g_f / 2\pi$. The velocity control loop can be simplified into a single feedback controller and the modified loop is shown in Fig.7-5 (b). After the IMRC is applied, the transfer function of the controlled velocity loop is shown in (7.13).

$$\frac{\dot{X}}{V_{cmd}} = \frac{1}{\frac{1}{g_v}s + 1} \tag{7.13}$$

For the position loop, the design process is similar to that of the velocity loop. The control algorithm of the position loop is derived similarly. The input of the process is the velocity command V_{cmd} and the output of the controlled process is the position of the PMLM x. The process of position loop $P_p(s)$ should be the controlled-velocity system multiplying an integrator. The position control loop is constructed as shown in Fig.7-6 (a). The process can be modeled as (7.13) together with an integrator and it is shown in (7.14).

$$P_{mp}(s) = \frac{X}{X_{cmd}} = \frac{1}{s}\frac{1}{\frac{1}{g_v}s + 1} \tag{7.14}$$

The stable model reference and controller for the position loop are designed as

$$M_p(s) = \left(\frac{1}{\frac{1}{g_x}s + 1}\right)^2 \tag{7.15}$$

$$Q_p(s) = \left(\frac{1}{\frac{1}{g_x}s+1}\right)^2\left(\frac{1}{g_v}s^2 + s\right) \tag{7.16}$$

The position control loop can be simplified into a single feedback controller and the modified loop is shown in Fig.7-6 (b).

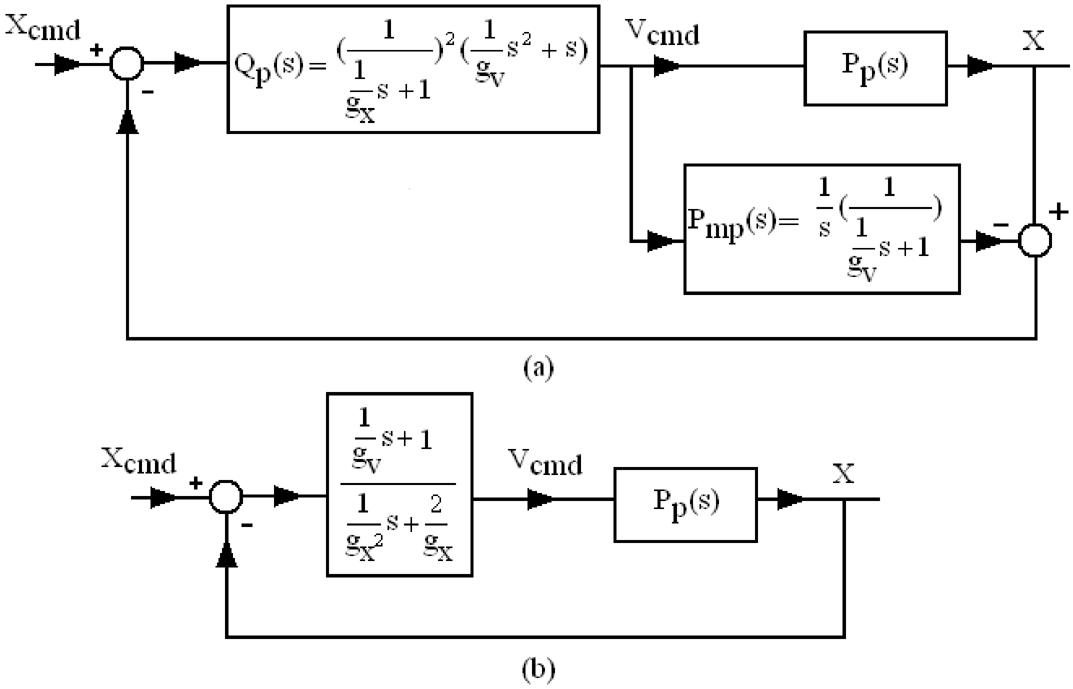

Fig.7-6(a) Position loop with internal model control algorithm, and

(b) Simplified position loop controller.

A second order critical damping model is selected as a stable reference model since oscillation in the position of translator (ringing) should be prevented during the industrial manufacturing or transportation process. The dynamic performance can be adjusted by varying the parameter g_x in the model. Note that g_x should not be higher than g_f and g_v. After the IMRC is applied, the transfer function of the controlled position loop is shown in (7.17).

$$\frac{X}{X_{cmd}} = \left(\frac{1}{\frac{1}{g_x}s+1}\right)^2 \tag{7.17}$$

If the velocity control loop and the position control loop are integrated and applied to control the compensated PMLM, the block diagram of the system can be represented as shown in Fig.7-7.

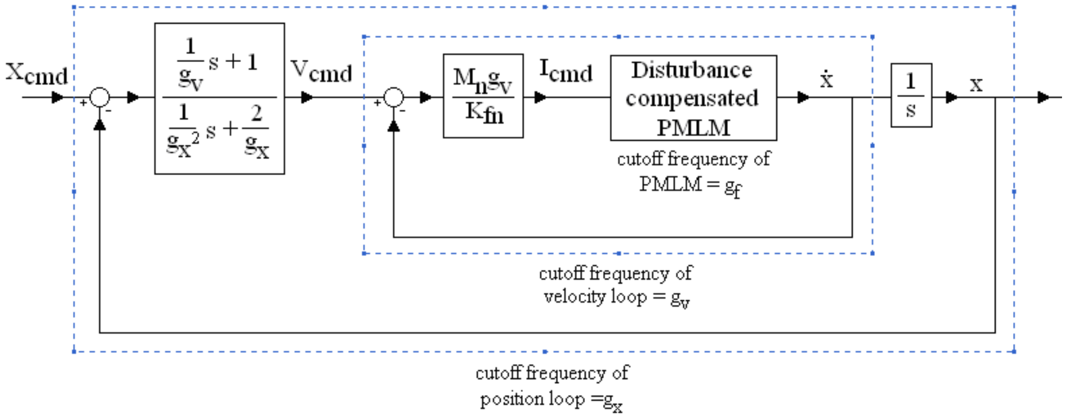

Fig.7-7 The block diagram of compensated PMLM controlled by normal IMRC, with cutoff frequencies of PMLM, velocity loop, and position loop

When the cutoff frequency of the LPF in the compensator g_f, the model in the velocity loop g_v, and the model in position loop g_x are considered, it is found that $g_f > g_v > g_x$. This relationship is established because the operation of outer loop should be slower than the inner loop [59-61]. When the cascaded-structure controllers are designed, it is suggested that the cutoff frequency of the inner loop should be three to five times larger than that of the outer loop (i.e. $g_f > 3g_v > 9g_x$). The selection of g_f has already been explained in section 7.1.3.

7.3 Novel modification for the disturbance observer and compensator

Generally, by applying the standard disturbance compensator and the IMRC algorithm, the high precision positioning control can be achieved. However, some expected problems still exist. They are:

1) The effect of static friction in the PMLM
2) The effect of the crossover between static friction and dynamic friction
3) Slow response to the external disturbance

Note that both problems will be investigated in the following section and a novel method of improvement is proposed.

7.3.1 Problems of the conventional disturbance compensator

The disturbance compensation algorithms mentioned in previous sections are the standard disturbance compensator. In fact, the high precision positioning control can be achieved effectively by using the standard algorithms only. However, the high frequency components of F_{cmp} still perturb the outputs of the "disturbance-free" PMLM. The main source of high frequency components of F_{cmp} is the presence of static friction and the crossover between static and dynamic friction. This section explains the transient disturbance and proposes a novel modification for a conventional disturbance compensator. This modification further improves the PMLM to be the ideal system in (7.4). The achievement of the high precision linear motion system can be easier.

7.3.2 Modification of the conventional disturbance compensator

Consider the original compensated PMLM, shown in (7.5), the term $[1-F(s)]\times F_{cmp}$ appears and it is the high frequency of F_{cmp}. Fortunately, the major components of F_{cmp} are usually at low frequency and they can be compensated. However, the transient disturbances, which are high frequency components, will still affect the outputs of the PMLM. Examples of transient disturbances are the sudden external impact, the effect of static friction and the effect of crossover between static and dynamic friction. A novel modification, inserting an additional extra gain K_i, is applied to the conventional disturbance compensator. The modified compensation block diagram can be modified as shown in Fig.7-8. Consider the compensated PMLM with K_i, the equations of the plant can be derived as shown in (7.18).

$$I_s K_i (K_{fn} + \Delta K_f) + F_{dis} = (M_n s + \Delta M s)v + Dv \tag{7.18}$$

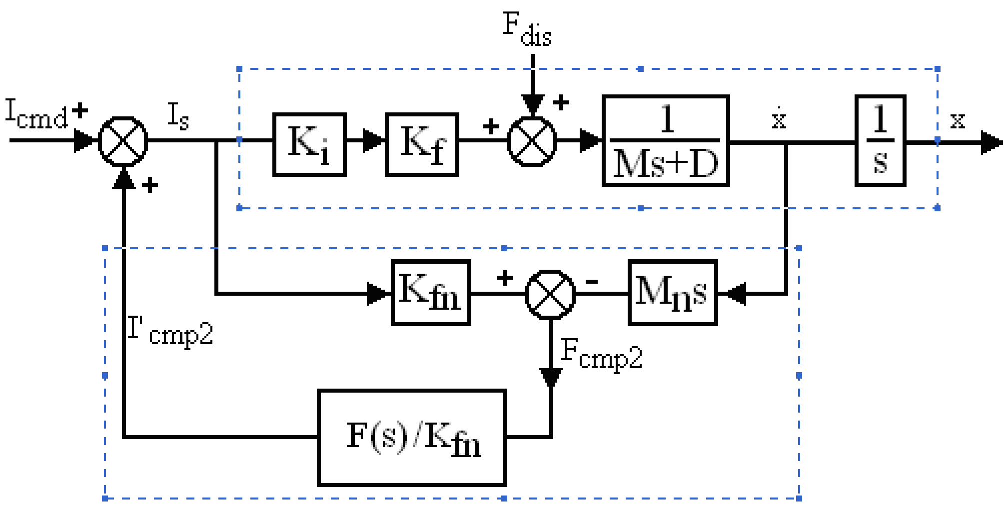

Fig.7-8. Modified disturbance compensator for PMLM

This PMLM with K_i can be rearranged as shown in (7.19) and those perturbations appearing in this PMLM are grouped and named as F_{cmp2}:

$$I_s K_{fn} - M_n sv = F_{cmp2} = \\ \Delta M sv + Dv - F_{dis} - I_s K_i \Delta K_f - I_s K_{fn}(K_i - 1) \tag{7.19}$$

If this F_{cmp2} is converted to a compensation current I'_{cmp2} and fed-back to the PMLM, the equations of the compensated system can be rearranged and they are shown in (7.20).

$$I_{cmd} K_{fn} - M_n sv = [1 - F(s)] F_{cmp2} \tag{7.20}$$

7.3.3 Advantage of the modified disturbance observer compensator

(7.20) can be rearranged into another two structures shown in (7.21) and (7.22). They can be used for explaining the properties of the new disturbance compensated system.

$$I_{cmd} K_{fn} - M_n sv = [1 - F(s)][F_{cmp} - I_s K_f (K_i - 1)] \tag{7.21}$$

$$I_{cmd} K_{fn} - M_n sv = \\ (\Delta M sv + Dv - F_{dis} - I_s \Delta K_f K_i)[1 - K_i F(s)] - \\ I_{cmd} K_{fn}(K_i - 1)[1 - K_i F(s)] + I'_{cmp2} K_{fn}(K_i - 1) F(s) \tag{7.22}$$

The format of (7.20) is same as that of (7.5). This means that the modified system in (7.20) can also reject the external disturbance force, kinetic friction, and parameter variation.

The merits of the modified compensator can be observed from (7.21). The equation (7.21) is rearranged for comparing with (7.5). An additional term $[1-F(s)]\times[I_sK_f(K_i-1)]$ has appeared in (7.21). Since the term $1-F(s)$ has a high pass filtering characteristic, this additional term can calculate the high frequency components of I_s. Note that I_s is composed of the input current command (I_{cmd}) and the compensation current for F_{cmp2} (I'_{cmp2}). In other words, when the command or measured disturbance changes suddenly, the high frequency components of I_s will be larger and extra efforts will be added to the PMLM. The modified systems will respond to the high frequency disturbances, such as impulse disturbance, faster than the conventional compensation system because of the presence of I'_{cmp2}. Also, the modified systems will respond to the current command I_{cmd} faster because I_s includes I_{cmd}. To conclude, the gain K_i will amplify the high frequency components of I_{cmd} and produce the additional effort to drive the PMLM to command inputs

Inserting K_i can reduce the adverse effect of static friction and that of the crossover between static and dynamic friction. Consider the <u>conventional compensation method</u> shown in Fig.7-2, when the velocity of the PMLM is crossing zero (the translator reverses its direction or starts moving from rest), the motor remains stationary (velocity remains zero) even the current is injected to the motor. This phenomenon is because of the presence of static friction. Since there is a difference between the expected thrust force (I_sK_{fn}) and the actual thrust force ($M_nsv=0$), F_{cmp} will rise quickly and the effect of static friction will be reflected in I'_{cmp}. This I'_{cmp} is fed-back to the translator and eliminates the effect of static friction after a short period of time. Note that the effect of static friction is like a transient force stopping the motor and it is a kind of high frequency disturbance. Now, referring <u>the proposed new compensated PMLM</u> in (7.21), $[1-F(s)]\times[I_sK_f(K_i-1)]$ can provide an extra effort to eliminate the static friction because I_s contains I'_{cmp2}. The time for eliminating the static friction is shorter than that of the PMLM with a conventional disturbance compensator.

Inserting K_i is a possible suggestion for reducing the transient effect of disturbance and command, but it will also cause some adverse effects to the output of PMLM if K_i is not chosen carefully. The term $[1-F(s)]\times[I_sK_f(K_i-1)]$ contains a high pass filter $1-F(s)$ and it does not only pass the high frequency components of I_s, but also allows the noise in F_{cmp2} to perturb to the PMLM. The level of noise will be amplified and this causes oscillation and audible noise if K_i is too large.

(7.22) is another form of the new compensated PMLM. It can be utilized to determine the maximum and minimum value of K_i. The right hand side of this equation consists of three terms. The first term is related to the effect of parameter variation, kinetic friction, and F_{dis}. The second term is related to I_{cmd}, and the final term is related to I'_{cmp2}. In this equation, there is a variable filter ($1-K_iF(s)$) with a special characteristic. Bode-plot with different K_i is obtained as shown in Fig.7-9. Note that the function $\Delta Msv+Dv-F_{dis}-I_s\Delta K_fK_i$ is always linear because all parameters in this equation continuous. F_{dis} in this equation includes the external disturbance, the static friction and the effect of the crossover between static and dynamic friction. Although the static friction is non-linear function, it appears like an impulse response from the point of view of time domain. F_{dis} is therefore counted as linear function. The effect of ($1-K_iF(s)$) will be additive to $\Delta Msv+Dv-F_{dis}-I_s\Delta K_fK_i$. When K_i is smaller than two, this filter has the high-pass filtering characteristics. When K_i is equal to or larger than two, the filter will amplify the signal instead of suppressing the signal because its magnitude is always larger than 0dB. The first term in (7.22) is expected to be suppressed, so K_i should not be larger than two. Meanwhile, if K_i is smaller than one, the response rate of the plant will be deteriorated. Note that the second and third term are the high-pass-filtered I_{cmd} and exceeding I'_{cmp2}. These two currents provide extra efforts to improve the dynamic response of the PMLM.

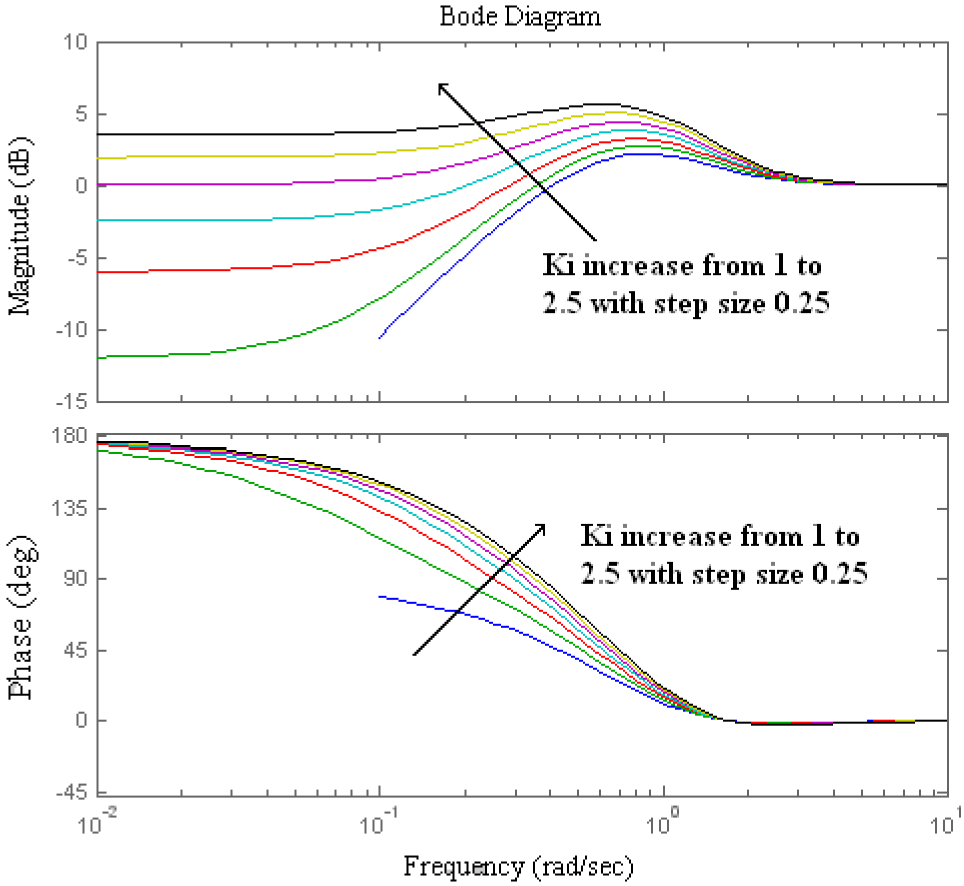

Fig.7-9. Bode plot of transfer function of $1\text{-}K_iF(s)$ with different K_i

For the practical situation, the effect of high frequency disturbance will dominate when the translator is near the targeted position and travels at low speed. Hence, the proposed additional gain K_i is designed with the considerations shown below:

1) When the position error is small and the translator is slow, K_i is selected to be two.

2) For other cases, the motor is operating at normal condition and K_i is selected to be one.

However, the profile of K_i should be determined by experiments and it will be discussed later.

7.3.4 Stability of the Controlled PMLM with IMRC

Consider the entire system of new compensated PMLM with IMRC controllers, the position output equation can be derived as shown in (7.23) and (7.24)

$$X = X_{cmd}\frac{1}{\left(\frac{1}{g_x}s+1\right)^2} - F_{cmp2}\left[\frac{\left[\left(\frac{1}{g_f}s+1\right)^3-1\right]\left(\frac{1}{g_x{}^2}s+\frac{2}{g_x}\right)}{\left(\frac{1}{g_f}s+1\right)^3\left(M_n s+M_n g_v\right)\left(\frac{1}{g_x}s+1\right)^2}\right] \tag{7.23}$$

$$X = X_{cmd}H_1(s) - F_{cmp2}H_2(s) \tag{7.24}$$

The stability of (7.24) can be ensured by studying the locations of poles of H1(s) and H2(s). All the poles of H1(s) and H2(s) appear at the left hand side of the s-plane. The linear motion system controlled by IMRC is, therefore, a stable system. Note that Fcmp2 is bounded and it will shown by experiment. Regarding to the effect of Ki on the stability of outputs, as mentioned in Section 7.3.3 and (7.22), if Ki is smaller than two, the disturbances will not be amplified and Fcmp2 will also remain bounded. Overall, the system outputs will be stable if Ki is not larger than two.

7.4 Implementation and practical selection for controller parameters

To illustrate the feasibility of the proposed high precision linear motion control algorithm, the equipments shown in Table 7-1 were utilized to construct a linear motion system. During the experiments, all parameters in the proposed idea were obtained and optimized based on the experimental results.

Name of equipment	Company	Model	Other specification
Permanent magnet linear motor	Copley Control Corporation	SM1104	Servotube Module with embedded hall effect motion sensor
Servo driver		ADP-090-09-S	Digital servo drive 1) with current cutoff frequency = 3.2 kHz 2) with current output limitation = 3A
Digital Signal Processor Board	dSPACE	DS1104 R&D controller board	Sampling time = 0.00005s
Linear optical incremental encoder	Renishaw	RGH24H30D30A	Resolution of 50nm

Table 7-1 Specifications and model of experiment equipments for controller parameters selection

7.4.1 Overview of the implementation

In order to investigate the actual performance of proposed control method and algorithm, the experimental setup shown in Fig.7-1 was connected. The linear motor used in this project was a PMLM which was driven by a servo driver. The position sensor installed on the actuator was a linear incremental optical encoder. The terminals of the optical linear incremental encoder and the current input terminal in amplifier were connected to a DSP. This powerful DSP allows the user to input the control algorithms through the simulink of MATLAB. The algorithms in time-continuous format (in s-domain) were transformed to the program code and uploaded to the real-time processor inside the DSP. During the experiment, the results and data can be stored by the DSP and plotted out for the presentation. Note that the maximum current from the amplifier is 3A and the maximum measurable speed of the encoder is $0.35ms^{-1}$.

The new proposed disturbance compensator is based on the conventional disturbance compensator, so the first step of experiment was to develop a compensated PMLM as shown in (7.5). g_f was determined and optimized experimentally. The IMRC control algorithms for the velocity loop and the position loop were implemented. The performances of this compensated and controlled PMLM were studied. The results were recorded for the comparison with the new proposed method. With the help of IMRC, the position and the velocity of the PMLM can be controlled. The effects of K_i on the PMLM were investigated. The PMLM was driven with different command inputs and different K_i. The performances of the new proposed system were studied. The shape of K_i was then determined based on these results. With the optimized profile of K_i, the new proposed method was implemented. The performances of compensated PMLM with the new method were also investigated and the results were studied. Note that the experiment works are in micro precision. Any vibrations or wind can affect the experimental results easily.

7.4.2 Disturbance measurement

Many textbooks and engineers have already discussed and pinpointed the major difficulties when the PMLM is utilized to develop the precision linear motion system. The difficulties include variations in parameters of motor, load disturbances, unexpected external disturbance forces, the friction, and the ripple force. Instead of handling the difficulties one by one, they are estimated and compensated by a single process in this project.

An experiment to observe the disturbance acting on the PMLM at different positions was conducted. The disturbances acting on the translator of the PMLM were measured while the translator was commanded to travel forward and backward slowly. This experiment was repeated with two different velocities. The estimated disturbances are shown in Fig.7-10. The disturbance was very complicated and not easy to be decomposed. Also, if the traveling speed of the motor is adjusted, the curve of disturbance will change accordingly. Note that the measured disturbances are given by a lower curve and an upper curve. They were obtained when the motor traveled in positive direction and the negative direction respectively.

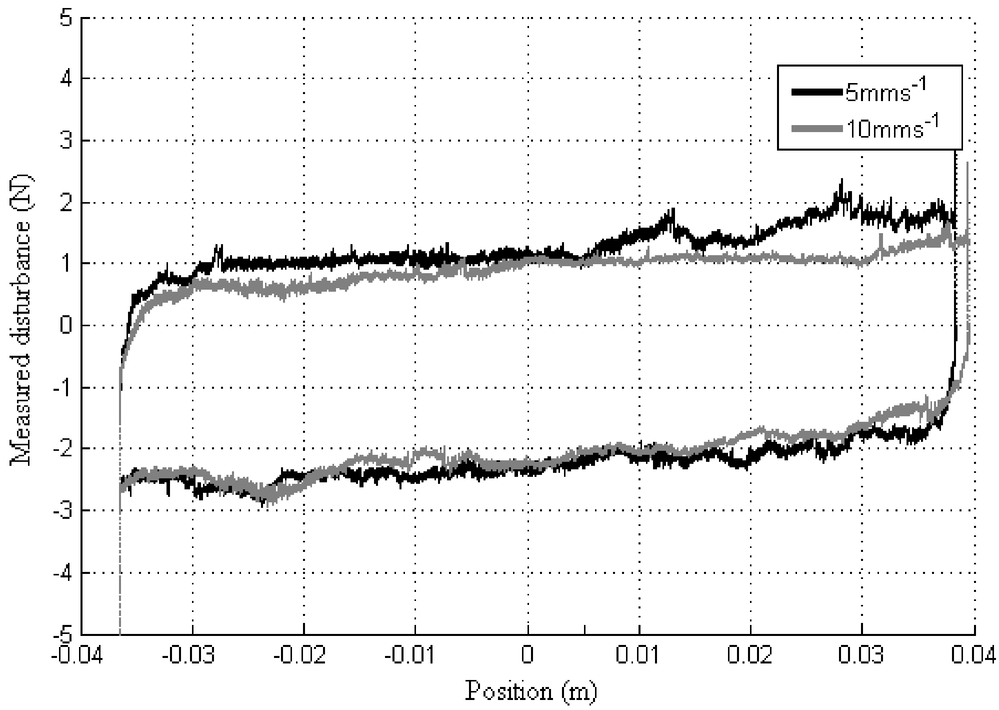

Fig.7-10 Measured disturbance of non-compensated PMLM

7.4.3 Construction of conventional disturbance observer and g_f optimization

The "disturbance observer and compensator" shown in Fig.7-2 was constructed. Referring the original disturbance compensation algorithm, there is one parameter, g_f, which needed to be determined. The constraints in section 7.1.3 are investigated.

1) The minimum amplitude of noise in F_{cmp} can be roughly deduced from the resolution of the optical incremental encoder. The resolution of the acceleration measurement is 20ms^{-2}. Based on (3), $F_{cmp} = (I_{cmd}+I'_{cmp})K_{fn}-M_n sv$, the minimum deviation in F'_{cmp} will be $M_n \times 20$ = 9N. The deviation in non-filtered compensated current F'_{cmp}/K_{fn}, is 9/4.1 = 2.195A. If this current deviation is injected to the PMLM, the audible noise and the high frequency oscillation in the position of PMLM will appear. The frequency of this noise can be calculated by $f_{sampling}/\pi$. The cutoff frequency $g_f/2\pi$ should be smaller than this value.

2) The operation frequency of the positioning system was designed to be 25Hz. It is the general operation frequency in many industrial applications. $g_f/2\pi$ should be much greater than 25Hz.

3) Based on the measurement of disturbance shown in Fig.7-10, the disturbances and perturbations are related to the position and the velocity. This means that the frequency of F_{cmp} or F_{cmp2} is also related to the operating frequency of the system. Therefore, $g_f/2\pi$ should be much greater than 25Hz.

4) The cutoff frequency of the current driver of PMLM is 3.2 kHz. The maximum value of g_f will be $2\pi\times3200$. However, g_f should be much smaller than $2\pi\times3200$ because the LPF has to suppress the noise in estimated F_{cmp}.

The possible range for g_f is also wide. In order to optimize g_f and achieve the high speed compensation and the noise suppression, the performances of disturbance compensators with different g_f were investigated through experiments.

The square wave current commands (with different amplitudes ranged from 0.1A to 0.35A, with period equal to 0.4s) were inputted to the disturbance compensated PMLM. The waveforms of compensated currents I'_{cmp} were recorded. The times of rejecting static friction were obtained and the r.m.s. values of the noise in I'_{cmp} were also recorded. The above experiments were repeated with different g_f. During the experiment, when g_f was larger than $2\times\pi\times450$, the PMLM generated the audible noise and this value was treated as the maximum limitation of the g_f. The relationship between g_f, rejecting time, and r.m.s. value of noise were studied and their plots are shown in Fig.7-11 and Fig.7-12.

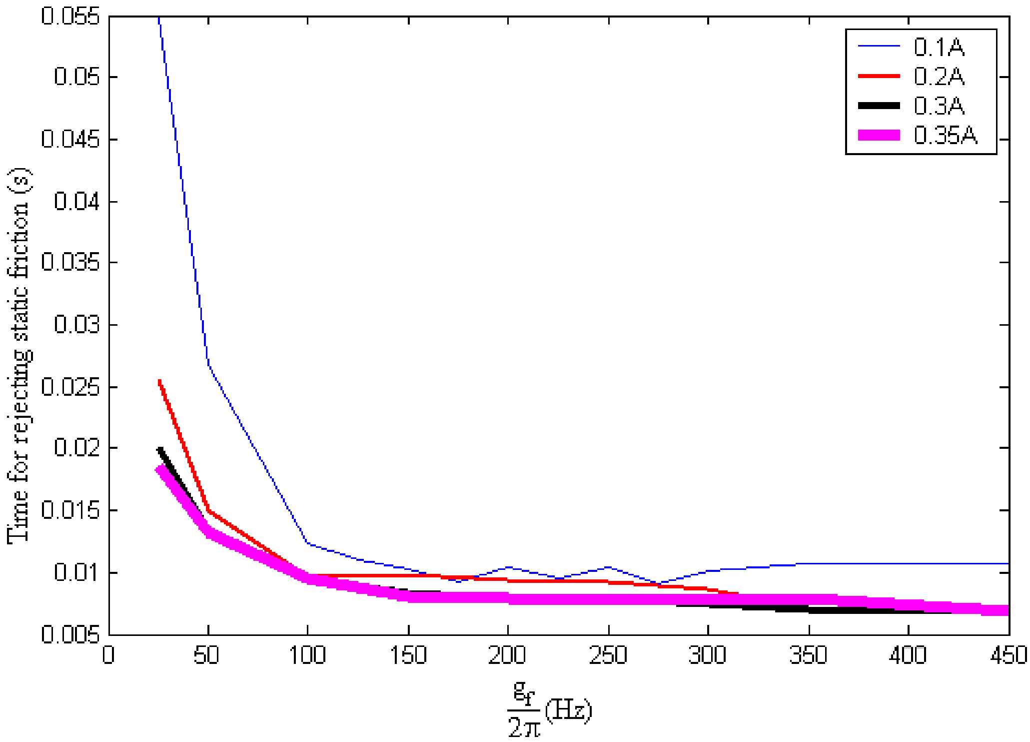

Fig.7-11. Time to override static friction vs. g_f

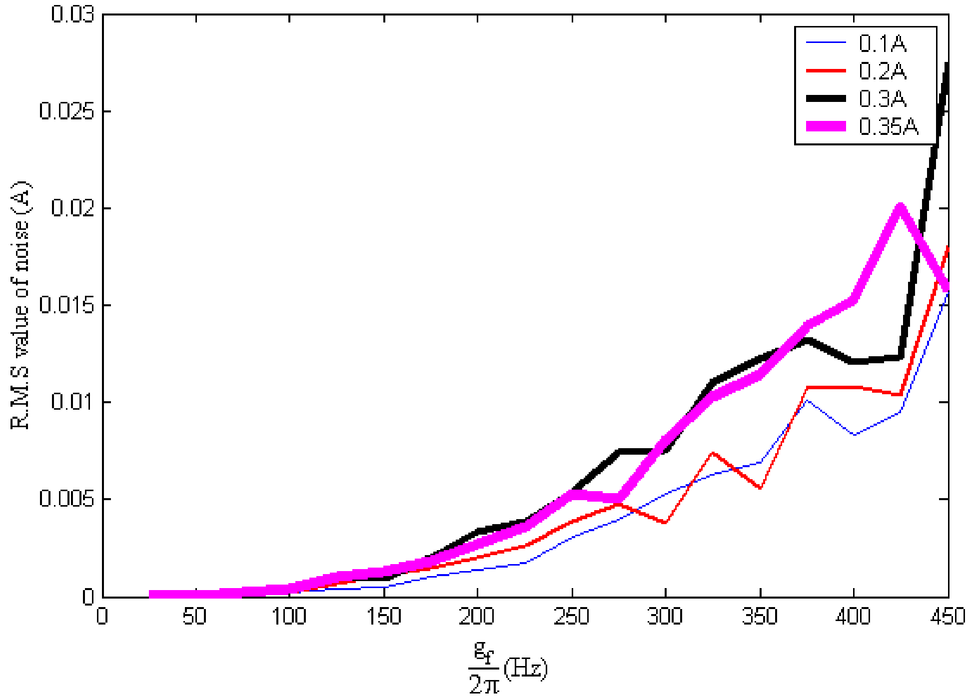

Fig.7-12. R.M.S. value of noise in I'_{cmp} vs. g_f

It is obvious that the times of eliminating static friction generally decreases with the g_f while the r.m.s. values of noise increases with g_f. There should be a trade-off point optimizing the performance of the disturbance compensator. Regarding the times of rejecting the static friction, larger g_f can reduce the time. However, the effect of time reduction is not significant when g_f is larger than 2×π×150. The minimum value of g_f should be 2×π×150. Consider another plot related to the noise of I'_{cmp}, g_f has to be kept at a small value in order to minimize the noise level. No specific indication in this plot can define the maximum value of g_f.

Another condition can help to determine the value of g_f. Based on common practice, the cutoff frequency of inner loop should be at least three times larger than that of the outer loop. The ratios between the g_f, g_v and g_x (cutoff frequency of different controlled loops) have to satisfy the following relationship:

$$g_f > 3\times g_v > 9\times g_x \tag{7.25}$$

Since the expected operating frequency of a PMLM system is 25Hz, g_x should be 2×π×25. In this thesis, g_f is chosen to be 2×π×250.

To further investigate the performance of the disturbance compensator with g_f = 2π×250, an experiment was performed with a square wave current command (amplitude equal to 0.1A). The experimental results are shown in Fig.7-13. Based on the I_{cmd}-time, velocity-time, and acceleration-time graph, the function of disturbance compensator is achieved. The results agree with the ideal model shown in (7.4) except when the velocity is nearly to zero. This difference is due to the presence of static friction. At that moment, the disturbance compensator has detected the static friction. I'_{cmp} will increase or decrease with a short period of time, which aims to reject this static friction. This response time causes the difference between the ideal model shown in (7.4) and the actual compensated motor. Consider Fig.7-13, the value of acceleration drops when the speed is around zero. This phenomenon is also caused by the static friction. Note that the acceleration shown in Fig.7-13 is filtered acceleration since the original noise of calculated acceleration is too large and meaningless in the presentation.

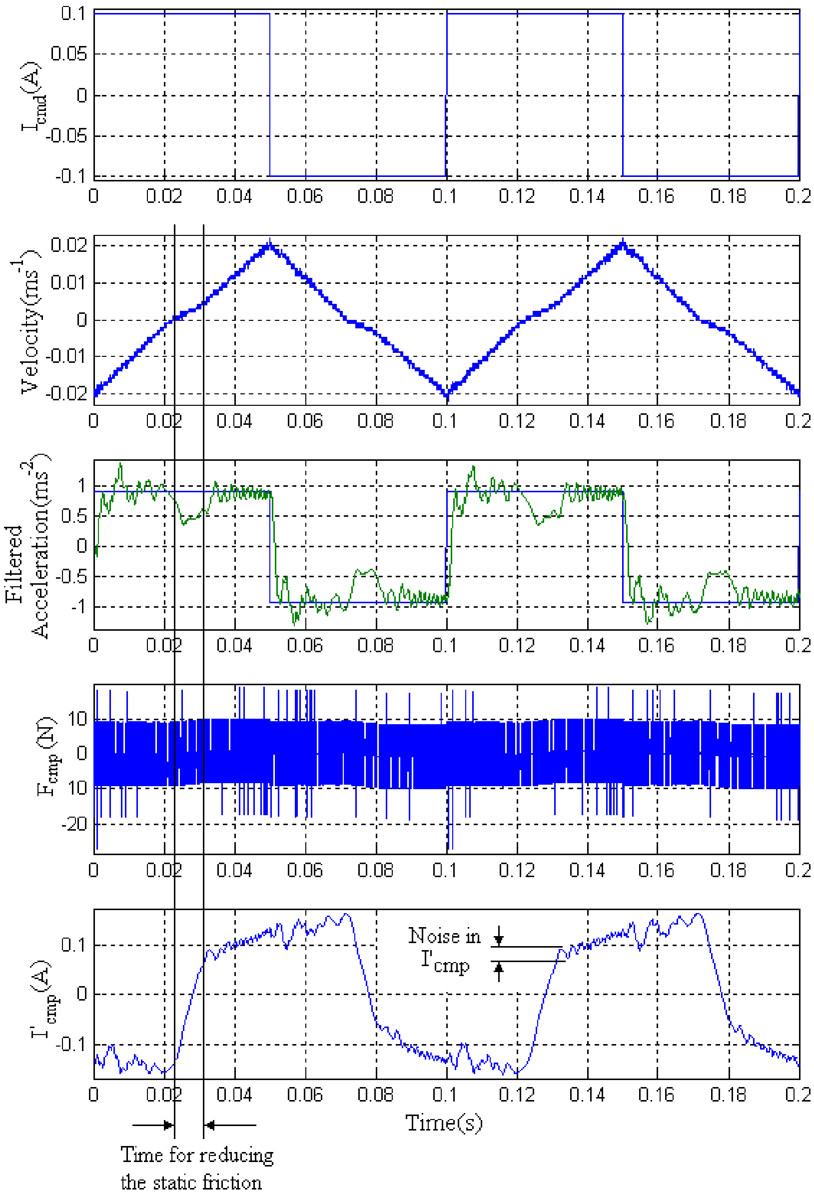

Fig. 7-13 Experimental results for performance of disturbance compensator with 0.1A step input amplitude

Another observation is related to the performance of the filter, $F(s)$. The noise in I'_{cmp} will be very high if there is absence of $F(s)$. This can be observed in F_{cmp}. The presence of a third order LPF can greatly reduce the noise amplitude to 0.01A to 0.02A and provide the effective disturbance compensation.

7.4.4 High precision linear motion controlled system by conventional disturbance compensator and IMRC

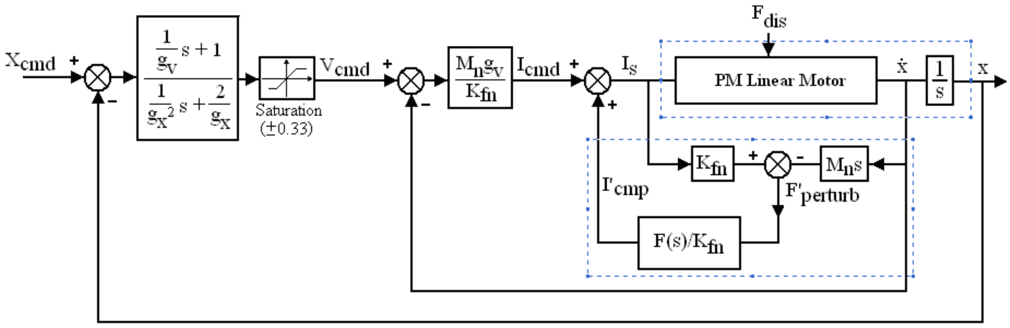

Fig.7-14 Experimental setup for PMLM with standard IMRC

The IMRC controllers shown in Fig.7-14 are implemented. Since g_f is selected as 2×π×250, the value of g_v and g_x can be defined as 2×π×80 and 2×π×25 respectively. With these two parameters, the IMRC controllers with cascaded structure were constructed. Three experiments of step responses (with minimum step, critical condition step, and large step) were performed. Their experimental results are illustrated in Fig.7-15, Fig.7-16, and Fig.7-17. The minimum step means that the step amplitude is one deviation of the position steady error (equal to 100nm). The critical condition step refers to the current or the velocity of PMLM near saturation or reaching the maximum value. For the case of large step, the current and the velocity of the motor are limited at their maximum values by the saturation functions inside the feedback loop. Another experiment called disturbance impulse response illustrating the response time on external disturbance was also performed and the results are shown in Fig.7-18.

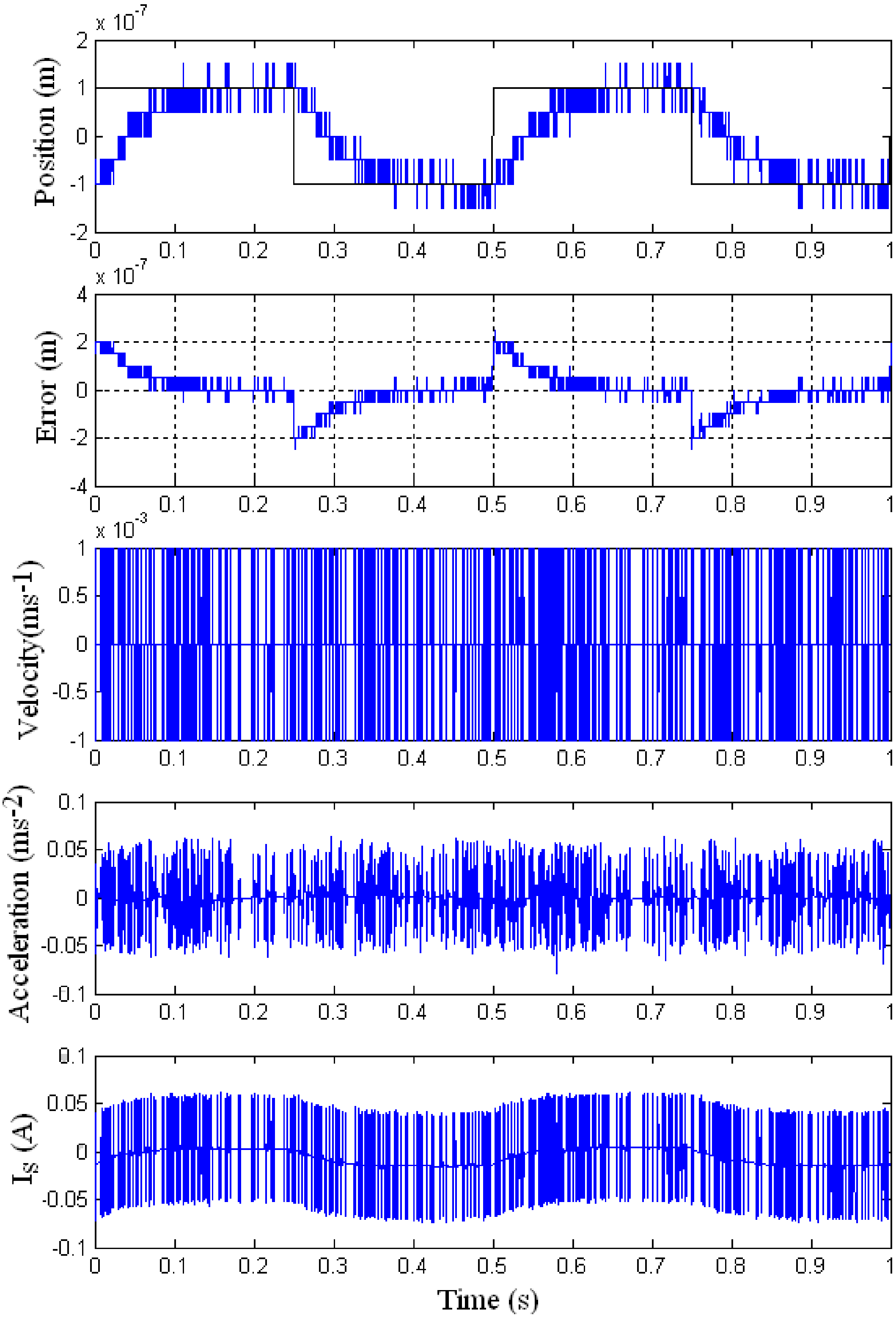

Fig. 7-15 Experimental results of controlled PMLM by standard IMRC algorithm

(small step, with amplitude of square wave = 100nm)

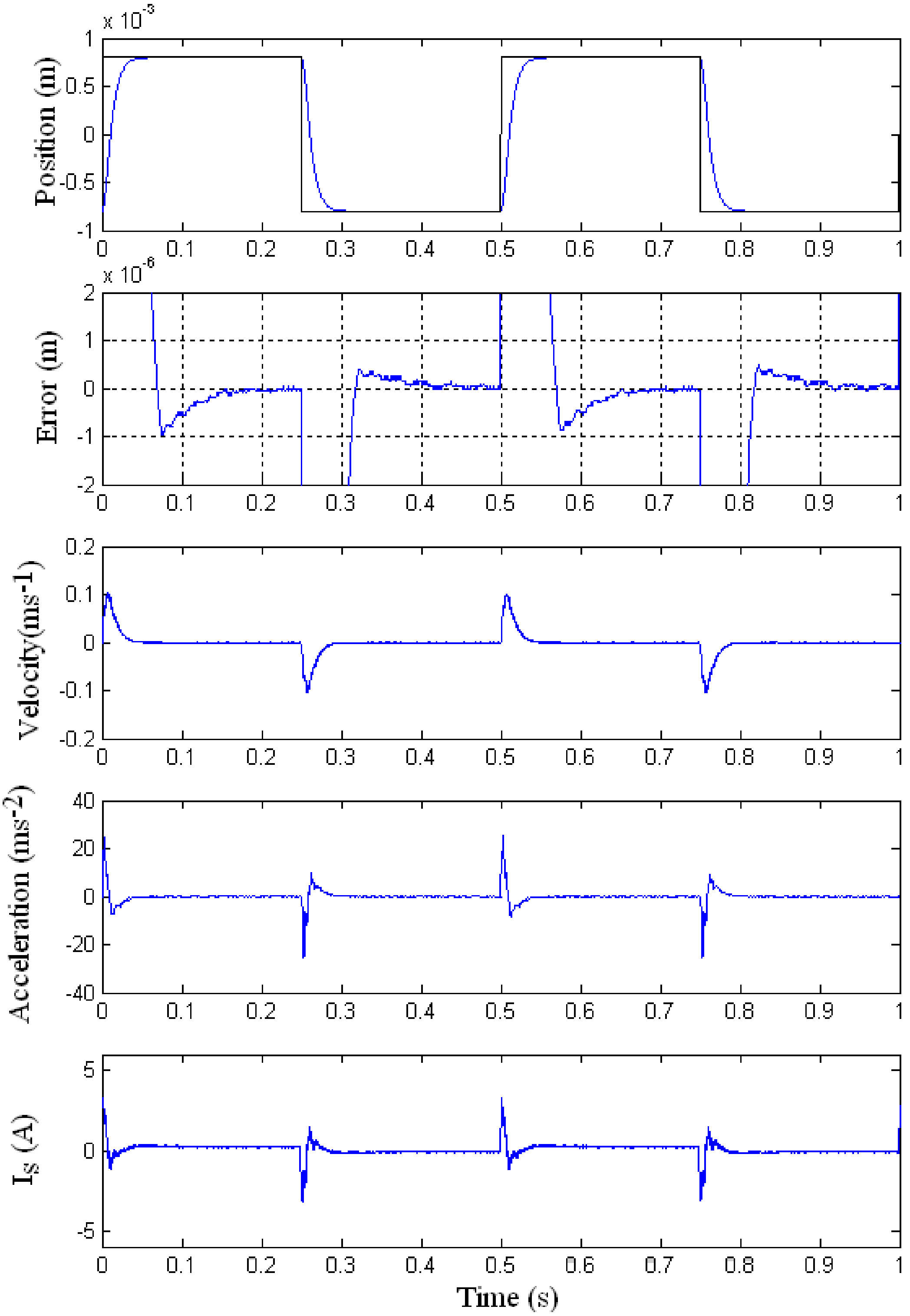

Fig. 7-16 Experimental results of controlled PMLM by standard IMRC algorithm

(critical situation step, with amplitude of square wave = 800µm)

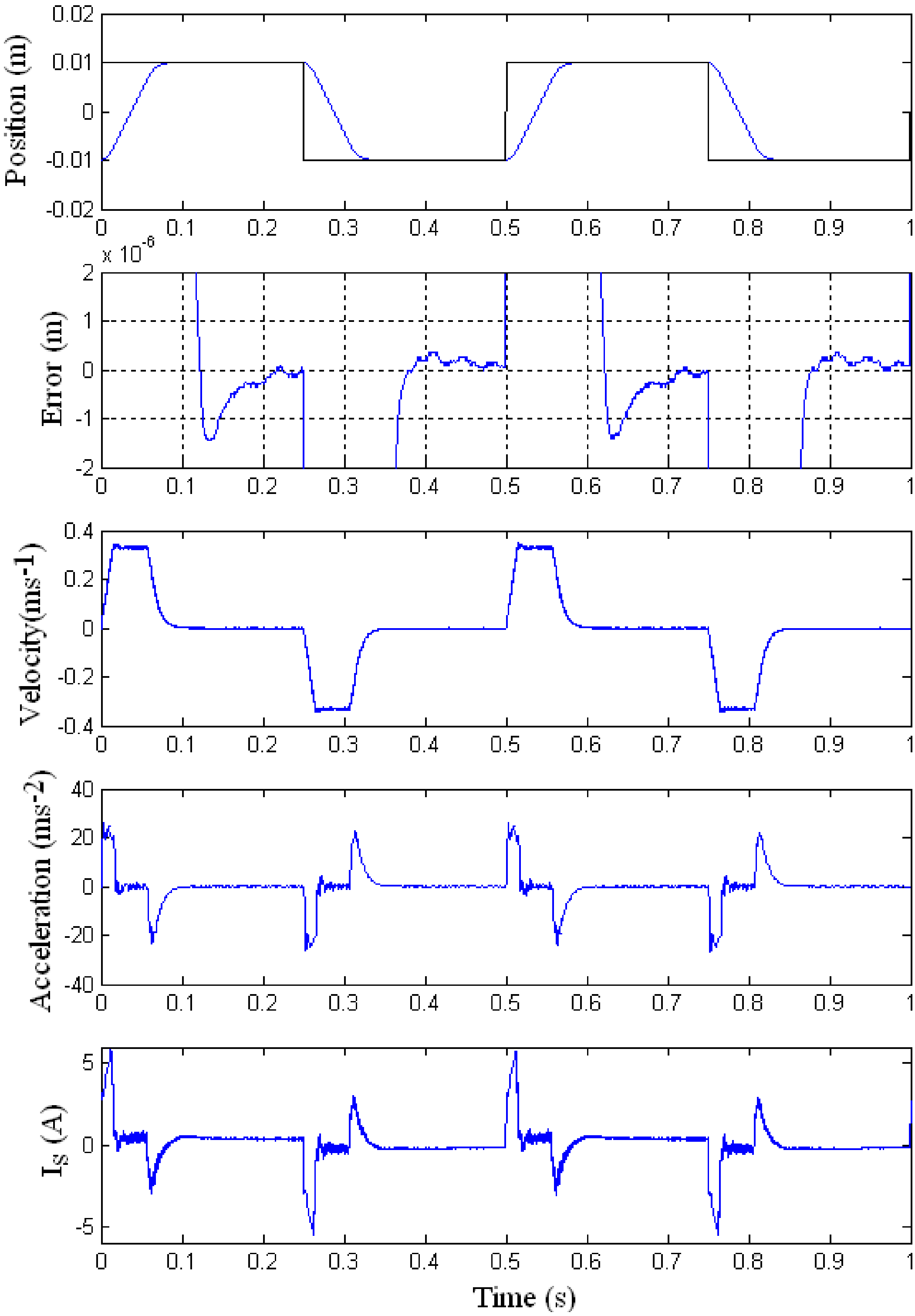

Fig. 7-17 Experimental results of controlled PMLM by standard IMRC algorithm

(large step, with amplitude of square wave = 10mm)

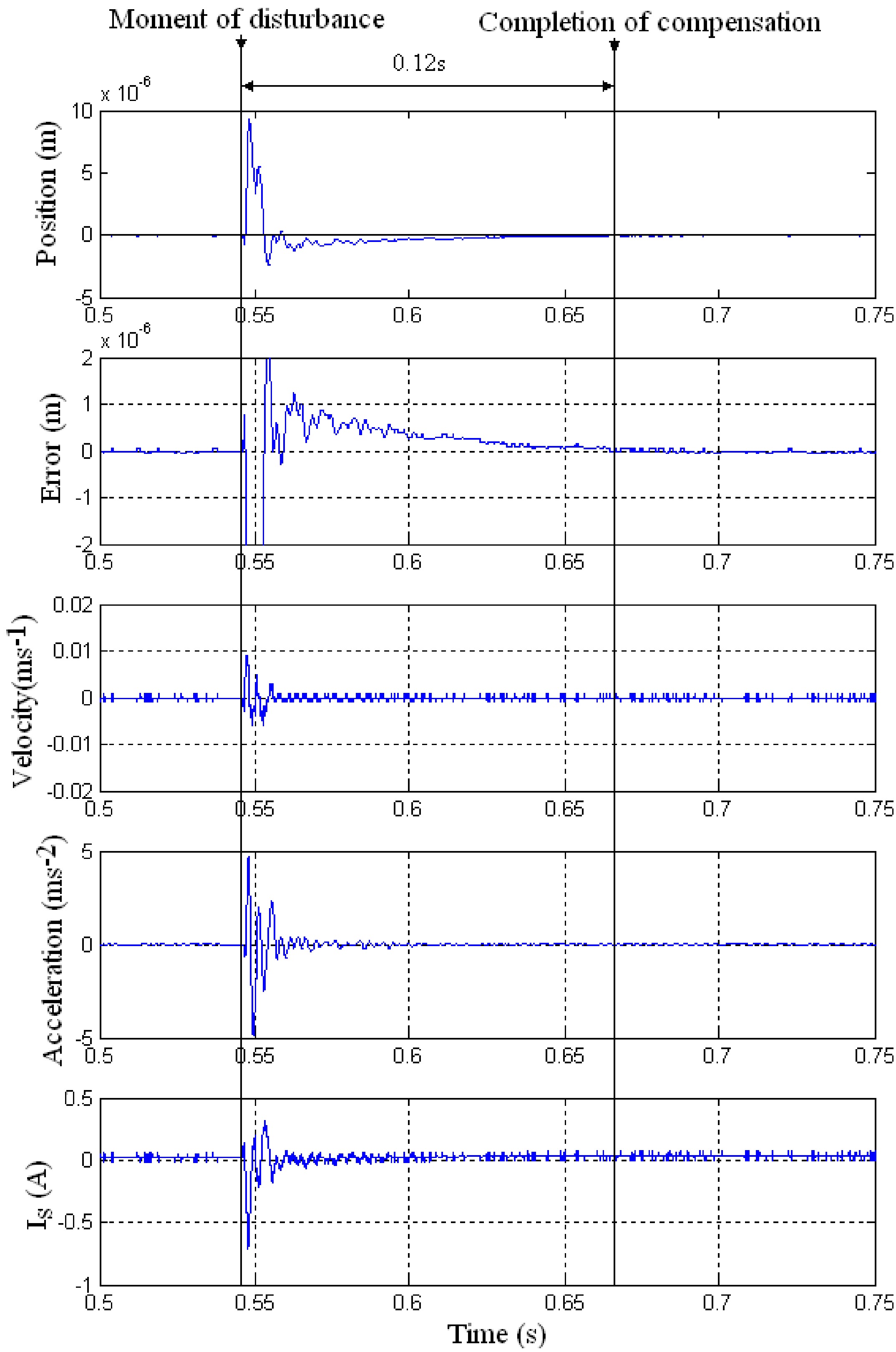

Fig. 7-18 Experimental results of controlled PMLM by standard IMRC algorithm

(with impulse contact force disturbance)

Although the compensated PMLM with IMRC algorithm can achieve the sub-micron precision linear motion system (with steady state deviation equal to 100nm), the performance of this linear motor is still not satisfactory. The major problem of the conventional method is the long rising time of the position output. The rising time of controlled position output should be 0.05s. However, the rising time of the minimum step response, shown in Fig.7-15, is 0.116s. This long rising time phenomenon is caused by the static friction and the slow response rate of the disturbance compensator.

Consider the overall control algorithm shown in Fig.7-14, when the translator is commanded to move a very small distance, the position error is very small (error is ±0.2μm, as shown in Fig.7-15). The gain of $C_p(s)$ and $C_v(s)$ should be about 63 and 55.2 respectively. The peak transient current calculated from the position error will be 0.696mA. It is a very small current and definitely too small to overcome the static friction and drive the translator to move. Although the I_{cmd} (0.696mA) is not large enough to drive the translator, the I'_{cmp} can assist the motor to overcome the static friction. If the I_s-time graph in Fig.7-15 is considered, this current contains low frequency components which are exponentially rising and falling (actually it is I'_{cmp}). This I'_{cmp} is accumulating slowly to overcome the static friction. In other words, the response time of the system is slow because of the rising time in $I_{s.}$ Note that the problem of long settling time in position output is especially serious when the position input command is too small.

Referring the experimental results of the critical step response, shown in Fig.7-16, it is obvious that the peak current is 3A and the current injected to motor reaches the limitation of power supply. Compared with the velocity of the translator, the current reaches its limit much faster. This phenomenon is because g_f is larger than g_v. The rising time shown in Fig.7-15 is smaller than that in Fig.7-16. It is because the larger I_{cmd} can provide larger effort to trigger the translator to move and overcome the static friction. This explanation can be supported by the I_s-time graph. If the step size is larger, the I_{cmd} will dominate in I_s. When the position command is changed, the I_s becomes a large value and this does not happen in the minimum step response.

Based on the information from the error-time graph in Fig. 7-16, the unexpected overshoot appears despite the fact that the critical damping model is used. The time-delay effect of LPF in the disturbance compensator possibly causes this small overshoot. The excessive and delayed compensation current develops extra thrust force in the translator and produces the small overshoot.

For the case of the large step (Fig.7-17), the current and the velocity of the PMLM are saturated. The position of the PMLM is no longer tracing the reference model as shown in (7.17). This means when the position command is larger than the critical value, 1600μm, and the controlled system is no longer an IMRC controlled system. Another observation related to I_s is shown in Fig.7-17. The peak value of this injected current I_s is larger than the limitation of the power supply (3A). However, this large current is directly injected to the servo driver. After the driver received a value larger than 3A, it will automatically limit the current output to 3A. Although the PMLM is not operated under IMRC operation, it can also achieve a sub-micron precision linear motion.

Referring the impulse disturbance response shown in Fig.7-18, the settling time is 0.12s and it is long from the industrial application's point of view. This slow response is because the disturbance compensator requires a long time to accumulate the I'_{cmp} to overcome the static friction and the cogging force.

To conclude, the original disturbance compensation system and standard IMRC system can also achieve the sub-micron precision linear motion system. The problem of this non-modified approach is that the non-linear static friction lengthens the settling time and causes a slower operating speed. Note that these results will be used for the comparison with the performance of the new proposed method.

7.4.5 Effect of K_i on high precision linear motion controlled system

Inserting K_i can improve the transient response of the position output, such as reducing the rising time and improving the response time on the disturbances. However, K_i should not be too large in order to prevent amplifying the effects of noise in I_s and the serious oscillation in the position output. Before the profile of K_i is determined, some experiments had been conducted in order to investigate the effect of K_i. The compensated PMLM controlled by IMRC is commanded to travel with different position step command. The rising time, steady state error deviation, and the overshoot level were studied. The results are summarized and shown in Table 7-2, Table 7-3, and Table 7-4.

K_i / Amplitude	1	1.5	2	2.5	3
100nm	0.116s	0.096s	0.082s	0.07s	0.06s
200nm	0.113s	0.092s	0.074s	0.067s	0.056s
500nm	0.104s	0.086s	0.072s	0.065s	0.057s
1µm	0.096s	0.081s	0.069s	0.063s	0.056s
2µm	0.076s	0.064s	0.059s	0.057s	0.056s
5µm	0.057s	0.052s	0.051s	0.05s	0.047s
10µm	0.048s	0.046s	0.046s	oscillation	oscillation
20µm	0.048s	0.05s	oscillation	oscillation	oscillation
50µm	0.056s	0.056s	oscillation	oscillation	oscillation

Table 7-2 Rising times of step responses for different amplitude inputs and K_i (time between triggering and reaching or passing through the target position)

K_i / Amplitude	1	1.5	2	2.5	3
100nm	0	0	0	0	0
200nm	0	0	0	0	0
500nm	0	0	0	0	0
1µm	50nm	50nm	50nm	50nm	50nm
2µm	100nm	100nm	100nm	50nm	50nm
5µm	200nm	150nm	150nm	100nm	100nm
10µm	250nm	200nm	200nm	oscillation	oscillation
20µm	250nm	200nm	oscillation	oscillation	oscillation
50µm	250nm	200nm	oscillation	oscillation	oscillation

Table 7-3 Overshoot of step responses for different amplitude inputs and K_i

K_i / Amplitude	1	1.5	2	2.5	3
100nm	100nm	100nm	100nm	150nm	200nm
200nm	100nm	100nm	100nm	150nm	200nm
500nm	100nm	100nm	100nm	150nm	200nm
1μm	100nm	100nm	100nm	150nm	200nm
2μm	100nm	100nm	100nm	200nm	200nm
5μm	100nm	100nm	100nm	200nm	200nm
10μm	100nm	100nm	100nm	oscillation	oscillation
20μm	100nm	100nm	oscillation	oscillation	oscillation
50μm	100nm	100nm	oscillation	oscillation	oscillation

Table 7-4 Error deviation in position for different amplitude inputs and K_i

The value of K_i can change the performances of the compensated PMLM. When K_i is increased, the rising time of the step response is reduced. This is exactly predicted as shown in Section 7.3. The additional terms $[1-F(s)]\times[I_sK_f(K_i-1)]$ in (7.21) can improve the response time by using K_i larger than one. At the same time, when the K_i is larger than two, the steady state error deviation is larger. It is because the filter $1-K_iF(s)$ acts as an amplifier when K_i is equal to and larger than two (as shown in Fig.7-9). This amplifier enlarges external disturbances, variations in parameters, and the kinetic friction and increases the error deviation. One unexpected improvements of K_i is the reduction in overshoot, although the effect of improvement is very small. This could be because $[1-F(s)]\times[I_sK_f(K_i-1)]$ in (7.21) amplifies the high frequency component in I_{cmd} and the system can react to the position error quicker than the conventional disturbance compensator.

The PMLM will oscillate when K_i is large. When K_i is larger than two, the position error (equal to amplitude of input step) is large. This oscillation situation can be explained by (7.22). Referring the second term on the right hand side of the equation, when K_i is larger than two, the force command injecting to the PMLM $I_{cmd}K_{fn}$ is amplified. This amplification is like the action of a pure proportional gain controller (P-controller). The sustaining oscillation occurs when the K_i is large, which is similar to the effect of P-controller with large gain. Therefore, large K_i has to be prevented by defining the profile of K_i deliberately.

The improvement in rising time is not significant when the step size (position error) is larger than 20μm. K_i is chosen to be two when the position error is smaller than 20μm. Although there is no experimental study on the relationship between K_i and the velocity, a large K_i should be utilized when the static friction is present. K_i should be two only when the velocity is small (i.e. $K_i = 2$ when the speed is 1mms^{-1}, within one resolution of velocity measurement).

The profile of K_i is shown in Fig.7-19. The shape of the K_i is determined by experiments and this arrangement is treated as the optimum setting, which does not amplify the noise in I_s and which improves the response time of the PMLM effectively.

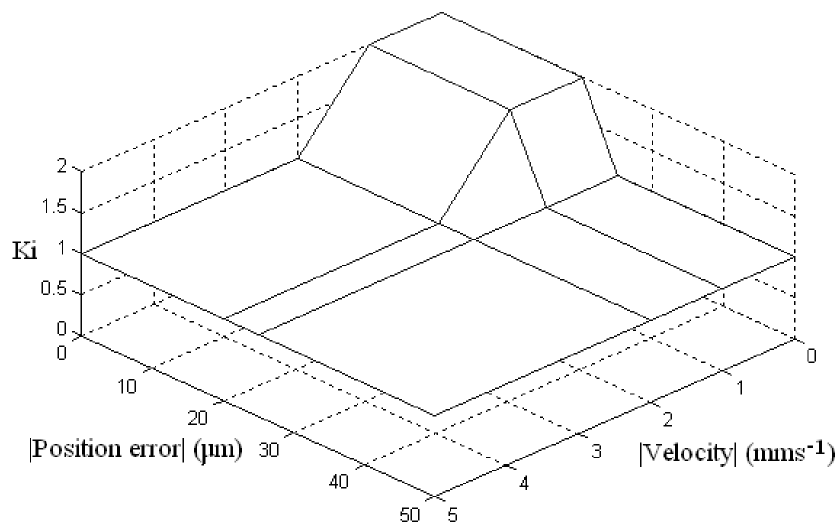

Fig. 7-19 Lookup table for K_i

7.4.6 High precision linear motion controlled system by modified disturbance compensator and IMRC

The mechanism for varying K_i was implemented to the compensated PMLM with the IMRC algorithm. The step response experiments (with square wave input with minimum step size, critical condition step size, large step, and impulse response) were conducted in order to illustrate the success of the proposed algorithm.

Two sets of step response experiments were conducted. The first set selected K_i=1, which is equivalent to construct the linear motion system with the conventional disturbance compensator. The step response experimental results are shown in Fig.7-20(a), Fig.7-21(a), Fig.7-22(a), and Fig.7-23(a). On the other hand, the profile of K_i shown in Fig.7-19 was implemented on the proposed linear motion system. This implementation is equivalent to develop the prototype of the new proposed linear motion system. The results are shown in Fig.7-20(b), Fig.7-21(b), Fig.7-22(b), and Fig.7-23(b).

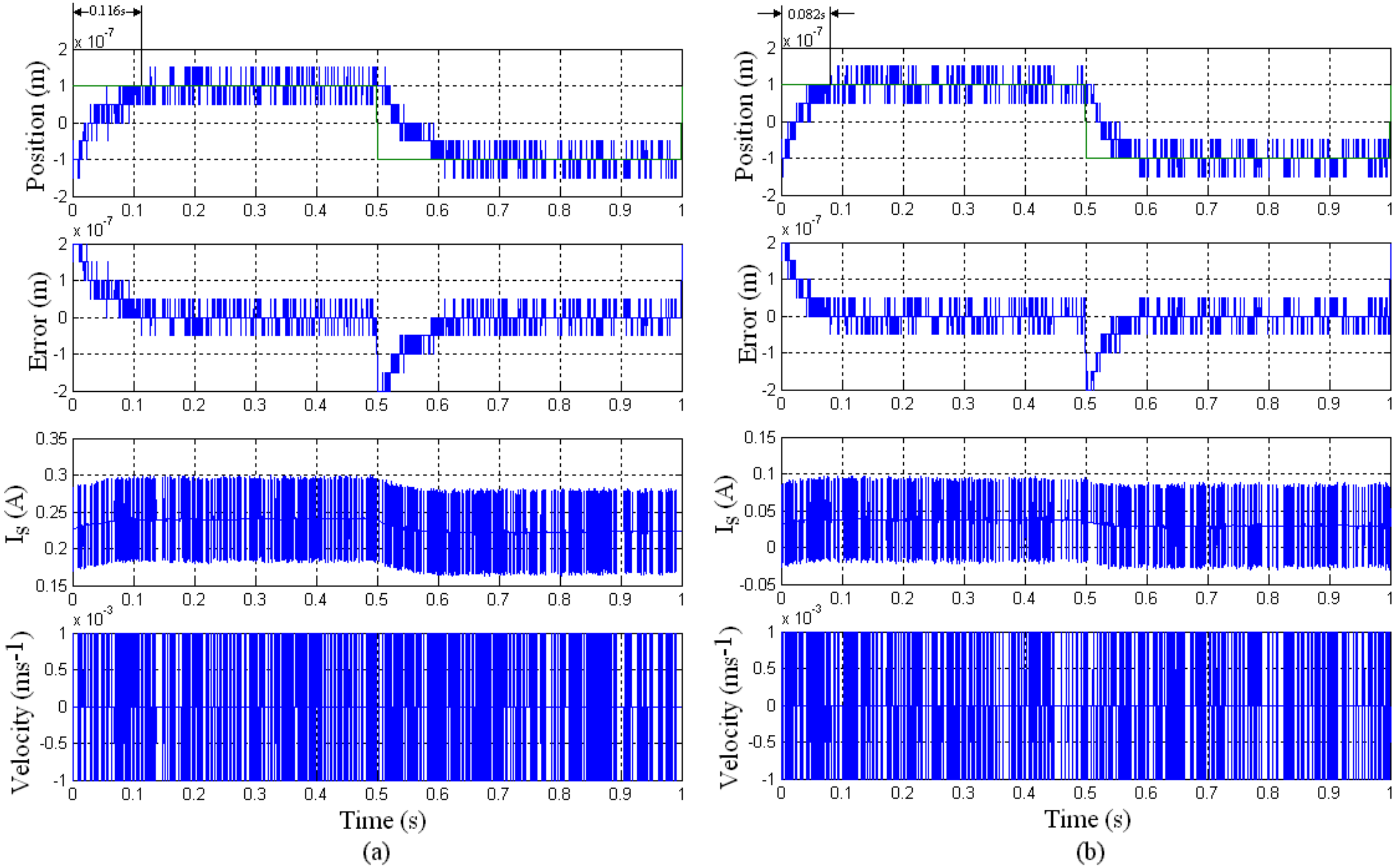

Fig. 7-20(a) The step response with amplitude 100nm of controlled PMLM with original IMRC and disturbance compensator;

Fig. 7-20(b) The step response with amplitude 100nm of controlled PMLM with K_i varying mechanism

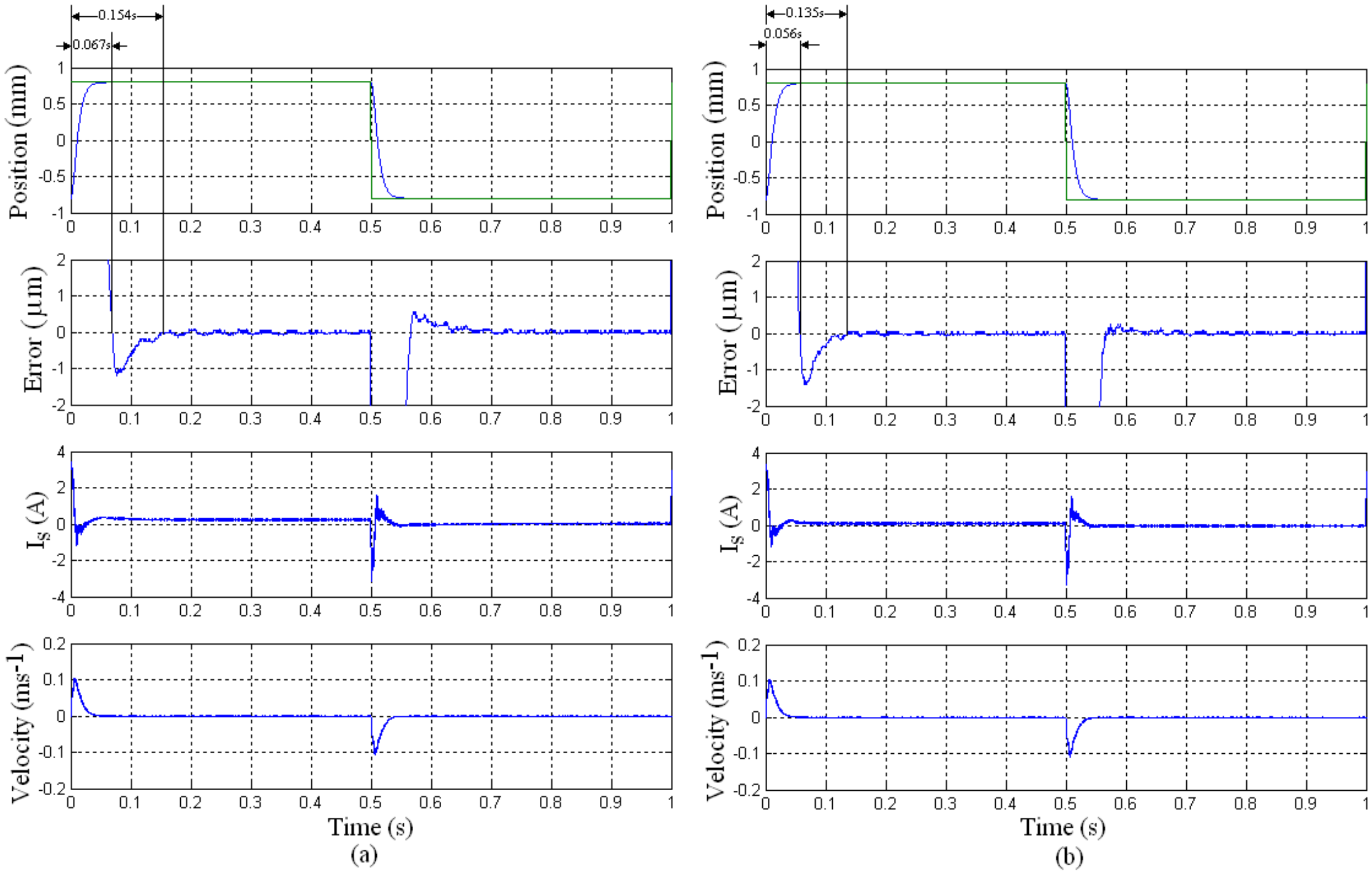

Fig. 7-21(a) The step response with amplitude 800μm of controlled PMLM with original IMRC and disturbance compensator;

Fig. 7-21(b) The step response with amplitude 800μm of controlled PMLM with K_i varying mechanism

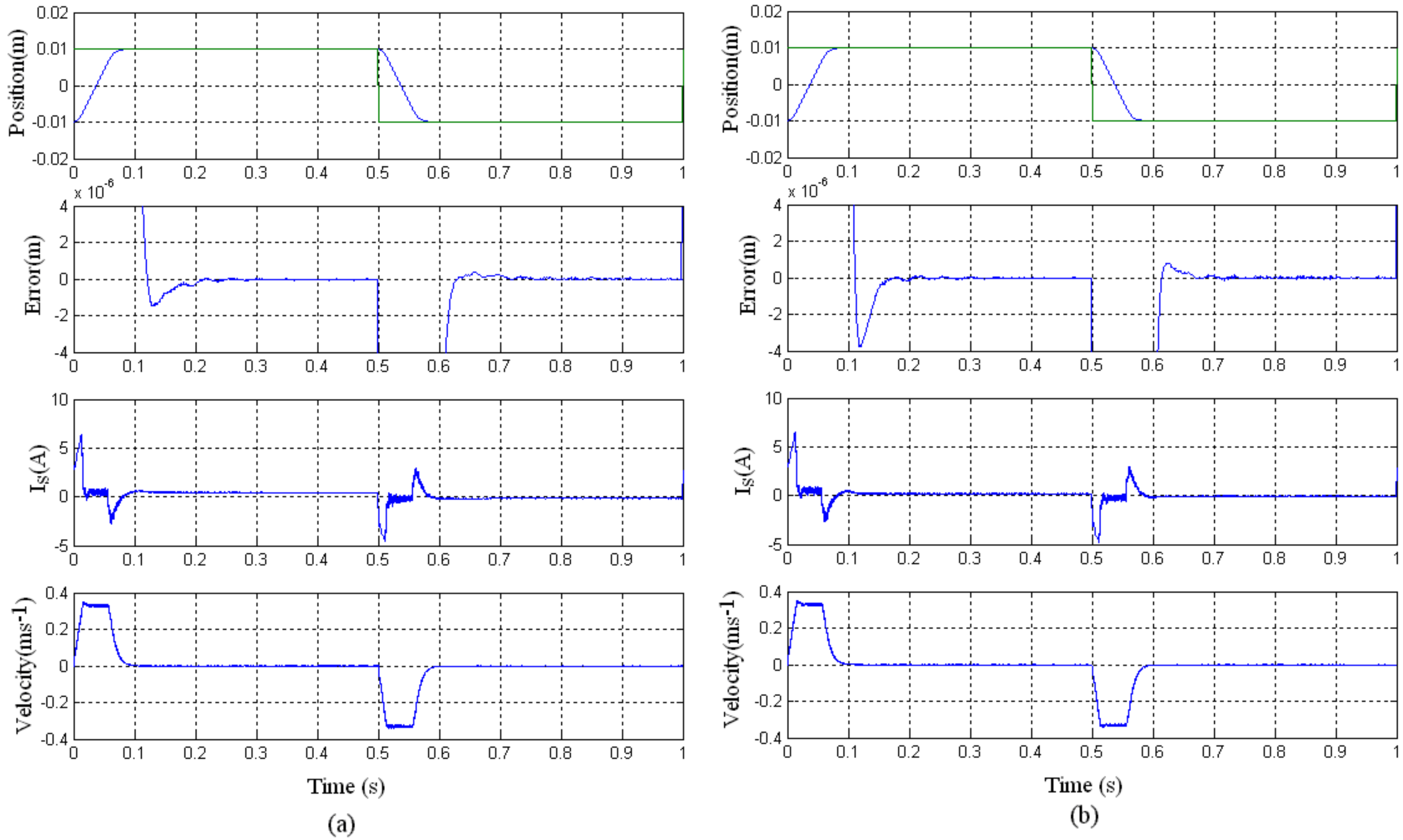

Fig. 7-22(a) The step response with amplitude 10mm of controlled PMLM with original IMRC and disturbance compensator;

Fig. 7-22(b) The step response with amplitude 10mm of controlled PMLM with K_i varying mechanism

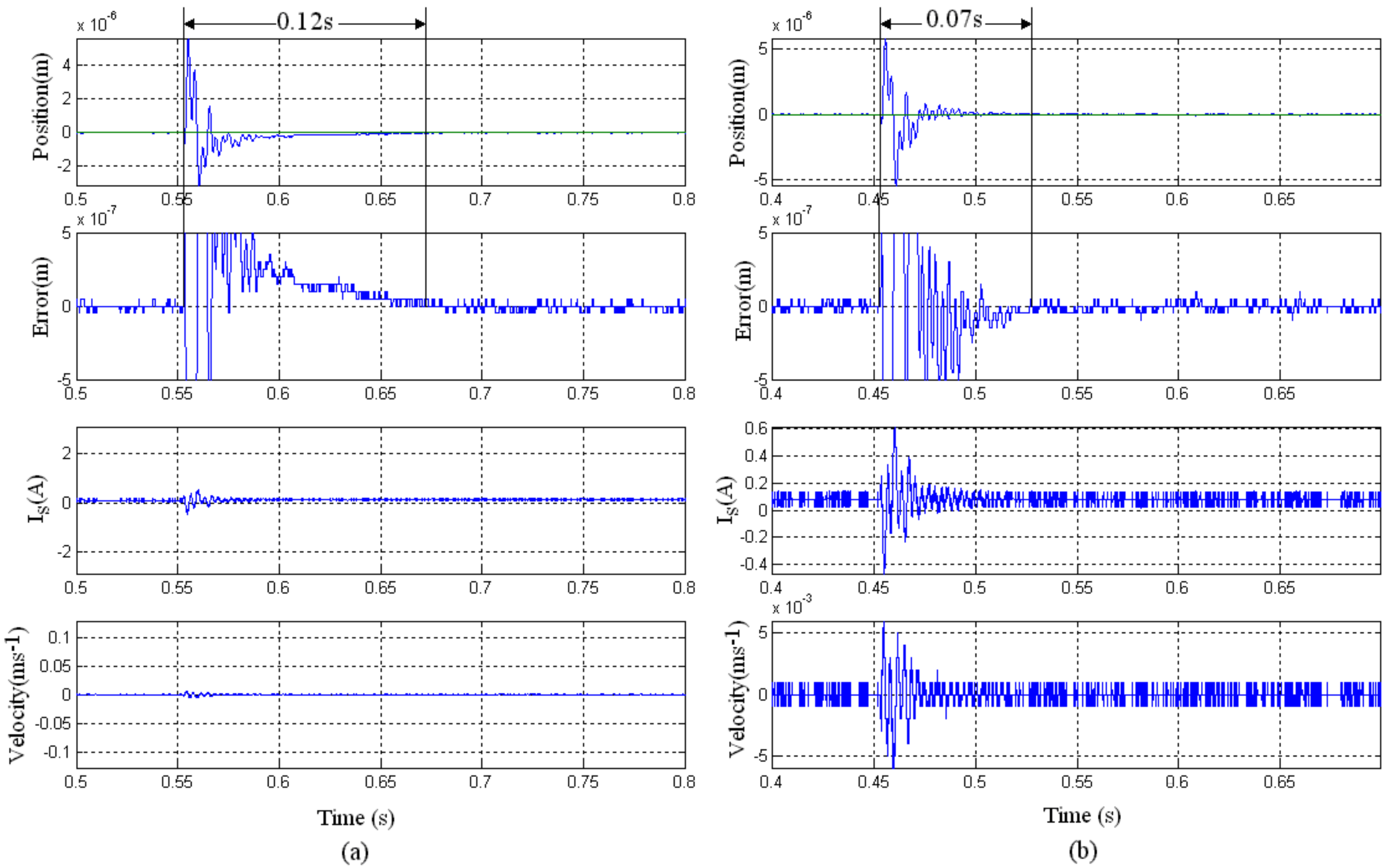

Fig. 7-23(a) The disturbance response of controlled PMLM with original IMRC and disturbance compensator;

Fig. 7-23(b) The disturbance response of controlled PMLM with K_i varying mechanism

Based on the experimental results, the performance of the controlled PMLM with varying K_i mechanism is better than the original control algorithm. Consider the four position-time graphs in Fig.7-20, Fig.7-21, Fig.7-22 and Fig.7-23, the response time of the positioning system with K_i varying mechanism is smaller than the original control algorithm. In Fig.7-20, the response time is reduced from 0.116s to 0.082s. In Fig. 7-21, the response time is reduced from 0.067s to 0.056s. Another valuable observation is related to the recovery time after the overshoot. Referring the error-time graphs in Fig.7-12, after the occurrence of overshoot, the controlled PMLM with varying K_i mechanism can bring the translator back to the set point faster than the controlled PMLM with original algorithm. The varying K_i mechanism not only reduces the rising time of the position of PMLM, but it also can maintain the precision and the accuracy of the position output (steady state error is ±50nm).

To investigate the response time on the disturbance, an impulse disturbance was applied to the controlled compensated PMLM with K_i varying mechanism. The disturbance response is plotted as shown in Fig.7-23. The experimental results illustrate that the disturbance recovery time is improved from 0.12s to 0.07s. As mentioned before, the long settling time shown in Fig.7-23 is caused by the static friction. This experimental result also proves that the effect of static friction can be reduced by using the varying K_i mechanism. It is because extra effort has been added to the PMLM to overcome the high frequency disturbance as shown in (7.22). Meanwhile, the more noises and the oscillations appear in the output of the PMLM with K_i varying mechanism. Actually, K_i is two after the PMLM received an impulse disturbance. Based on Fig.7-9 and (7.23), the minimum value of the gain of transfer function $1\text{-}K_iF(s)$ is 0dB. That means the effect of deviation terms and noises will add to PMLM and the output is therefore so noisy.

The largest step response of the proposed motion system is 800μm (peak to peak 1600μm) without reaching the current and velocity limit. It is not the traveling range limitation of the proposed system. If the profile of the position command is designed properly (controlling the derivative and double derivative of the position command within the limitation), the traveling range of the proposed mechanism will be longer as shown in Fig.7-23. Note that the velocity command and the acceleration command must be controlled, so that the input current I_s can be limited within 3A and the velocity of the PMLM can be limited within the maximum measurable speed of the optical linear incremental encoder (0.35ms^{-1}).

7.5 Summary

A general purpose permanent magnet linear motor (PMLM) is controlled for developing a sub-micron precision linear motion system. The proposed idea in this chapter focuses on the "simplicity and generic of design process". Apart from achieving the high precision motion control, the proposed motion system further focuses on the response time improvement when the PMLM is commanded to move a short distance movement. This aspect is seldom discussed by other researches.

Two main contributions related to the modification of the disturbance compensator are "establishing the process to optimize g_f in the LPF of a disturbance observer" and "introducing the additional gain K_i to modify the performance of a conventional disturbance observer". The effect of static friction is greatly reduced by the presence of K_i. With the success of the modified disturbance compensator, the disturbance-free PMLM is therefore developed.

With the assistance of the modified disturbance compensator, the controlled linear motion system with IMRC is capable of traveling a short distance. Referring the experimental results, the controlled PMLM can be driven with the minimum step size equal to 0.2μm with zero steady state error. The response time is also short (0.082s) because the effect of static friction is rejected. The derivation of steady state error is 0.1μm. Note that when the motor moves a longer distance, the precision of the position can also be maintained, which is proved by the experimental results. Although the linear motion system can achieve the high precision motion control, the controller design process is not difficult and the algorithm is generic. This proposed idea is suitable for converting all PMLM into a high precision linear motion system without the expensive cost. Note that the presented idea can be converted into a marketable product which allows the engineers without experience in accurate motion control developing high precision linear motion system.

Chapter 8
Conclusion and further work

This thesis investigates the different components of a high precision linear motion system, including (i) a laser interferometric displacement sensor with a 3×3 coupler for sub-micron position sensing, (ii) a resolution increasing circuit for improving the measurement speed of incremental encoder, and (iii) a high precision linear motion control algorithm by employing modified disturbance compensation and IMRC. This chapter summarizes the main contributions and findings of this thesis. Possible future research work is also suggested.

8.1 The laser interferometric displacement sensor with 3×3 fiber coupler

The theories of laser interferometer with a 3×3 fiber coupler have been studied. This laser interferometer is modified to be a displacement sensor. The relationship between the position of the movable target and the output values are derived. These optical outputs are converted to electrical signals and modified by the analog circuit so that it can be suitable for conventional controller interface (quadrature signals). In addition, this analog circuit also modifies the resolution of sensor down to $\lambda/16$. The prototype of position sensor is constructed by an interferometer with a 3×3 fiber coupler and a highly coherent laser source. The resolution of the sensor can be as small as 95.5nm.

The proposed method is especially suitable for high precision oscillatory displacement measurement, such as the sensing of feedback motion control in mechanical alignment system.

8.2 Resolution step up circuit for measurement speed improvement of incremental encoder

The method for improving the measurement speed range of an incremental encoder is proposed. A "resolution increasing circuit" is developed. This circuit generates a new set of an incremental quadrature signals from the outputs of incremental encoder. The resolution of the new circuit can provide a higher resolution at a lower frequency bandwidth, when compared with the original outputs of the encoder.

The maximum measurement speed of new circuit outputs will be double that of the original encoder. Since the circuit modification is based on the simplified direction detection method, the output information will suffer from state sequence problem when the travel direction is reversed. The outputs of the original encoder and the resolution increasing circuit are combined by the data fusion method. The measurement speed of the fused outputs can be improved. Also, the direction reversal problems can be overcome.

The fusion algorithm is operated as follows:

1) If the operating speed is very low or zero, then the velocity information from the optical incremental encoder is used.

2) If the operating speed is higher than the maximum measurement speed of the incremental decoder, then the information from the resolution increasing circuit will be used.
3) For operating speeds between 1) and 2), two sets of velocity information will be fused with weighting factors based on their resolutions. The high resolution sensor will have a smaller weighting factor and the more precise sensor will have a larger weighting factor.

The circuit and data fusion method have been verified by experiment.

8.3 High precision motion control algorithm through IMRC and disturbance compensation

Due to the high precision nature of the motion system, it is obvious that the PMLM suffers easily from the effect of friction, ripple force, and parameters variations. It is difficult to achieve a very high precision linear motion system by using a PMLM alone.

Those disturbances and perturbations can be derived from the input (current) and output (velocity) of the PMLM. In this project, the calculated disturbance is converted to the compensation current through a LPF which filters the noise in the compensation signals. The disturbance-free linear motion system is then controlled by an algorithm (IMRC) in order to achieve high precision motion control. The controllers of the velocity loop and the position loop are in cascaded structure so that the controlled performances of velocity and position can be adjusted independently.

A novel variable gain K_i is developed and implemented to minimize the effect of Coulomb static friction. Also, this additional gain K_i in the linear motion system can greatly reduce the response time to the position command and the external disturbance. The idea of this control algorithm is verified by experiments. The results show that the proposed control algorithm can achieve a high speed and high accuracy linear motion system with a steady error deviation less than 0.1μm. The ability of static friction elimination is investigated and verified. Compared with the original disturbance compensator, the dynamic response improvement is also successfully achieved.

8.4 Suggestion for further research

Although this thesis provided several promising performance tools for achieving high precision linear motion control, there is still room for improvements. Below are some suggestions for further research.

8.4.1 Re-design of mechanical structure of the interferometric displacement sensor

Although the displacement sensor constructed by a 3×3 fiber coupler provides high precision measurement with 95.5nm resolution, it is not suitable for measuring the motion with a high acceleration or a high rate of change of acceleration. This limitation has been mentioned in the thesis and it is caused by elastic material in mirror mounting.

During the experiment, it is proved that the acceleration of the motor will affect the accuracy of the measurement due to the elastic material in mirror mounting. Therefore, the acceleration of the controlled object has to be limited in order to generate an accurate measured position.

This interferometer with 3×3 coupler can be further improved by modifying the rigidity of the mirror mounting. The reconstructed mirror mounting material and mechanical structure have to be rigid so that the unwanted oscillation described in the thesis will not appear. Anti-vibration mirror mounting could also be considered and used.

8.4.2 Variable gain K_i selection for proposed high precision motion control algorithm

Precision linear motion system has been achieved by the PMLM. The steady state error is limited within 100nm. Compared with the PMLM compensated by the conventional disturbance compensator and controlled by the IMRC, the response time of the linear motion system with the modified compensation algorithm can provide faster response to the position command and the external disturbance.

In this project, the variable gain K_i is selected based on a finite number of experimental results. By analyzing the performance of PMLM, a predefined look-up table for K_i is set-up. However, this approach may not optimize the performance of the linear motion system in all situations. Instead of formulating the K_i based on the experimental results, some systematic method should be developed for K_i optimization.

The aim of inserting K_i is to improve the response time of the PMLM and to minimize the effect of static friction. Therefore, by formulating and using the information of an accurate friction model, K_i can be selected properly and the compensation of the static friction can be optimized. Also, an adaptive or iterative algorithm can be employed for K_i selection. The relationship between the static friction, position of the actuator, and the value of K_i should be studied in further research work.

8.4.3 Noise filtering in the velocity measurements

In this thesis, the velocity measurements are calculated by differential method. This calculation introduces some noise on the velocity measurement. In the motion control, the velocity measurements are used as a feedback for the velocity control loop. Because of the effect of noise, the output of the system is easily oscillated. Some velocity measuring methods, such as Kalman filter velocity observer, can be used so that the noise-free velocity measurement and the system without oscillation can be achieved. The disadvantage of these measurement techniques is increasing the time delay in the velocity output. The noise verse time delay trade-off can be further considered in future researches.

Appendixes

Appendix 1: Specification for the novel laser interferometric displacement sensor for sub-micron precision control

Mechanical	Maximum measurable range (theoretical value)	58.4m
	Maximum measurable speed	37500 λs^{-1}
	Resolution	$\lambda/16$
	Angle adjustment for the mirror	$\pm 5^{o}$
Electrical	Voltage supply (except liner drivers)	15V
	Voltage supply for liner drivers	5V
	Maximum frequency bandwidth	150KHz
	Interface	Quadrature signals
Optical	Laser source (External cavity turntable laser)	1528nm
	Laser source line width	5MHz
	Photodiode responsitivity	0.9A/W

Appendix 2: Specification for the high precision motion control with non-linear uncertainty elimination for PMLM

Mechanical	Traveling range	852mm
	Mass of translator (not include the encoder and cable chains)	0.293kg
	Resolution	50nm
	Steady state error deviation	100nm
	Pole pitch (one electric cycle)	25.6mm
	Maximum velocity (limited by the position sensor)	350mm/s
	Maximum step input amplitude (peak to peak)	1.6mm
	Maximum thrust force	12.3N
Electrical	Working voltage	30V
	Maximum current (limited by the power supply)	3A
	Back EMF constant	4.42 V/ms^{-1}
	Force constant	4.1 N/A

Appendix 3: Photograph of the prototype (the novel laser interferometric displacement sensor for sub-micron precision control)

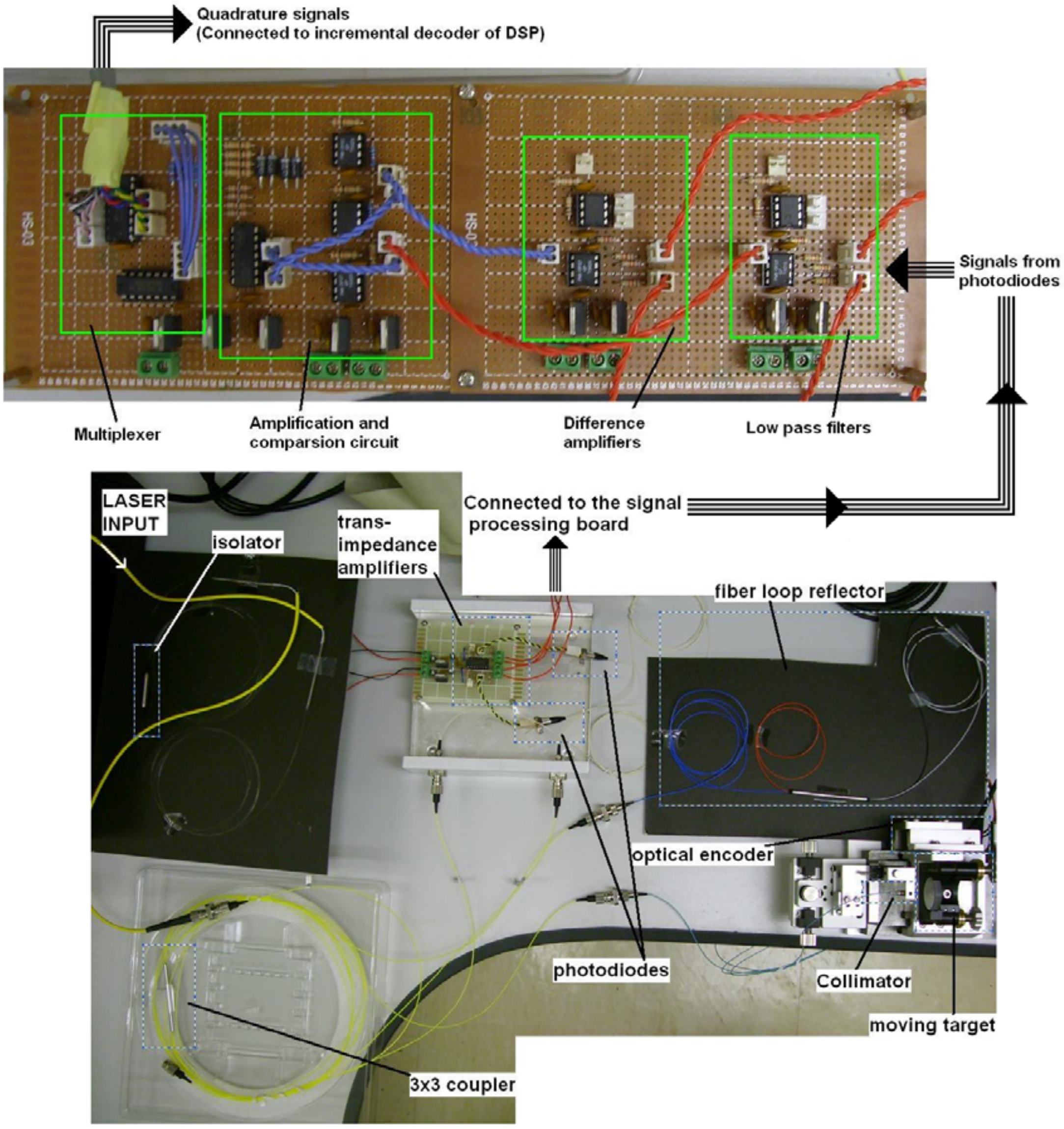

Appendix 4: Photograph of the prototype (Enhancement approaches to improve the performance of incremental encoders & High precision motion control with non-linear uncertainty elimination for PMLM)

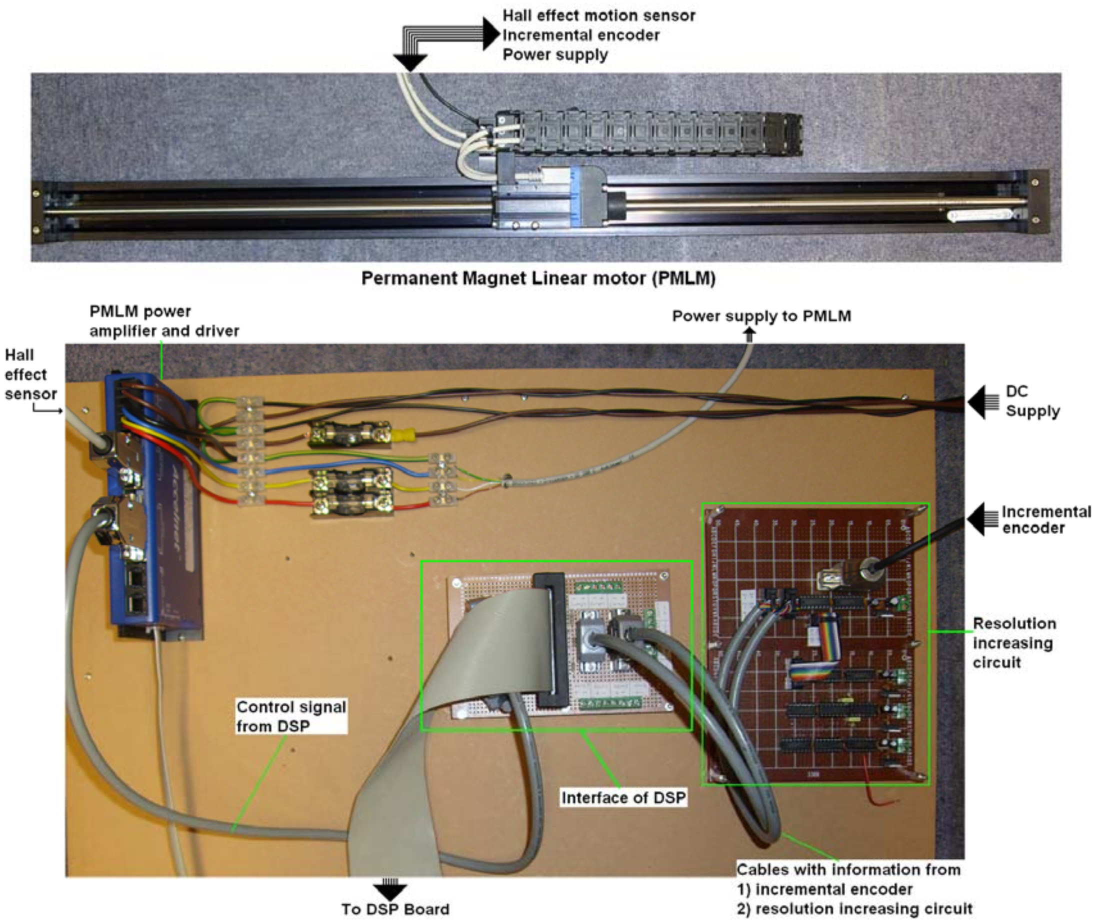

References

[1] "Motion control application stories ", http://www.qproducts.sk/files/Advantech_Motion_control_story.pdf, extracted on 26 Sept 2010

[2] "Process & Tools: Precision Motion ", http://www.www.aeiboston.com/process_motion_stage.htm, extracted on 26 Sept 2010

[3] Huang Y.S., Sung C.C.: ‘Implementation of sliding mode controller for linear synchronous motors based on direct thrust control theory’, IET Control Theory and Applications, pp.326-338, October 2008

[4] F. Cupertino, D. Naso, E. Mininno, B. Turchiano, "Sliding-Mode Control With Double Boundary Layer for Robust Compensation of Payload Mass and Friction in Linear Motors", IEEE Transactions on Industry Applications, vol. 45 , no. 5, pp. 1688 – 1696, October,2009

[5] S. L Chen; K. K. Tan; S. Huang; C. S. Teo; "Modeling and Compensation of Ripples and Friction in Permanent-Magnet Linear Motor Using a Hysteretic Relay", IEEE/ASME Transactions on Mechatronics, vol. 15 , no. 4, pp.586-594, August 2010

[6] D.S. Nyce, “Linear position sensor, technology and application”, Hoboken, John Wiley, 2004

[7] “Non-contact position encoder” brochure from Renishaw.

[8] C. W. Lee, X. M. Zhang, S. C. Tjin1, and A. Q. Liu, " Nano-scale displacement measurement of MEMS devices using fiber optic interferometry", Journal of The Institution of Engineers, Singapore, Vol. 44, Issue 5, pp.1-8, 2004

[9] S. Donati, L. Falzoni, and S. Merlo, “A PC-interfaced, compact laserdiode feedback interferometer for displacement measurements,” IEEE Trans. Instrum. Meas., vol. 45, Issue 6, pp. 942–947, Dec. 1996

[10] S. Donati, G. Giuliani, and S. Merlo, “Laser Diode Feedback Interferometer for measurement of Displacements without Ambiguity,” IEEE Journal of quantum electronics, vol. 31, Issue. 1, pp. 113-119, Jan. 1995

[11] M. Wang, G. Lai, "A self-mixing interferometer using an external dual cavity", Measurement Science and Technology, Institute of Physics Publishing, Vol. 14 ,pp. 1025–1031, May 2003

[12] H. C. Seat, S. Pullteap, T. Bosch, "An Extrinsic Fibre Optic Interferometer with Possible Signal Fading Compensation for Vibrometric Applications", IMTC 2005, Vol. 3, pp. 2236 - 2241, Ottawa, Canada, 17-19 May 2005

[13] X. Liu, W. Clegg, D. Jenkins, B. Liu, "Polarization interferometer for measuring small displacement", Proceedings of the 17th IEEE Instrumentation and Measurement Technology Conference, Baltimore, Maryland ,vol.2 pp.729-732, 2000

[14] Q. Huang, X. Liu, L. Sun, "Homodyne laser interferometric displacement measuring system with nanometer accuracy", 9th International Conference on Electronic Measurement & Instruments, pp. 1_908-1_912, 2009

[15] M.A.Choma, C. Yang, and C. J.A. Izatt, "Instantaneous quadrature low-coherence interferometry with 3×3 fiber optic couplers", Optics Letters, vol.28. no.22, pp.2162-2164, 15 Nov. 2003

[16] M.C. Tomic, J. M. Elazar, Z.V. Djinovic, "Low-coherence interferometric method for measurement of displacement based on a 3×3 fibre-optic directional coupler", Journal of Optics A: Pure and Applied Optics 4, pp.381–S386, 2002

[17] D. B. Mortimore, "Fiber Loop Reflectors", Journal of Lightwave technology, vol. 6, no. 7, pp.1217-1224, July 1988

[18] S. K. Sheem, "Optical fiber interferometers with 3×3 directional couplers: Analysis", Journal of Applied Physics, Vol. 52, no.6, pp3865-3872, June 1981

[19] S. K. Sheem, "Fiber-optic gyroscope with 3×3 directional coupler", Applied Physics Letter, Vol. 37, no. 10, pp. 869-871, November 1980

[20] F. Schliep, Nonideal behaviour of sinlemode fibre-optic 3×3 directional couplers", Electronics letters, vol.31, no.17, pp.1496-1498, 17 Aug. 1995

[21] J.F. Cliche, A.Zarka, M. Tetu and J.-M. Chartier, "Automatic locking of a semiconductor laser at 633nm on linear absorption iodine transitions", IEEE Transaction on Instrumentation and Measurement, vol 48, no. 2, pp.596-599, April. 1999

[22] J.-F. Cliche, M. Tetu, "Automatic absolute frequency calibration of tunable optical sources", Optical Fiber Communication Conference 2000, Baltimore, U.S.A, vol 2, pp.269-271, 7-10 March 2000

[23] R. Rojas, "The Kalman filter", the Mathematical Intelligencer, Volume: 1, Issue: 2, 2005

[24] "Electronics Tutorial about Frequency Dividers", http:// www.electronics-tutorials.ws/counter/count_1.htm, Electronics-Tutorial.ws, extracted on 29 Sept 2009

[25] A.Mahajan, K.H.Wang, P.K.Ray, "Multisensor Integration and Fusion Model that Uses a Fuzzy Inference System",IEEE/ASME TRANS on mechatronics, Vol. 6, No. 2, pp.188-196, June 2001

[26] A. H. Slocum, "Title Precision machine design", Englewood Cliffs, N.J. : Prentice Hall, 1992

[27] J. F. Gieras, "Permanent magnet motor technology: design and applications, Edition 2nd," Marcel Dekker, 2002

[28] K. K. Tan, T. H. Lee. H. Dou, S. Huang, “Precision motion control – Design and implementation”, Springer, 2001

[29] M. A. Krzeminski, "Modeling Friction through the use of a Genetic Algorithm", Master thesis, Electrical and Computer Engineering, the University of Waterloo, Waterloo, Ontario, Canada, 2003

[30] L. Bo, D.Pavelescu., “The Friction-Speed relation and its Influence on the Critical Velocity of Stick-Slip Motion”, Wear, Vol 82, pp.277, 1982

[31] A. Tustin, "The Effects of Backlash and Speed-Dependent Friction on the Stability of Closed Cycle Control System", Journal of IEEE, Part IIA: Automatic Regulators and Servo Mechanisms, Vol. 94, pp 143-151, 1947.

[32] C. Canudas de Wit, P.Noel, A. Aubin, B. Brogliato, "Adaptive Friction Compensation in Robot Manipulators: Low Velocities". International Journal of Robotics Research, Vol. 10, No. 3, pp.189-199, 1991

[33] B. Armstrong-Helouvry, P. Dupont, C. Canudas de Wit, "A Survey of Models, Analysis Tools and Compensation Methods for the Control of Machines with Friction", Automatica, Vol 30 No 7, pp.1083-1138, 1994

[34] C. Canudas de Wit, H. Olsson, K.J. Astrom, P. Lischinsky, "A New Model for Control of Systems with Friction", IEEE Transactions on Automatic Control, Vol 40, No 3, pp.419-425, March 1995

[35] P. A. Ioannou, J. Sun, “Robust adaptive control”, Prentice Hall, Upper Saddle River, 1996

[36] R. Krishnan, "Electric motor drives- Modeling, Analysis, and Control", Pearson Education, Prentice Hall, 2001

[37] D.Y. Ohm, "Dynamic Model of PM Synchronous Motors", technical articles, Drivetech, Inc, 2000

[38] Q. Li, K. Zou. "Introduction to feedback control",Upper Saddle River, N.J., Pearson Prentice Hall, 2010.

[39] D. Xue, Y. Q. Chen, D. P. Atherton., "Linear feedback control - analysis and design with MATLAB", Philadelphia, Pa., Society for Industrial and Applied Mathematics, 2007

[40] K.K. Tan, S. Zhao, "Adaptive force ripple suppression in iron-core permanent magnet linear motors ", Proceedings of the 2002 IEEE International Symposium on Intelligent Control, Vancouver, Canada, pp.266-269, 27-30 Oct. 2002

[41] A. Datta, “Adaptive internal model control”, Springer, 1998

[42] K. K. Tan, S. N. Huang, T. H. Lee, "Robust adaptive numerical compensation for friction and force ripple in permanent-magnet linear motors", IEEE Transactions on Magnetics, vol. 38, no.1, pp. 221-228, 2002

[43] R. L. A. Ribeiro, A. D. Araiijo, A. C. Oliveira, C. B. Jacobina, "A High Performance Permanent Magnet Synchronous Motor Drive by using a Robust Adaptive Control Strategy", IEEE Power Electronics Specialists Conference, 2007, Orlando, Florida, pp.2260-2266, 8-12 Jul. 2007

[44] X. Xiao, Y. Li, M. Zhang,Y. Liang, "A Sensorless Control Based on MRAS Method in Interior Permanent-Magnet Machine Drive", International Conference on Power Electronics and Drives Systems 2005,Kuala Lumpur, Malaysia, vol.1 , pp.734-738, 28 Nov - 1 Dec. 2005

[45] Q. Guo, D. Xie, "On-line identification and compensation-based model reference adaptive neural network speed control for LPMSM" 7th International Workshop on Advanced Motion Control 2002, Maribor, Slovenia, pp.322 – 325, 3-5 Jul. 2002

[46] L. Fan, Y. Liu, "Iterative Learning Control for Linear Motor Motion System", 2007 IEEE International Conference on Automation and Logistics, Jinan, China, pp.2379-2383 , 18-21 Aug. 2007

[47] J. Wu, H. Ding, "Iterative Learning Variable Structure Controller on Linear Motors for Point-To-Point Motion", 2006 IEEE Conference on Robotics, Automation and Mechatronics, Bangkok, Tailand, pp.1-5, 7-9 Jun. 2006

[48] S. Komada, M. Ishida, K. Ohnishi, T. Hori,"Motion control of linear synchronous motors based on disturbance observer", 16th Annual Conference of IEEE Industrial Electronics Society, vol. 1, pp.154-159, 27-30 Nov. 1990

[49] S. Komada, M. Ishida, K. Ohnishi, T. Hori, "Disturbance observer-based motion control of direct drive motors", IEEE Transactions on Energy Conversion, vol. 6, no.3, pp.553-559, 1991

[50] A. Datta, L. Xing, "Adaptive Internal Model Control: H-infinity Optimization for Stable Plants", IEEE Transactions on Automatic Control, Vol. 44, No. 11, pp.2130-2134, Nov 1999

[51] G.J. Silva, A. Datta, "Adaptive Internal Model Control: The Discrete-Time Case", Proceedings of the American Control Conference, San Diego, California, pp. 547-555, June 1999

[52] K. Furuta, M. Iwase, S. Hatakeyama, "Internal Model and Saturating Actuation in Human Operation From View of Human-Adaptive Mechatronics", IEEE Transactions on Idustrial Electronics, Vol. 52, No. 5, pp.1236-1246, Oct 2005

[53] A. Datta, L. Xing, "The Theory and Design of Adaptive Internal Model Control Schemes", Proceedings of the American Control Conference, Philadelphia, Pennsylvania, pp.3677-3684, June 1998

[54] K. M. Al-Zahrani, M. Shafiq, "Adaptive Inverse Control with IMC Structure Implementation on Robotic Arm Manipulator", 10th IEEE Conference on Emerging Technologies and Factory Automation, ETFA 2005, pp.537-543, 2005

[55] K. C. Kim, Y.M. Choi, J.J.Kim and D. G. Gweon, "Development of Control Algorithm to Reduce Force Ripple for High Speed Permanent Magnet Linear Motor(PMLM)", International Conference on Control, Automation and Systems 2007, Seoul, Korea, pp.1712-1716, 17-20 Oct. 2007

[56] D.L. Zhang, Y.P. Chen, Z.D. Zhou, W. Ai, X.D. Li, "Robust adaptive motion control of permanent magnet linear motors based on disturbance compensation", IET Electr. Power Appl., Vol. 1, No. 4, pp.543-548, July 2007

[57] K.S. Low, M.T. Keck, "Advanced Precision Linear Stage for Industrial Automation Applications", IEEE Transactions on Instrumentation and Measurement, Vol. 52, No. 3, pp.785-789, June 2003

[58] S. Katsura, K. Irie, K. Ohishi, "High Precision Force Control by Multi-Sensor based Disturbance Observer", IEEE Industrial Electronics, IECON 2006 - 32nd Annual Conference, pp.5227-5233,2006

[59] S. Mukhopadhyay, S. Sen, "Special Control Structures: Cascade, Override and Split Range Control", lecture notes of Industrial Automation and Control from IIT KHARAGPUR NEPTEL ONLINE, located at the following URL (visited November 2010): http://nptel.iitm.ac.in/courses.php?branch=Electrical

[60] J. Casler, A. Haryanto, S. Kahle, W. Xu, "CascadeControl: Conditions for Cascade Control", The Michigan Chemical Process Dynamics and Controls Open Text Book, located at the following URL (visited November 2010): http://controls.engin.umich.edu/wiki/index.php/CascadeControl

[61] D. J. Cooper, "An Implementation Recipe for Cascade Control", Controlguru: practical process control e-textbook, located at the following URL (visited November 2010): http://www.controlguru.com/2007/090207.html